University of Denver
Digital Commons @ DU

Electronic Theses and Dissertations | Graduate Studies

3-1-2015

Assessment of Normal Knee Kinematics Using High-Speed Stereo-Radiography System

Vasiliki Kefala
University of Denver

Follow this and additional works at: https://digitalcommons.du.edu/etd

Part of the Biomedical Engineering and Bioengineering Commons

Recommended Citation

Kefala, Vasiliki, "Assessment of Normal Knee Kinematics Using High-Speed Stereo-Radiography System" (2015). *Electronic Theses and Dissertations*. 331.
https://digitalcommons.du.edu/etd/331

This Thesis is brought to you for free and open access by the Graduate Studies at Digital Commons @ DU. It has been accepted for inclusion in Electronic Theses and Dissertations by an authorized administrator of Digital Commons @ DU. For more information, please contact jennifer.cox@du.edu,dig-commons@du.edu.

Assessment of Normal Knee Kinematics using High-Speed Stereo-Radiography System

---

A Thesis

Presented to

The Faculty of the Daniel Felix Ritchie School of Engineering and Computer Science

University of Denver

In Partial Fulfillment

of the Requirements for the Degree

Master of Science

---

by

Vasiliki Kefala

March 2015

Advisor: Dr. Matthew H. Gordon

Author: Vasiliki Kefala
Assessment of Normal Knee Kinematics using High-Speed Stereo-Radiography System
Advisor: Dr. Matthew H. Gordon
Degree Date: March 2015

Abstract

The measurement of dynamic joint kinematics in vivo is important in order to understand the effects of joint injuries and diseases as well as for evaluating the treatment effectiveness. Quantification of knee motion is essential for assessment of joint function for diagnosis of pathology, such as tracking and progression of osteoarthritis and evaluation of outcome following conservative or surgical treatment. Total knee arthroplasty (TKA) is an invasive treatment for arthritic pain and functional disability and it is used for deformed joint replacement with implants in order to restore joint alignment. It is important to describe knee kinematics in healthy individuals for comparison in diagnosis of pathology and understanding treatment to restore normal function. However measuring the in vivo dynamic biomechanics in 6 degrees of freedom with an accuracy that is acceptable has been shown to be technically challenging. Skin marker based methods, commonly used in human movement analysis, are still prone to large errors produced by soft tissue artifacts. Thus, great deal of research has been done to obtain more accurate data of the knee joint by using other measuring techniques like dual plane fluoroscopy. The goal of this thesis is to use high-speed stereo radiography (HSSR) system for measuring joint kinematics in healthy older adults performing common movements of daily living such as straight walking and during higher demand activities of pivoting and step descending in order to establish a useful baseline for the envelope of healthy knee motion for subsequent comparison with patients with TKA. Prior to data collection, validation and calibration techniques as well as dose estimations were mandatory for the successful accomplishment of this study.

Acknowledgements

I would like to offer my sincere appreciation to all of those at the University of Denver who provided me with the opportunity to complete this work. It is always difficult to write a gratitude text when the number of persons involved is large. It does not mean that others that are not referred to do not deserve my attention and recognition as well. My thanks to my advisors Dr. Kevin Shelburne, Dr. Matthew Gordon and Dr. Bradley Davidson for the orientation and long discussions not only about the contents of this dissertation but also for the resources and human opportunities provided. I would like also to thank Dr. Adam Cyr and Dr. Michael Harris for their careful guidance and insight throughout my degree. To my parents, brothers and husband, I express my gratitude for the sacrifices supported that made possible my graduation and for all the comfort and affection that they have always revealed. For all my colleagues and friends, companions in this path, by their camaraderie and solidarity shown, not only by the encouragement that they always provided but also by the long conceptual and philosophical discussions taken through along these two years. The difficult moments will be better overcome together.

Table of Contents

1 Introduction **1**
- 1.1 Motivation and Problem Statement . . . 3
- 1.2 Contributions . . . 3
- 1.3 Organization of Thesis . . . 4

2 Previous Investigations and High Speed Stereo Radiography **5**
- 2.1 Literature review-Background . . . 6
  - 2.1.1 Methods for measuring joint kinematics . . . 6
  - 2.1.2 Marker-based motion capture techniques . . . 6
  - 2.1.3 Dynamic Radiography . . . 8
  - 2.1.4 Single Plane Fluoroscopy . . . 9
  - 2.1.5 Dual Plane Fluoroscopy . . . 13
- 2.2 Methods of tracking . . . 20
  - 2.2.1 Section I: Bead Tracking . . . 21
  - 2.2.2 Section II: Implant Tracking . . . 24
  - 2.2.3 Section III: Bone Tracking . . . 28
- 2.3 Overview HSSR at the university of Denver . . . 36

3 Calibration and Validation of HSSR System **39**
- 3.1 Introduction . . . 39
- 3.2 Alignment . . . 39
- 3.3 Distortion Correction . . . 40
- 3.4 Calibration . . . 42
- 3.5 Validation of system accuracy . . . 44
  - 3.5.1 Bead Tracking . . . 44
  - 3.5.2 Implant Tracking . . . 47
  - 3.5.3 Bone Tracking . . . 49

4 Literature Review- Precise Healthy Knee Kinematics measurements **53**

5 Application to Normal Knee **70**
- 5.1 Introduction . . . 70
- 5.2 Methods and Materials . . . 72
- 5.3 Results . . . 78

5.4 Discussion 90

Appendices **103**

A **104**
A.1 PCXMC 104
A.2 Using the program 104
A.2.1 Dose estimations for HSSR projects 112

B **119**
B.1 2D-3D matching process 119
B.1.1 Autoscoper Tracking Tutorial 119

List of Tables

2.1 **Summary of the results based on the techniques presented in this study**.(S): Scapula, (H): Humerus, (P):Patella, (F): Femur, (PF): Patello-femoral displacement, (FT): Femoro-tibial displacement, (R): Radius, (U): Ulna, (CA): Contact areas displacement. 35

3.1 Average overall error for bead, implant and bone tracking 51

4.1 Summary of the studies presented here that have used precise techniques for assessment of healthy knee kinematics. M: Male, F:Female, TF:Tibiofemoral, FT:Femorotibial, IE:Internal-External, AP:Anterior-Posterior, ML:Mediolateral, MC:Medial COndyle, LC: Lateral Condyle, ATT:Anterior tibial translation, LTT:Lateral tibial translation 69

5.1 Subjects Specifications 73
5.2 Average and Excursion values for the 3 DOF for all subjects and activities . 87
5.3 Standard deviation of the Excursion 88
5.4 Standard Deviation of the average standard deviations 89

List of Figures

2.1 The HSSR system configuration 36
2.2 Radiograpchic components 37

3.1 Grids placed in front of the surface of the image intensifier 41
3.2 Raw distorted image of a machined steel plate with precise hole sizing and spacing on the left and undistorted image on the right 41
3.3 Calibration cube with 52 steel beads 42
3.4 XROMM calibration interface 43
3.5 All the calibration points are being selected and the camera parameters are shown in the sidebar set 44
3.6 Example translation and rotation of the calibration cube for bead tracking . 45
3.7 Positional stage used for the validation of the HSSR system 45
3.8 Bead Tracking using XrayProject software 46
3.9 Radiograph for bead tracking with example beads for a single plane (yellow,blue,red) 46
3.10 Femoral implant component 47
3.11 A. Stereo radiographs from HSSR system for implant tracking. B. Stereo radiographs visualized in Autoscoper for implant tracking at different time points/positions 48
3.12 CAD model of the femoral component were simultaneously fitted over the 2D projections from each plane. This process was repeated for each position, allowing for 3D positioning to be tracked. 49
3.13 Knee phantom. 50
3.14 A:Stereo radiographs from HSSR for the knee phantom, B:Stereo radiographs when they are imported in Autoscoper 50
3.15 Alignment of the 3D model (orange) with the 2D radiographs in Autoscoper 51

4.1 The 6 DOFs of the knee 54
4.2 Anterior, Medial and Posterior view of the right knee anatomy [1] 55
4.3 View from one of the camera positions as the subject walked with the target triads attached to the femoral and tibial pins [1] 57
4.4 Subject position within the MRI imager [2] 59

[1] http://www.waterburyhospital.org

4.5 Schematic diagram showing a subject performing active knee extension under dynamic single fluoroscopic surveillance [3] 61
4.6 Computer rendering of the configuration of the biplane fluoroscopy system [4] 65

5.1 Healthy knee subject during normal gait 73
5.2 An image of the reconstructed femur and tibia/fibula. Autoscoper was used to align the projected contours of the imported bone geometries to the stereo images 77
5.3 Representative bone geometry model derived from the CT scan depicting coordinate axis used to determine the reference position of the femur and tibia: superior(+)-inferior (SI), anterior(+)-posterior (AP), medial(+)-lateral (ML) 78
5.4 Knee Extension trial for 3DOF with respect flexion angle and Knee Extension with respect percent cycle 80
5.5 Normal Gait for the 3DOF and the Knee Extension trial 82
5.6 Pivot for the 3DOF and the Knee Extension trial 83
5.7 Step Descent for the 3DOF and the Knee Extension trial 84
5.8 Excursion plots for the 3DOF for all the activities.I/E (top), V/V (middle), A/P (bottom) 86
5.9 All trials together for each subject individually 90

A.1 The main form of PCXMC 105
A.2 The X-ray examination input form of PCXMC 106
A.3 The Monte Carlo Simulation form 108
A.4 The dose calculation form. Before a file has been opened the table is empty 109
A.5 Calculation of th X-ray spectrum form of PCXMC 110
A.6 The patient input dose specification form of PCXMC 110
A.7 The risk assessment form of PCXMC. WHen it is firstly open the form shows data of 30 yeal old European with no radiation exposure 111
A.8 Dose Estimates for KS01 healthy knee subject 112
A.9 Dose Estimates for KS02 healthy knee subject 113
A.10 Dose Estimates for KS03 healthy knee subject 113
A.11 Knee Dose Estimates by using pulsed radiographic mode for 1 ms of exposure 114
A.12 Knee Dose Estimates by using pulsed radiographic mode for 4 ms of exposure 114
A.13 Dose estimates for hip by using pulsed radiographic mode for 1 ms of exposure 114
A.14 Dose estimates for hip by using pulsed radiographic mode for 5 ms of exposure 115
A.15 Dose estimates for hip by using pulsed radiographic mode for 1/0.4 ms of exposure and for 100 f/sec 115
A.16 Dose estimates for hip by using pulsed radiographic mode for different pulsed widths 115

A.17 Dose estimates for Cadaver hip by using pulsed radiographic mode 116
A.18 Dose estimates for Shoulder by using pulsed radiographic mode 116
A.19 Dose estimates for Cadaver Shoulder by using pulsed radiographic mode . . 117
A.20 Dose estimates for Foot by using pulsed radiographic mode for 5 ms of exposure 117
A.21 Dose estimates for Pelvis by using pulsed radiographic mode for 5 ms of exposure 118
A.22 Dose estimates for Torso by using pulsed radiographic mode for 5 ms of exposure 118

B.1 An example of a configuration file 120
B.2 When the configuration file is loaded in Autoscoper 121
B.3 Illustration of how to add filters in Autoscoper 122
B.4 Options for the DRRender in Autoscoper 123
B.5 Load or Save filters in Autoscoper 123
B.6 Demonstration of the knee joint in Autoscoper when the filters are applied . 124
B.7 World view in Autoscoper 125
B.8 Demonstration of positioning the pivot in the center of the femoral component using the World view 126
B.9 2D-3D alignment of the femoral component as shown in Autoscoper 127
B.10 Tracking options in Autoscoper 128
B.11 DOS window showing when the optimization is completed 129
B.12 How to lock a frame when the 2D-3D alignment for that current frame is satisfactory 130
B.13 Saving options in Autoscoper 131

Chapter 1

Introduction

The description of human joint kinematics during daily living activity is the main goal of human motion analysis. Measurements of the 3D kinematics of the human joint during movement is important for comprehending and evaluating the function of the joint as well as for several clinical purposes such as characterizing pre- and post-operative joint motion and to enable better prosthesis design. However, measuring the in vivo dynamic biomechanics in six degrees of freedom (position and orientation) with an accuracy that is acceptable has been shown to be technically challenging. To analyze the in vivo human joint motion several techniques have been developed. Researchers have used *in vitro* (cadavers) [5, 6], noninvasive (gait laboratories) [7, 8] and *in vivo* (roentgen stereophotogrammetry and fluoroscopy) [9, 10] methods for assessing human joint motion. Cadaveric and Static X-ray measurement techniques often do not accurately reflect loads that happen during typical movements and their predicted outcome is not reliable. Therefore, treatments aimed at improving the joint function should be evaluated when the data are acquired from dynamic measurement methods which need the estimation of six degrees of freedom (DOF) of objects to be determined during dynamic activities. The most common methods for assessing dynamic movements are based on skin-mounted markers; however

these methods include errors due to skin and soft tissue motion [11]. Medical imaging such as magnetic resonance imaging (MRI) and computed tomography (CT) allow assessing movement of the underlying bone directly but limit the analysis to quasi-static conditions. Fluoroscopic imaging technique have been extensively used for the analysis of joint motion during dynamic activities. Single plane fluoroscopy has proven to be a precise method for establishing joint position along the axis parallel to the image plane with sub-mm accuracy; however it is proven to be imprecise in the out of plane motion[12]. To overcome the inherent limitations of these methods researchers have used dual plane fluoroscopy systems that directly measures three-dimensional skeletal motion with sub-millimeter accuracy. Recently we have developed a high-speed stereo radiography system with high frame rates and two view planes for three-dimensional tracking of bones and implants with sub-millimeter accuracy that offers high-speed kinematic measurements of in vivo 6 degrees of freedom (DOF) joint motion during activities of daily living. The purpose of this thesis is the calibration, validation of a high speed stereo radiography (HSSR) system and the assessment of normal knee kinematics during high demand activities in subjects age-appropriate to total knee arthroplasty (TKA) by using the HSSR system. In order to achieve this goal, we had to acquire the dose in order to be able to have the international review board approval (IRB) and recruit subjects that would participate in this study. Moreover, for maintaining the ability of the HSSR to capture the skeletal motion with sub-millimeter accuracy and resolution, alignment, distortion correction and calibration are the important steps that need to be done before the data collection. Finally, a validation study was conducted to demonstrate our system's accuracy for sub-millimeter tracking of rotations and translations for a human knee joint, implant and beads.

1.1 Motivation and Problem Statement

The measurement of dynamic knee kinematics in vivo is important in order to understand the effects of joint injuries and diseases as well as for evaluating the treatment effectiveness. Osteoarthritis appears in the knee more than any other joint and disease development and progression are affected by abnormal joint kinematics under weight bearing conditions. TKA, which is one of the most common orthopaedic knee surgeries, is an extremely effective treatment for arthritic pain or functional impotence and this treatment is used in order to substitute a deformed joint with a knee prosthesis. To investigate the characteristic knee motion is essential for assessment and design improved implants that intend to restore joint alignment and to achieve full range of knee flexion. Particularly, precise knowledge of normal knee mechanics provides useful metrics for comparison to knee function following TKA. High prevalence of knee pain, osteoarthritis, TKA occurs more frequently in older adults and movement patterns change as we age [13]. Thus, our purpose was to determine joint kinematics in healthy older adults performing common movements of daily living like straight walking and during higher demand activities in order to establish a useful baseline for the envelope of healthy knee motion for subsequent comparison with patients with TKA.

1.2 Contributions

To our knowledge, no others have evaluated normal knee function for a cohort age-matched to TKA recipients and during activities that patients with TKA often report to be troublesome, such as descending a step and executing a turn during walking. Most descriptions of knee kinematics have been for younger adults and for a limited span of activities. Furthermore, most existing dual plane fluoroscopy systems are often limited by capture

at rates less than many normal physiological movements, small fields-of-view, and static configurations. HSSR makes possible the 3D tracking of bones and implants with high accuracy with 16 inch image intensifiers that allow a field of view nearly 150% larger than most research radiography systems while the high-speed cameras and 480 volt generators allow motion capture at up to 120 fps in low-dose pulsed mode or up to 1000 fps in a continuous mode. With the HSSR system we were able to measure knee kinematics during tasks with increasing demand and to establish a useful baseline for the envelope of healthy knee motion in adults over the age of 55 that will provide the baseline knowledge for the analysis of the pathological knees and assessment of TKA function for further improvement in TKA design and rehabilitation.

1.3 Organization of Thesis

This thesis is organized as follows. Chapter 2 provides a literature review where background information on methods used to measure joint kinematics as well as techniques of joint tracking are investigated and compared with other existing methods in research. Additionally an overview of the HSSR system is introduced. Chapter 3 describes the calibration and the validation methods used in order to demonstrate our system's accuracy. Chapter 4 discusses all the precise methods used to describe healthy knee kinematics. Finally, Chapter 5 is the application of the HSSR by classifying joint kinematics in healthy older adults performing common movements of daily living like straight walking and during higher demand activities.

Chapter 2

Previous Investigations and High Speed Stereo Radiography

The measurement of dynamic joint kinematics in vivo is important in order to understand the effects of joint injuries and diseases as well as for evaluating treatment effectiveness. The main aim of human motion analysis is the description of human joint kinematics during daily living activity. Joint motion is driven by a combination of dynamic physical forces (gravitational, inertial and contact), active muscular forces and constraints imposed by passive structures. Measuring the in vivo dynamic biomechanics in six degrees of freedom (position and orientation) with an accuracy that is acceptable has been proven to be technically challenging. Numerous techniques have been developed to study the in vivo human joint motion.

2.1 Literature review-Background

2.1.1 Methods for measuring joint kinematics

There are three different approaches towards the analysis of human joint kinematics. Researchers have used *in vitro* (cadavers) [5, 6], noninvasive (gait laboratories) [7, 8] and *in vivo* (roentgen stereophotogrammetry and fluoroscopy) [9, 10] approaches to assess human joint motion. Cadaveric and Static X-ray measurement methods often do not accurately reflect loads that occur during typical movements and they do not give a reliable predicted outcome. For that reason, treatments aimed at improving the joint function should be evaluated when the data are obtained from dynamic measurement methods which requires the estimation of six degrees of freedom (DOF) of objects to be determined during dynamic activities.

2.1.2 Marker-based motion capture techniques

The most commonly used methods for assessing dynamic movement rely upon skin-mounted or bone implanted markers. Reconstruction of human movement based on skin-mounted optical markers has become a standard procedure in clinical practice. These markers are mounted and attached to the skin surface of the body segments to be analyzed. It is well established that markers placed on the skin tend to slide relative to the underlying bones because of the interposition of soft tissues. This interposition is the origin of two sources of error: anatomical landmarks mis-location and soft tissue artifacts (STA). The latter one has been recognized to be the major source of errors in human motion analysis. Much previous work has been done in quantifying the magnitude nature and effects on estimating bone motions from skin marker. Several methods have been developed to compensate for the marker cluster deformation but the problem with them is that STA can

cause unrealistic motions of the joints. These source of errors associated with STA are difficult to eliminate non-invasively. The use of skin marker-based methods to describe joint surface kinematics during motion is also difficult due to lack of joint surface information. When applied to measuring knee joint kinematics by using skin-mounted markers, soft tissue and structures surrounding the knee interfere with the actual underlying kinematics and task-displacements of individual skin-mounted markers relative to the underlying bone of more than 20 mm are reported [11]. Another example would be the measurement of 3-D kinematics of the upper extremity of the body. Upper limb motion may be spatially complex especially in the shoulder and this makes the use of markers attached to wands prone to interference with other limb segments and subject to inaccuracies from soft tissue oscillations and inertial effects.

To overcome the inherent inaccuracy of skin-mounted markers, markers have been mounted on pins and inserted into the underlying bones. Although this approach can provide high-quality kinematics data, its invasive nature as well as the risk of infection has limited its application in human movement studies. Using the bone pin technique, errors due to skin motion of up to 10 mm of translation and 8 degrees of rotation have been observed [14].

X-ray imaging avoids the problem of skin motion error, and is relatively safe and non-invasive but limits the analysis to quasi-static conditions and does not allow for 3-D measurement of joint kinematics. Existing 3D techniques such as Computed Tomography (CT) and Magnetic Resonance Imaging (MRI) allow assessing movement of the underlying bone directly although CT and MRI are not yet capable of achieving high frame rates required for estimating dynamic function. Furthermore, these methods are costly and the restrictions imposed by the imaging environment (typically a small-diameter cylindrical space) prevent full motion kinematics measurement during functional activities like walking. Finally CT/MRI will be really difficult to use with subjects that have prosthetic parts in their

bodies because of the detrimental effects of large metal objects on both modalities. The limitations of existing methods described above may be overcome by fluoroscopic/radiographic imaging, which enables direct visualization of the bone.

2.1.3 Dynamic Radiography

Until today the only way to measure the motion of structures inside the body during human motions such as walking, jumping or running is by using the fluoroscopic imaging or dynamic radiography. Dynamic radiography allows real-time tracking of joint motion by using X-ray imaging and capturing X-ray videos. Fluoroscopy, being dynamic radiography, captured at low frame rates and with low radiation energy, allows following dynamic anatomical/physiological processes in real time in vivo, with an obvious drawback of acquiring two-dimensional images. Fluoroscopy is an imaging technique where X-rays are emitted from a tube, pass through the joint and strike on a fluorescent screen coupled to an image intensifier and a video camera. Images are recorded and played on a monitor and the result is perspective projections of the joint, recorded as a continuous series of images. A preliminary CT scan or MRI imaging, allow making a 3-D bone model that can convert the 2-D fluoroscopic image with a shape matching technique. Fluoroscopic techniques provide the most direct way to measure joint motion. Single plane and biplane fluoroscopy have been used extensively to track movement inside the body with sub-millimeter accuracy. Biplane fluoroscopy is also known as dual plane fluoroscopy , 3D radiography, stereoradiography as well as other titles. Direct 3-D measurements of bone position have been investigated by using marker-based techniques and image-based techniques [15, 16, 17]. Each of these techniques is based on single-plane or dual plane X-ray exposure. The marker-based techniques require implanting radioopaque markers inside the bone. Although this method can be implemented during surgery the application of this technique to healthy subjects

is severely restricted due to ethical reasons. Finally, matching radiographic images with 3D models of bones or implants is a preferable technique for accurately measuring in vivo kinematics.

2.1.4 Single Plane Fluoroscopy

Being able to estimate three-dimensional skeletal kinematics during daily activities such as walking, is important for accurate modeling of joint motion and loading, and is necessary for several orthopaedic research applications including providing input data to modeling applications and identifying the effects of injuries and diseases. For example, accurate measurement of joint kinematics is important in understanding the pathogenesis of osteoarthritis and its symptoms and for developing methods in order to provide comfort from joint pain. Single-plane fluoroscopy has been used to track movement inside the body and measure in vivo 3D kinematics with sub-millimeter accuracy for different joints in the human body like the spine , elbow, shoulder as well as the natural and prosthetic hip, knee and ankle.

Researchers have used extensively single-plane fluoroscopy in order to measure natural knee motion and the kinematics of artificial knees [18, 12, 19]. The silhouette of a metallic component is clearly observable in a 2-D fluoroscopic image because the metallic components have precisely known geometric features and produce some edges in fluoroscopic images. The 3-D posture (6DOF) of a metallic implant can be estimated by matching the calculated projection of the implant's 3-D model with the silhouette. Several researchers have applied this technique to the measurement of natural knee motion [17, 12] however, the accuracy of their results was lower than that of studies applied to implanted knee joints due to weaker contrast of human bones and non perfect 3-D bone models.

The authors in study [12] performed an in vivo fluoroscopic analysis of the normal human knee. The objective was to use single-plane fluoroscopy and computed tomography (CT) to accurately determine the three-dimensional, in vivo, weight-bearing kinematics of five normal knees. Three-dimensional computer aided design models (CAD) of each subject's femur and tibia were recreated from the 3-D CT bone density data. Five healthy subjects subsequently did five weight-bearing activities (deep knee bend, normal gait, rising from a chair, stair descent) while under fluoroscopic surveillance. The results showed that during all five activities the lateral condyle experienced significantly more anterior-posterior translation, leading to axial rotation of the tibia relative to femur. This study provides an accurate three-dimensional, in vivo kinematic analysis of the normal knee under weight-bearing conditions, while the subjects did multiple different activities. The presented data may provide useful information for future knee simulation studies and a better baseline of kinematic data for future total knee arthroplasty design.

Another reason for using fluoroscopy to study kinematics of the knee and the significance of understanding the weight-bearing forces and shear stresses applied to bearing surfaces is that this knowledge is highly important for total knee arthroplasty (TKA). Approximately 177,000 total knee replacements (TKA) operations were performed in the United States in 1991, a 26% increase from the number implanted in 1990 in [20]. Accurate measurements of knee replacement kinematics during functional activities would provide the basis for assessing the performance of current designs and also the basis to design devices with improved kinematics. For artificial knees, single-plane fluoroscopy has been used to measure implant motion directly [21], [22]. An X-ray fluoroscopy based technique was investigated for the measurement of 3-D TKR kinematics during dynamic activities in [19]. The measurement approach is based on the concept that given the imaging geometry of the fluoroscope and the surface geometry of the prosthetic components, a computer can create an image which matches any experimentally acquired image of the knee. The kinematic

measurement approach is based on imaging the knee joint as it moves, using the single-plane fluoroscopy to obtain a sequence of images in which the prosthesis is projected as a 2-D perspective silhouette. The advantage is that it is a direct measurement of dynamic prosthetic motion and the information gained form that study will improve our understanding of how these devices are functioning in vivo. The results indicate that knee rotations can be measured with an accuracy of approximately one degree and that sagittal plane translations can be measured with an accuracy of approximately 0.5 mm. The accuracy of estimating the relative pose between knee replacement components in terms of clinical motion is important in the study of knee joint kinematics.

In Acker *et al.* [23] the accuracy of single-plane fluoroscopy in determining relative position and orientation of total knee replacement components is also investigated. Determining the accuracy of knee joint kinematics calculated by using fluoroscopy shape matching approach was accomplished by comparing it to optoelectronic motion tracking. The single-plane fluoroscopy method was used to calculate the relative pose between the femoral and tibial component, along knee motion axes, while the components were in motion relative to each other. Calibration and distortion correction parameters were defined by using a calibration image of radioopaque beads in known patterns. The kinematics of total knee replacements were determined in vitro for both methods. The mean differences between the fluoroscopic and optoelectronic poses and the corresponding limits of agreement calculated in this study shows the accuracy with which the relative pose between knee replacement components can be defined by shape-matching single-plane fluoroscopic images and then optimize the match by using an automated optimization algorithm. The mean accuracy values and limits of agreement shown from this study can be used to determine whether the shape-matching approach using single-plane fluoroscopic images is sufficiently accurate for an intended motion tracking application.

Similarly an investigation is presented for the glenohumeral translation using single plane fluoroscopy and shape matching techniques [24]. In this study the glenohumeral translation in vivo during active shoulder abduction in the scapular plane is investigated. The hypothesis was that with the arm at the side, the humeral head would be relatively inferior with respect to the glenoid and move to the center of the glenoid with arm elevation in healthy shoulders. Furthermore, another hypothesis was that kinematic variability would decrease with arm abduction. For the purpose of this study nine healthy subjects were recruited. The 3D models of the scapula and proximal humerus were created with CT scans. Fluoroscopic images aligned to the plane of the scapula were captured during active arm abduction with neutral rotation.The 3D motions of the scapula and humerus were established using model-based 3D-to-2D registration. Humeral translation was referenced to the glenoid center in the superior/inferior direction. A custom shape-matching program was utilized to acquire 6 DOF shoulder kinematics. Glenohumeral translations perpendicular to the image plane were not considered precise enough to be reported. The results demonstrated that the humerus moved an average of 1.7 mm superior with arm abduction, from an inferior location to the glenoid center. Also, all shoulders exhibited the same pattern of motion, with most variability in the data appearing to result from the definition of the glenoid center. The variability in glenohumeral transaltion among the nine shoulders reduced significantly from initial to final arm abduction. According to the authors the 3D fluoroscopic analysis of shoulder kinematics can give significant information for improved understanding of shoulder function.

One of the disadvantages, though, of single-plane fluoroscopy is that it is not precise enough in the out of plane direction [12, 16, 15]. In addition, bone edge attenuation for normal joints has been suggested to be the primary factor that limits the theoretical accuracy in measuring bone poses with single-plane fluoroscopy. These limitations may be overcome by using a dual plane fluoroscopy system.

2.1.5 Dual Plane Fluoroscopy

Dual plane fluoroscopy is the method where an additional single plane fluoroscope is oriented at an oblique angle and images are taken from both single plane fluoroscopes simultaneously. By using this method, the movement of the structures inside the body in six degrees of freedom, translation and rotation, can be determined with sub-millimeter accuracy. It is used to characterize kinematics in healthy normal and symptomatic population and can be adapted to measure high-speed human joint motion in vivo. Hip, knee and ankle kinematics during functional activities such as running or shoulder kinematics during throwing can be estimated. Since dual plane fluoroscopy has the ability to quantify six DOF joint motion with high accuracy during dynamic movements it finds many applications in orthopaedics, bioengineering and sports medicine. Accurate measurement of joint motion derived from this method helps assessing joint function and improving the design of an implant. Moreover the dual plane fluoroscopy kinematic data may be also used as input to assess deformation of joint structures, to derive contact stress distributions and for different modeling applications. This information is also essential for planning surgeries or rehabilitation therapies.

The purpose of study in Bey et al [25] was to assess the accuracy of biplane X-ray imaging combined with a new model-based technique for measuring patellofemoral (PF) joint motion. The distal femur and patella compose the patellofemoral (PF) joint. In order to validate this technique, tantalum beads were implanted into the femur and patella of three cadaveric knee specimens and then biplane fluoroscopic images were recorded while manually flexing and extending the specimen. The model-based tracking technique system as well as a dynamic radiostereometric analysis (RSA) (gold standard) were used to define the position of the femur and the patella. This CT model-based technique for precisely measuring the in vivo joint motion from biplane fluoroscopic images tracks the position of

bones by maximizing the correlation between biplane X-ray images and Digitally Reconstructed Radiographs (DRRs). Usually knee flexion is accomplished with the tibia rotating relative to a fixed femur. In this case both the femur and the patella are moving relative to a fixed tibia. The biplane X-ray images were acquired at 60 frames per second for 1.5 seconds. The model-based tracking method applies a ray-tracing algorithm to project a pair of DRRs from the CT-based bone model. By maximizing the correlation between the DRRs and the biplane X-ray images the in vivo position of the bone as well as its orientation can be estimated. The orientation and the 3-D position of the femur and patella were defined independently for all frames for each trial. Bias and precision were used in order to quantify the accuracy of this technique. Results demonstrated that the outcomes from both techniques are in high agreement. Patellofemoral joint (PF) motion is important to be accurately measured for understanding the consequences of a conservative and surgical treatment of PF pain syndrome and the results from this research showed that this technique is sufficiently accurate in measuring clinically relevant changes in PF joint motion following conservative or surgical treatment. One disadvantage of this technique is the amount of the X-ray exposure the subjects must undergo from the CT scan and the biplane fluoroscopy and that limits the number of trials that can be performed. Furthermore the field of view is constrained to the biplane X-ray system's 3-D imaging volume.

In Myers *et al.* [26] a study was undertaken to measure, describe and compare tibiofemoral rotations and translations of soft and stiff landings in healthy individuals by using dual plane fluoroscopy. Although anterior cruciate ligament (ACL) injury prevention programs have been denoted to be efficient at teaching athletes to avoid stiff landings, the overall occurrence of non contact ACL injury and surgical reconstructions remains high in both men and women. Biplane fluoroscopy systems enable the accurate measurement of 6 degrees of freedom kinematics of the knee joint during dynamic activities. The in vivo 3-D lower extremity, knee kinematics of three men and ten women, were collected as they per-

formed the landing from a 40-cm height. All subjects were instructed to perform soft and stiff landings. Stiff landings produced significantly greater ground reaction forces (GRFs) and knee extension moments but did not cause increased amounts of anterior tibial translation or knee rotation in either varus / valgus or internal / external rotation when compared with soft landings in healthy individuals under these testing conditions. The results of that study showed the ability of the musculature and soft tissues around the knee joint to keep translations and rotations of the knee within a small, safe range during controlled tasks of differing demand.

The authors in paper [27] adapted a Dual Fluoroscopic Imaging technique (DFIS) to investigate the various in vivo dynamic knee motions as well. Furthermore, a thorough validation of the accuracy and repeatability of the DFIS system was presented during measuring 6 DOF dynamic knee kinematics. For the validation, standard geometric spheres made from different materials, were used to show the capability of the DFIS method to determine the object positions under changing velocities. Cadaveric knees were used to define both the knee positions translated at a known speed and the 6 DOF knee kinematics during flexion and extension. Also this method was applied to a living subject during step ascent and treadmill gait for investigating the knee kinematics and demonstrating the in vivo utilization of the DFIS. The validation showed that knee positions and velocities can be defined by this method. One of the limitations is the restriction to activities such as treadmill gait, stair ascent or descent and lunge. The results demonstrated that DFIS, which is a non invasive technique with low radiation dose, can be used as an accurate and useful tool.

An analysis for knee prosthesis by using two X-ray sources is conducted in paper [28]. Total knee arthroplasty (TKA) is very successful in comforting pain and restoring joint function, but the implant failure remains a problem. One of the main reasons of failure is excessive polyethylene wear. Osteolysis can be induced from wear particles and may cause

complications like aseptic loosening. Excessive wear is related to the design of prothesis. In this study the accuracy and the robustness of TKA wear measurements of a model-based Roentegen stereophotogrammetric analysis (MBRSA) is investigated. An RSA setup and a knee phantom in which the separation distance between the tibia and femur is known exactly, are used for the purpose of this study. The phantom setup was used of sawbones with a total knee replacement in standing position. RSA images were obtained from two synchronized X-ray sources. The measurement method is addressed for various settings such as prostheses type, actual separation distance, digital model accuracy and patient positioning. The robustness of the method is defined by assessing the measurement error as a function of these parameters. The results showed that the joint separate measurements based on a model-based RSA are accurate enough for wear studies of knee prostheses. The limitation of this study is the lack of experiments with in vivo data in which the soft tissue attenuation can deteriorate contour detection.

A further analysis of the kinematics of knee implants was held at the Department of Orthopaedics Leiden University [29]. The authors propose an automated contour detection method which is integrated in the pose estimation. In this technique, most of the manual work in fluoroscopic analysis is eliminated and is precise enough for clinical research purposes. In a phantom experiment, with a biplane flat-panel fluoroscopic set-up, the automated method was compared with a standard method which uses manual selection of correct contour parts. It is a conventional model-based pose estimation method [30] with semi-automated contour detection, the Canny edge detection [31]. The purpose of this study is to validate the new and automated model-based contour detection method, which is integrated into a model-based pose estimation method. The analysis of a complete fluoroscopic data set can easily be automated by propagating the pose from one image to the next [32]. Both clinical data and phantom were used in order to validate the precision and accuracy of the clinically relevant in-plane positions and orientations. A fluoroscopic

image, the relative X-ray focus position, a 3-D surface model of the implant as well as an initial candidate pose are the main inputs of the automated model-based contour detection method. The results showed that the most prominent differences are in the systematic errors where in the automated method the systematic errors are consistently higher. However, the systematic errors are less important than the standard deviations when implant kinematics is investigated, where the relative positions of the components are considered. With respect to standard deviations the two methods gave the same results. Moreover the standard and the automated method employ the same technique except that the last one has a second image available from the biplane set-up and that can cause, according to the authors, the discrepancy in the systematic errors between the two methods. Overall this research demonstrated that the contour detection can be completely integrated within the pose estimation with an easier work-flow and less manual work in fluoroscopic analysis with only minor consequences for the accuracy of the system

Quantifying foot bone motion or measuring dynamic in vivo glenohumeral joint kinematics remains a challenging problem. Single-plane fluoroscopy has been used to study hindfoot kinematics; however the complex anatomy of the foot with many small occluding bones limits the system. Dual plane fluoroscopy has been successfully used instead in order to overcome this limitation [33]. The biplane fluorscope was used to capture the foot phantom with metal balls embedded on 3 bones (tibia, calcaneous and first metatarsal). The metal balls were used in order to embed fixed coordinate systems in the first metatarsal and calcaneous. The foot phantom was CT scanned and in addition DRRs of the foot phantom were generated to perform a manual alignment with the 2D fluoroscope data. Results demonstrated sub-millimeter and sub-degree accuracies (0.1 mm and 0.15 ^{0} respectively).

Many researchers have conducted research based on dual plane fluoroscopy systems for measuring 3D shoulder kinematics analysis in order to achieve significant levels of accuracy [34, 35] or to study hip joint kinematics [36]. The glenohumeral joint has the greatest

range of motion of any joint in the body and, due to its complicated anatomy, measuring the dynamic in vivo shoulder kinematics is a challenging problem. Therefore, in [35] study, the authors present the validation of a non-invasive dual fluoroscopic imaging system (DFIS) model-based tracking technique for assessing dynamic in vivo shoulder kinematics. The DFIS system tracks the position of bones based on their projected silhouettes to contours on recorded pairs of fluoroscopic images. For the purpose of this study the authors compared their tracking of the scapula and humerus bones without implantation of any markers with a radiostereometric analysis (RSA) where titanium beads were implanted in a cadaver's specimens arm. In addition, the repeatability of the DFIS to track the scapula and the humerus during dynamic shoulder motion was investigated. Their results demonstrated that this model-based tracking technique was similar to the invasive RSA gold standard technique within approximately $\pm 0.3mm$ in translation and $\pm 0.5^0$ in rotation. Furthermore, the repeatability of the model-based tracking technique for the scapula and humerus was approximately $\pm 0.2mm$ and $\pm 0.4^0$, respectively. Finally, dual plane fluoroscopy system is highly recommended for non-invasively studying the in vivo motion of the shoulder in both healthy and pathological subjects.

In Martins *et al.* study [36] a combined high-speed biplane radiography and model-based tracking technique to study hip joint kinematics and arthrokinematics is presented. Two fresh-frozen human cadaver pelvises were obtained and consisted of all bone and soft tissue from the pelvis to the midfemurs and so the study includes a total of four hip joints. Four 2-mm chrome beads were implanted into the right and left hemipelvis and right and left femur for each specimen. CT scans were collected in order to create the 3D models of the bones. Radiographic data were collected during two activities designed to simulate activities of daily living. The implanted beads were tracked using radiostereophotogrammetric analysis (RSA) and only three beads are required to perform this analysis. The 3D bone models and the radiographs were imported into a custom software that automatically

manipulates the bone model's position for better alignment with the 2D images in order to determine the position of the bone. Results from the comparison of model-based tracking technique to the gold standard RSA using implanted beads showed a bias of 0.2 mm and a precision 0.3 mm for joint translation and for joint rotation the bias was 0.2^0 and the precision was 0.8^0. Therefore model-based tracking technique of the hip provides the ability to study hip pathologic conditions noninvasively with high accuracy.

For measuring in vivo six DOF vertebral motion during unrestricted weight-bearing functional body activities the authors in study [37] used a combined MR and dual fluoroscopic imaging technique. Eight healthy subjects participated in this study and all subjects underwent MRI scans in order to construct 3D vertebral models of L2,L3,L4 and L5 of the lumbar spine for each subject. Then the target spinal segments were captured using the dual plane fluoroscopic system while the subject performed several activities including primary flexion-extension, left-right bending and left-right twisting. The range of vertebral motion during each activity was defined at L2-3, L3-4 and L4-5 levels. The MR image-based 3D vertebral models along with the 2D fluoroscopic images were imported into the Rhinoceros solid modeling software and after the alignment f the 3D models in the 2D images the vertebral positions during in vivo weight-bearing activities were reproduced and in that way establishing the 6DOF kinematics of the vertebrae at each in vivo position. Findings from this study demonstrated that the upper vertebrae had a greater range of flexion than the lower vertebrae during flexion-extension of the body. During bending activity the L4-5 had a greater range of left-right bending motion than both L2-3.

The accuracy of the dual plane fluoroscopy system is substantially higher than single plane since it is imprecise in the out of plane direction. As an example, in [27] dynamic accuracy of dual plane fluoroscopy for the healthy knee was reported to be 0.24mm and 0.16 degrees for translations and rotations respectively while for single plane in [38] the translations and rotations were 2.00mm and 1.5 degrees respectively [39].

However, most existing dual plane fluoroscopy systems are often limited by capture rates less than physiological movement, recording joint motion in small fields of view and the majority of these systems are static configurations since most of the X-ray equipment is mounted on large C-arms that can not move freely in space. This volume constraint, limits the number of dynamic activities and joints that can be captured.

2.2 Methods of tracking

This part of the literature review presents a study of current research activities going on the Universities and Research Centers around the globe in the area of joint tracking. The purpose of this literature review is to gather and explain some of the available methods that have been used to track and measure joint motions derived from X-ray imaging and is organized as follows: The first section discusses the measurements of joint motion based on bead tracking. In the second section current research based on implant tracking is presented while in the last section a summary of papers referring to joint motion based on bone tracking are presented. At the end, Table 2.1 summarizes the results of the techniques that are presented in this study.

In most of the papers that are described herein radiostereometric analysis (RSA) is used as a reference technique. Dynamic radiostereometric analysis (RSA) technique is a well established and widely accepted method for measuring joint kinematics by tracking the position of implanted tantalum beads. This technique utilizes ray trace intersections of implanted metallic spheres to determine the three-dimensional position of objects in space [34, 40, 27]. Because it is widely accepted it is extensively used as the gold standard for measuring relative bone and implant motion.

2.2.1 Section I: Bead Tracking

A study was conducted at the Bone and Joint Center on a novel technique for measuring in-vivo skeletal kinematics that combines data collected from high-speed biplane radiography and static computed tomography (CT) [41]. The purpose was to demonstrate that sufficient precision can be obtained by combining high frame-rate biplane video-radiography with analysis methods close to RSA during dynamic movement and to introduce a method for expressing joint kinematics in an anatomically relevant coordinate system. This method is applied for studying canine ACL deficiency though this technique has been applied similarly to human studies. The four components that were used in order to implement this method are: a) a hardware system for generation and acquisition of high frame rate biplane radiographs b) a software package for identification and 3-D tracking of bone markers c) a CT-based system for coordinate system determination and d) a set of kinematic analysis routines for determining joint motion in anatomically based coordinates. Similarly to static RSA, implanted radiopaque tantalum bone markers were employed to enable accurate registration between the two views. Markers were implanted in the distal femur and proximal tibia in order to maximize inter-marker spacing and to avoid marker overlap. Then the radiographic process introduces significant defects in the acquired images that must be corrected to minimize 3-D tracking errors. These errors are corrected before image processing and 3-D tracking. Software was developed to search for marker signatures in each image frame. The resulting 2-D coordinates were saved in a format compatible with the motion analysis software EVa (EVa, Motion Analysis,corp.). The EVa software was used to perform 3-D camera calibration and coordinate reconstruction by using the calibration cube data and a modified Direct Linear Transformation (DLT) [42]. 3-D bone models were developed from CT and they were used to determine the transformations between instrumentation-based and anatomically based coordinate systems. Locations of the tanta-

lum markers within the bone were determined from CT slices using the public domain NIH image program (developed at the U.S. National Institutes of Health). Then joint rotations and translations were calculated. The resulting angles for joint rotations are those described by Grood and Suntay [43] and the joint translation is defined as the relative displacement between specific points fixed to each bone.

Precision and repeatability were estimated for in-vivo data and assessed using inter-marker distance while bias was estimated from phantom tests. Bias measurements were within the accuracy of the precision milling equipment used to construct the phantom object and were not significantly different from zero. The level of the precision is sufficiently accurate and is attainable on live objects performing dynamic movements. Angular errors were reported based on actual, implanted marker configurations and are dependent on the specific geometry of the markers implanted into each bone. One limitation of this technique is the need for CT data from proximal joints near internal organs. This approach can be used whenever the benefits of very high accuracy outweigh the minimal risks and is well suited for implementation and validation of dynamic musculoskeletal models for estimating in-vivo behavior of internal joint structures.

Marker Configuration Model-based Roentgen Fluoroscopic analysis (MCM-based RFA) is introduced in [44] in order to evaluate how the polyethylene bearing in mobile bearing knees moves during dynamic activities with respect to the tibial base plate. This technique uses a marker configuration model of inserted tantalum markers in order to accurately estimate the pose of an implant or bone by using single plane Roentgen images or fluoroscopic images. The accuracy of this method is investigated in a standard fluoroscopic set-up using phantom experiments and also this study determines the error propagation of the accuracy of 3D marker position reconstruction with computer simulations. This technique uses an MC-model.

MC-model describes the positions of the markers relative to each other and this can be assessed by the reconstructed 3D positions of the markers from one or more RSA radiographs using RSA software (RSA-CMS, Medis, The Netherlands).

The 2D positions of the marker projections in the fluoroscopic images are automatically detected with an algorithm based on the Hough-transform for circle detection [45]. A calibration box has been used for calculating the 3D position of the Roentgen focus by the same procedure as in RSA [46]. This procedure is further explained in detail in the paper. To be able to correct for distortion and calibrate the set-up a 400x400 mm Perspex calibration box (BAAT Engineering B.V., Hengel, The Netherlands) was used. In the phantom experiments this calibration box was utilized to obtain the 3D position of the focus and to define the coordinate system. A two-dimensional N-degree polynomial model was used to quantify the distortion and calculate the correction parameters. Also for the phantom experiments the phantom used was made of carbon fibre sandwich plates and contained 17 1-mm tantalum beads attached to each edge. Two rigid bodies define two MC-models within the phantom. The relative change between the two MC-models in position and orientation was calculated by comparing their relative pose in two consecutive images. These relative changes indicate the error of the MCM-Based RFA method [47]. Based on the results of the phantom study, the error propagation of this technique was assessed by computer simulations using MATLAB (The Mathworks Inc.,Natick, MA). Five types of simulations were performed in order to separately investigate the influence of image distortion, MC-model accuracy, focus position, the relative distance between MC-models, and MC-model configuration on the accuracy of MCM-Based RFA. In each type of simulation, ten levels of normally distributed noise with zero mean and set standard deviation was added to the data of test parameters. These simulations are described in the paper.

The results showed that the highest distortion was found at the boarders of the field of view. A ninth-order polynomial model was used to correct for image distortion. The

phantom study established that the in-plane accuracy of this method is 0.1mm and the out of plane accuracy is 0.9 mm. The rotational accuracy is 0.1 degrees.

From the computer simulations the results showed that the out of plane measurement error was the most sensitive when noise was added. The measurement error of MCM-Based RFA is linearly related to the amount of model distortion. Image distortion and accuracy of models have the largest influence in the accuracy of the method. In the worst case the results showed that the in vivo measurement accuracy for translations is estimated to be 0.14 mm (x-axis), 0.17 mm (y-axis), 1.9 mm (z-axis) and a rotational accuracy of 0.3 degrees. MCM-Based RFA is potentially an accurate clinical useful tool for studying kinematics after total joint replacement using standard equipment.

2.2.2 Section II: Implant Tracking

At the Department of Orthopaedics Leiden University, kinematics of knee implants is investigated [29]. The authors propose an automated contour detection method which is integrated in the pose estimation. In this technique, most of the manual work in fluoroscopic analysis is eliminated and is precise enough for clinical research purposes. In a phantom experiment, with a biplane flat-panel fluoroscopic set-up, the automated method was compared with a standard method which uses manual selection of correct contour parts. It is a conventional model-based pose estimation method [30] with semi-automated contour detection, the Canny edge detection [31]. The purpose of this study is to validate the new and automated model-based contour detection method, which is integrated into a model-based pose estimation method. The analysis of a complete fluoroscopic dataset can easily be automated by propagating the pose from one image to the next. Both clinical data and phantom were used in order to validate the precision and accuracy of the clinically relevant in-plane positions and orientations. A fluoroscopic image, the relative X-ray focus posi-

tion, a 3-D surface model of the implant as well as an initial candidate pose are the main input of the automated model-based contour detection method. In order to compare the new automated and the standard method the error in pose is calculated as the difference for each pose parameter with respect to the pose obtained by the biplane reference measurement. The initial pose of the model for the new method can be provided by an experienced user. For the standard model-based pose estimation method the user is responsible for the Canny edge detection and then the pose is estimated with iterative inverse-perspective matching followed by a global optimization of the distance between the contour points and the implant model.

The results showed that the most prominent differences are in the systematic errors where in the automated method the systematic errors are consistently higher. The precision was comparable for both methods with a minor difference in the Y-position (0.08 versus 0.06 mm). The precision of each method was so small (below 0.2 mm and 0.3^0) that both are sufficiently accurate for clinical research purposes. Moreover the standard and the automated method employ the same technique except that the last one has a second image available from the biplane set-up and that can cause, according to the authors, the discrepancy in the systematic errors between the two methods. Overall this research demonstrated that the contour detection can be completely integrated within the pose estimation with an easier workflow and less manual work in fluoroscopic analysis with only minor consequences for the accuracy of the system.

Similarly in Mahfouz et al [21] a method is presented for registering 3D knee implant models, but in this case to single plane fluoroscopic images. Although this research is focused on total knee arthroplasty (TKA) this method, according to the authors, can be applied to other implanted joints as well. Single plane fluoroscopy has been used because it allows the patient free motion in the plane between the X-ray source and the image intensifier in comparison with the biplane fluoroscopy that limits the motion of the patient.

All six degrees of freedom of the pose from a 2-D image can be recovered with an accurate geometric model of the object and an accurate model from the imaging sensor, from which the image was formed. This new method that estimates the kinematics of TKA knees from single plane fluoroscopic images is a robust method with respect to image noise, occlusions and low object-to-background contrast. Unlike previous techniques in this case an accurate segmentation of the implant silhouette in the image is not necessary and instead a direct image-to-image similarity measure was utilized. In this approach, a synthetic fluoroscopic image of the implant in a predicted pose is produced and this image is correlated to the original input image. In that way explicit segmentation is not necessary but gives numerous local minima that can produce false registration solutions. This problem is overcome by using a robust optimization algorithm that finds the global minimum, avoids local minima and minimizes the error between a predicted and an actual X-ray image. This technique involves four elements: 1) an initialization step, 2) a matching algorithm which evaluates the match between the observed image and the predicted image from the current hypothesized pose, 3) a robust optimization algorithm and 4) a method of supervisory control. All these elements are described in detail in the paper [21] .

Experiments were conducted in order to analyze the convergence properties of the algorithm and to measure how well the registration algorithm could find the best pose of the femoral component, when it was run from different starting conditions. Accuracy tests showed that the registration method is highly accurate for measuring relative pose with the exception of Z translation. A completely independent method using an optical sensor was used for determining the ground truth pose data that were used as a gold standard. The overall rms difference in translation was approximately 0.65 mm and the rms error in rotation was approximately 1.5 degrees.

Additionally in Acker et al [23] a study was conducted to determine the accuracy of total knee replacement kinematics in vitro that was established via fluoroscopic shape matching

software and optimization algorithm by comparing it to optoelectronic motion tracking. By using a custom synchronization software, trials were recorded simultaneously using a C-arm fluoroscope and an Optotrack Cercus Camera. During five dynamic trials the femur Sawbone was manually moved through a knee extension cycle. In order to correct all trial images, calibration and distortion parameters were established using a calibration image of radiopaque beads in known patterns. The computer aided design models (CAD) and the undistorted images were imported into an open source shape matching software program (JointTrack, University of FLorida, Gainesville, FLorida). By manually adjusting the position and orientation of the CAD models on the display, the contour of the CAD model was manually matched to the extracted contour of the respective component in the fluoroscopic image. When the two shape outlines match then the poses were optimized. The optimization algorithm was based on the technique described in [21]. The evaluation of the shape matching between the two images was dependent on the combination of two variables. The first variable was a correlation on the intensity values of the two images while the second was a correlation on the shape contours. According on [21] results, the edge contour detection weights more than the intensity correlation. The results from this study showed that the largest absolute mean differences in relative pose between the fluoroscopic and optoelectronic results were 2.1^0, 0.3^0 and 1.1^0 in extension, abduction and internal rotation respectively and 1.3, 0.9 and 1.9 mm in anterior, distal and lateral translations, respectively. These results can be used to decide if the fluoroscopic shape matching method described here is adequately accurate for an intended motion tracking application.

Similarly in Sharma et al [48] the same shape matching technique was used in order to measure patellofemoral (PF) and tibiofemoral (TF) kinematics before and after total knee replacement. The goal for this study was to develop and validate a novel in vivo sequential biplane radiological methods that allows accurate tracking of the PF and TF

joints, throughout the range of movement under weightbearing, before and after the total knee replacement. The shape matching of the 3D bone or implant CAD models to the 2D calibrated and undistorted images is perfomed by using the biplane version of JoinTrack software (JointTrack Biplane, University of FLorida, Gainesville, FLorida). As already described previously this software rotates and translated the 3D model, manually or automatically until the two shapes are perfectly aligned, whether pre- or post-operative. The results showed that the TF kinematics and PF kinematics were highly accurate ($<$0.9mm,$<0.6^0$) and repeatable.

2.2.3 Section III: Bone Tracking

Bone tracking is based on three-dimensional shape and texture of the bones. The methods of tracking bones are based either on the contour detection or on gray-scale detection.

Researchers at the Bone and Joint Center, Henry Ford Hospital, investigated the accuracy of a new non invasive model-based tracking technique for measuring three-dimensional in vivo glenohumeral joint kinematics [34]. They compared this method with a well established, accurate dynamic RSA technique that measures joint kinematics by tracking the position of implanted tantalum beads.

New model-based tracking technique is based on the following concept: Given the geometry of the biplane x-ray system and a 3-D bone model, which is taken from a CT scan, a pair of digitally reconstructed radiographs (DRRs) can be generated via-ray traced projection through the 3-D bone model. The in vivo position and orientation of a given bone can be estimated after the optimization of the similarity between the two DRRs and the actual 2-D biplane radiographic images. In order to enhance the matching process a sobel edge-detector is added to the base images for both the DRRs and the radiographs. Sobel edge detection works by calculating the gradient of the image intensity at each pixel. The

end result is that it produces a value which correlates to how abruptly the image changes at each pixel. In that way edges can easily be detected.

After developing the 3-D volumetric bone model the model-based tracking process is performed with a workbench designed by the authors. The graphical tools obtained in this workbench are described in detail in the paper. In order to get a good visual match between fluoroscopic images and DRRs for both biplane views, initial estimates for bone position and orientation were obtained by manually adjusting the six motion parameters. The quality of the initial guess is measured from the program by: 1) generating a DRR for each of the biplane views then 2) adding a sobel edge detector output to the original DRR for the enhancement of each view, 3) calculating the correlation coefficient for each DRR 4) and finally multiplying the two correlation coefficients to get a system-correlation measure. By using this technique the 3-D position and orientation of the parts of the body that are captured were determined independently for all frames for each trial. RSA involves the determination of the position of the tantalum beads within the CT bone model and then expressing their 3-D position relative to a fixed laboratory coordinate system [41].

This research showed that the results from the new model-based tracking technique are in high agreement with the RSA technique. Measurement bias ranged from -0.126 to 0.199 mm for the scapula and ranged from -0.022 to 0.079 mm for the humerus. Precision was better than 0.130 mm for the scapula and 0.095mm for the humerus. Particularly the results indicate that the new model-based tracking technique is accurate to within approximately $\pm$0.5 mm of high accuracy validated dynamic RSA technique.

The accuracy in the same new model-based tracking technique is investigated but now is applied for measuring the patellofemoral joint motion [25]. To assess the accuracy of this technique model based tracking is compared again to dynamic RSA by computing measures of bias, precision and overall dynamic accuracy of four clinically-relevant kinematic parameters. For the validation of this technique, small beads were implanted into

the patella and femur of three cadaver knee specimens, biplane radiographic images were recorded while manually flexing and extending the leg, then the position of femur and patella was measured with both techniques and finally the results of the model-based tracking technique and the RSA which is considered to be the ”gold standard”, were compared.

According to the authors, the results of both procedures are in high agreement. Model based-tracking is a non-invasive technique and the level of accuracy that it achieves is sufficient enough for addressing clinically relevant questions regarding PF joint function. Overall dynamic accuracy was better than 0.395 mm for the three translational measurements and better than 0.877 degrees for rotational measurements.

On the other hand one disadvantage is the amount of x-ray exposure that limits the number of trials that can be performed and the field of view is limited to the biplane x-ray system's 3D imaging volume.

Another application of the same technique is presented by accurately measuring the three-dimensional motion of the shoulder's glenohumeral joint under in vivo conditions [49]. In this study the application of the new model-based tracking technique is demonstrated for accurately measuring glenohumeral joint translations during shoulder motion in the repaired and contralateral shoulders of patients following rotator cuff repair. The results from this study showed that superior-inferior humeral translation during elevation indicated an overall range of approximately 2.6 mm which is in agreement with previous works [50]. Also the anterior-posterior humeral translation was measured during external rotation (1.5 mm for repaired shoulder and 2.1mm for contralateral shoulder) which is in agreement with previous reported studies [51]. The data failed to detect statistically significant differences between the repaired and contralateral shoulders in superior-inferior translation (p=0.74) or anterior-posterior translation (0.77).

In Giphart et al [52] the accuracy of a contour-based biplane fluoroscopy tracking knee kinematics technique is investigated by comparing it to a marker-based method during

three knee movements with increasing intensity. The purpose of this in vitro study was to demonstrate weather this contour-based tracking of the knee was equally accurate across a range of motions of different speeds.

The 3D geometries of the bones were reconstructed from the CT data while the marker models of the beads were created in Model-Based RSA. Model-Based RSA was also used to determine the 3D bone and marker positions and orientations from the biplane fluoroscopy data. A canny edge-detection filter was used for the bones so the edges will be automatically detected in the fluoroscopic images and manually assigned as contours of the femur and tibia/fibula. The position and orientation of the 3D bone models was adjusted in 3D space in a way that contours from the projections of the bone models (black lines) align well with the bone contours identified in the 2D images (light lines). The markers were automatically identified in the 2D images and the pose of the marker models was adjusted so that the marker positions match well with the projection lines. The results demonstrated that the average bias and precision was $0.01 \pm 0.65\ ^{0}$ for rotations and 0.01 ± 0.59 mm for joint translations. According to this study the contour-based method showed sub-millimeter and sub-degree accuracy and it can be used as a tool for measuring complex 3D knee movements for different speeds.

In [17] the authors quantify relative and absolute accuracy limitations due to the shape matching process alone when natural knee kinematics are measured by aligning flat-shaded, edge detected bone models to single plane fluoroscopic images. For the shape matching procedure, implant 3-D computer aided design (CAD) models are replaced with geometric bone models created from medical imaging data. In fluoroscopic images, cortical bone edges are less well defined than are metallic implant edges. For that reason, a theoretical accuracy assessment is needed to quantify expected errors in measured joint (relative) and bone (absolute) kinematics. The results indicate that biased edge detection is the primary factor limiting the theoretical accuracy of this single plane shape matching procedure. In

addition this approach is insufficient for measuring in vivo contact areas for arthritis-related research applications. Biplane fluoroscopy should be used to overcome that limitation.

Massimini et al [35] presents the translation and rotation differences between a non-invasive markerless dual fluoroscopic imaging system (DFIS) model-based tracking technique for calculating dynamic in-vivo shoulder kinematics with respect to widely accepted RSA marker based technique during simulated dynamic shoulder motion. Additionally the repeatability of the DFIS to track the scapula and humerus during dynamic shoulder motion is reported. The technique of model-based tracking which started for stereophotogrammetry includes a ray trace which is constructed from a point to an image plane to the source location from two or more independent views. The 3-D position of an object can be determined by simultaneously tracking multiple points on the object. This method can determine the 3-D object position based on its projected silhouette to segmented contour in place of individual points. In this case humerus bone and scapula were manually segmented from the fluoroscopic images within the virtual DFIS. Bone models of the scapula and humerus with titanium spheres removed, were manually translated and rotated within the virtual DFIS until their alignment of their projected silhouettes with the segmented contours was achieved simultaneously on both image planes. In order to compare the two methods, the relative position and orientation were determined for both techniques. Furthermore the repeatability was investigated by tracking the position of the scapula and humerus with respect to fixed laboratory coordinate system. The results for this research showed that the difference between the markerless model-based tracking technique and the RSA was ± 0.3 mm in translation and $\pm\ 0.5^o$ in rotation. In addition the repeatability of the DFIS method for the scapula and the humerus was ± 0.2 mm and $\pm 0.4^o$, respectively.

Miranda et al [53] introduced a new markerless tracking software in order to describe a method for quantifying the systematic error of biplane fluoroscopy system. Independent gold standard instrumentation was used to evaluate the systematic error of the W.M. Keck

XROMM Facility's biplane videoradiography system using both marker-based and markerless tracking algorithms under static and dynamic motions.

In order to process all marker-based data custom Matlab software (Xrayproject) has been developed by using standard Direct Linear Transformation (DLT) techniques. Markeless XROMM can be performed by auto-registration of a CT volume in the 2D images. The auto registration algorithm consists of four major components. Digitally reconstructed radiographs (DRRs) are generated form a CT volume. Secondly both the radiographs and the DRRS are processed to detect edges and enhance features. Then a normalized cross correlation is utilized to evaluate the similarity between the DRRs and the radiographs. Finally, an optimization algorithm iterates over the 6 DOF motion parameters until the desired result has been achieved. The autoregistration algorithm needs an initial guess of the pose of the bones and this can be done either manually or extrapolated form the previous tracked frames. There are some parameters that allow the user to manipulate either the DRRs or the radiographs. Additional filters are available such as contrast and edge detection that can be applied to both DRRS and radiographs. This auto-registration algorithm has been implemented in an open source software Autoscoper (Autoscoper, Brown University, Providence, RI, USA) (see also Appendix B). Bone tracking over a video sequence can be performed with this software. The results from this study demonstrated that both techniques described here are in high agreement with the gold standard instrumentation for both static and dynamic activities.

The same markeless tracking software, Autoscoper, was used to process the biplane radiography data in [54]. In this paper the focus was on comparing kinetic and knee kinematic measurements for male and female ACL-intact and ACL-reconstructed subjects during a jumo-cut maneuver using dual plane fluoroscopy. The results demonstrated that the rotational and translational tracking precision for this work was 0.08 ^{0} and 0.45 mm, respectively.

Conclusions

Based on the literature review, it may be stated that most of the above techniques achieved high accuracy and can be very useful for establishing joint tracking. Model-based tracking technique that was introduced from the group of Bone and Joint center achieves high accuracy levels for measuring in vivo glenohumeral and patellofemoral joint motion. Additionally, the open source Autoscoper tracking software that makes use of a modern GPU technology, seems to be a highly accurate and useful tool for bone tracking. The automated contour detection method for the knee implant kinematics has also sufficient accuracy for clinical research purposes and by using this technique most of the manual work in fluoroscopic analysis is eliminated. Another software that has been used for either bone or implant tracking is JointTrack and the studies showed that it can be successfully used for radiographic model-image registration. Marker Configuration Model-Based Roentgen Fluoroscopic Analysis (MCM-based RFA) technique has the potential to be an accurate clinically useful tool for studying kinematics after total joint replacement using standard equipment.

Category	Methods	Accuracy		
Bones	**New Model-Based Tracking Method (M.J. Bey et al)**	**Bias**	**Precision**	**Overall Dynamic Accuracy**
		0.126 to 0.199 mm (S), -0.022 to 0.079 mm (H)	0.130 mm (S), 0.095 mm (H)	0.385 mm, 0.25Â°(S), 0.374 mm ,0.47Â°(H)
		-0.174 to 0.248 mm (P), -0.022 to 0.218 mm (F)	0.062 mm (P), 0.049 mm (F)	0.335 mm (P), 0.276 mm (F)
	DFIS model-based tracking method (D.F. Massimini et al)	**Repeatability**	**Average difference**	**Model Tracking error**
		±0.23 mm,±0.42Â° (S) ±0.13 mm ,±0.44Â° (H)	0.27 ±0.19mm (S) 0.49±0.36mm (H)	0.3mm and 0.5^0
	Contour-based biplane fluoroscopy method (J.E. Giphart et al)	**Bias and Precision**		
		0.01 ± 0.65^0 0.1 ±0.59 mm		
	Markerless Tracking Software (Autoscoper) for Biplane fluoroscopy Data (Miranda et al)	**Absolute Dynamic error**	**Tracking Precision**	
		within 0.15^0 of (F), (R) and (U)	0.08$ˆ0%and 0.45 mm for (F) and (T)	
	Model-Based Shape Matching with Single Plane Fluoroscopy (B.J. Fregly et al)	**TF pose**	**PF pose**	
		2mm and 1.5^0	2mm and 3^0	
Implants	**Automated Contour Detection (A.H. Prins et al)**	**Precision**		
		0.2 mm and 0.3^0		
	Robust Method for Registering 3D Knee Implant Models to Fluor. Images (M.R. Mahfouz et al)	**Convergence test**	**Accuracy test**	
		0.1 mm and 0.4^0	0.65 mm and 1.5^0	
	Single-Plane Fluor. shape matching (JoinTrack) and Optoelectronic matching method (S. Acker et al)	**Average Error Between Methods**		
		within 2.1^0 and 1.9 mm		
	JointTrack Biplane Software (G.B. Sharma et al)	**Mean accuracy**		
		0.9mm and 0.6^0 for (F) and (T)		
Beads	**MCM-Based RFA, (Eric.H.Garling et al.)**	**Accuracy translational**	**Accuracy Rotational**	
		0.14 mm(X-axis) ,0.17 mm(Y-axis), 1.9 mm (Z-axis)	0.3^0	
	Biplane Radiography and CT (Scott Tashman et al.)	**Precision (Implanted markers)**		
		0.064 mm and 0.32^0		

Table 2.1: **Summary of the results based on the techniques presented in this study**.(S): Scapula, (H): Humerus, (P):Patella, (F): Femur, (PF): Patello-femoral displacement, (FT): Femoro-tibial displacement, (R): Radius, (U): Ulna, (CA): Contact areas displacement.

2.3 Overview HSSR at the university of Denver

For diagnosing joint disorders or establishing joint treatment, precise kinematic measurements of in vivo human joint motion are required often at millimeter scale. Measurement of bone-to-bone or implant kinematics with the necessary sub-millimeter accuracy cannot be provided from traditional optical motion capture systems. Based on the literature review, dynamic radiography can capture in vivo joint motion with high accuracy. However, most fluoroscopy-based radiography systems are limited to a single plane, resulting in reduced out-of-plane accuracy. Even most existing bi-plane fluoroscopy systems as already stated are often limited by capture at rates less than many normal physiological movements, small (<12 inch) fields-of-view, and static configurations. To overcome all these limitations we have developed a High-Speed Stereo Radiography (HSSR) system which is a 3D imaging tool for dynamic measurement of bone and joint motion at a sub-millimeter level (Figure 2.1).

Figure 2.1: The HSSR system configuration

Each imaging plane of the HSSR system consists of an X-ray source and collimator where the last one reduces the size and shape of the X-ray beam according to the volume

of interest we want to irradiate on the subject and the image intensifier (II) that converts X-rays into a visible image. Furthermore high speed, high definition cameras are used for recording the resulting image. All these radiography components (Figure 2.2) of each image plane are mounted on a custom gantry that allows imaging of a wide range of joints including cervical spine and shoulder, arm and hand, foot and ankle, knee, hip and lumbar spine.

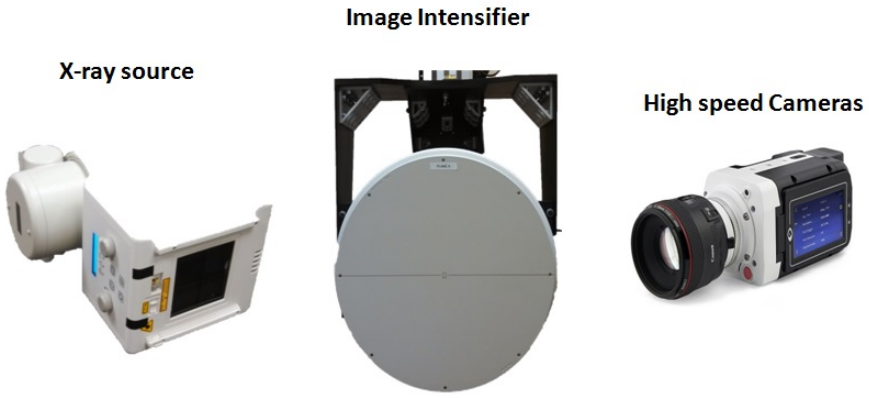

Figure 2.2: Radiograpchic components

HSSR is easily reconfigurable since it allows 8 vertical feet of travel of the radiography components on the actuators, from foot to cervical height and also the distance from the X-ray source to the image intensifier can be varied from 1.00 to 1.600 m in order to enable enough capture area for different dynamic activities. Once the gantries, each for one imaging plane, are in position they can be made rigid by using the lockable clusters. The 16 inch image intensifiers allow a field of view nearly 150% larger than most research radiography systems (approximately 40x40x40 cm^3) while the high-speed cameras and 480 volt generators allow motion capture at up to 120 fps in low-dose pulsed mode or up to 1000 fps in a continuous mode.

Finally, to achieve our research goals for human movement capture, the HSSR system is integrated into an existing marker-based camera system and forceplates. The optical motion capture system consists of 8 Vicon MX near-infrared cameras (Vicon, Oxford, UK) that can capture trajectories of spherical surface markers that define anatomical segments on human subjects. Also four force plates (Bertec, Columbus, OH) that are located within the floor capture ground force data at the same time with the video motion capture.

Our new developed High-Speed Stereo Radiography (HSSR) system provides the capability of capturing human joint motion with high frame rates, larger viewing volume, an open capture area, and two view planes for three-dimensional tracking of bone and implants with sub-millimeter accuracy.

Chapter 3

Calibration and Validation of HSSR System

3.1 Introduction

Generally, dual plane fluoroscopic imaging systems are considered to be the most precise systems for measuring joint kinematics in vivo with sub-millimeter accuracy. Accurate calibration methods for biplane systems are used in order to correct for the image distortion of the imaging devices, to determine the focus position of each X-ray generator relative to its corresponding imaging device and to accurately estimate the geometric relationship of the two fluoroscopy systems. There are three major steps to capture accurate images with the HSSR system: alignment, undistortion, and calibration.

3.2 Alignment

If the fluoroscopy system is moved though, then prior to calibration methods the alignment of the X-ray source and the image intensifier must be verified. With the HSSR the

X-ray generator must be aligned such that the X-ray beam is orthogonal to and centered on the image intensifier. Alignment is achieved using lasers and lights that are built into the X-ray source. For vertical alignment the lasers are aligned with the horizontal line on the image intensifier while the cross hair shadows coming from the X-ray generator are centered over a small icon in the center of the image intensifiers and are used for lateral alignment. The final step is to place mirrors flush with the face of each image intensifier (II). The lasers embedded in the II's are then projected on the mirrors from the corresponding plane. The reflection cast back on the X-ray source can be checked to ensure it falls between a mark above and below the laser projection, corresponding to being withing 1 degree of perpendicular. This is a necessary procedure since misalignment can reduce the image contrast, waste X-ray exposure and reduce the field of view. Once alignment is achieved, the distortion created by the II's is then quantified.

3.3 Distortion Correction

Fluoroscopic images tend to have significant geometric distortion due to the image collection from the lens and image intensifier and that must be corrected for accurate measurements. Image undistortion can be achieved by imaging a low-tolerance perforated steel sheet with known distances between the holes (3.18 mm diameter holes spaced 4.76 mm apart in a staggered pattern (9255T641, McMaster-Carr, Robinson, NJ)) that were cut to fit the face of the image intensifiers. This flat plate is directly positioned in front of the surface of the image intensifier as shown in Figure 3.1. After the grids are placed on the image intensifiers a single image is captured using technique characteristics of 50 KV, 80 mA, 24 frames/sec with 0.8 msec pulse-width. The idealized geometry of the perforations in the images can then be used to correct any distortions and to provide a distance measure to the pixels of the images by using the XROMM Undistorter (Brown University,RI)

software. A distortion correction algorithm compares the spacing between holes as seen in the fluoroscopic image with the idealized spacing and then a transformation matrix is calculated for correcting the images. The transformation from the distorted image to the corrected image after being estimated is applied to all subsequent images.

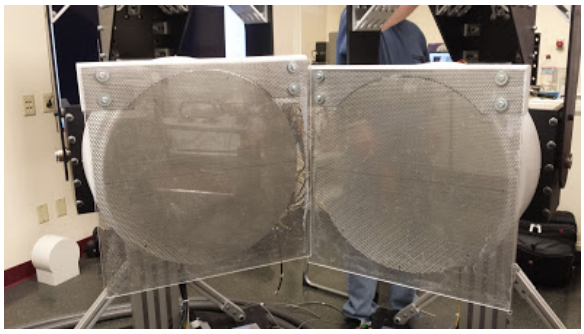

Figure 3.1: Grids placed in front of the surface of the image intensifier

Figure 3.2 shows the raw distorted image and undistorted image of the steel grid. After the correction the image is smaller because close to the edges the distorted holes have been reduced to their initial size.

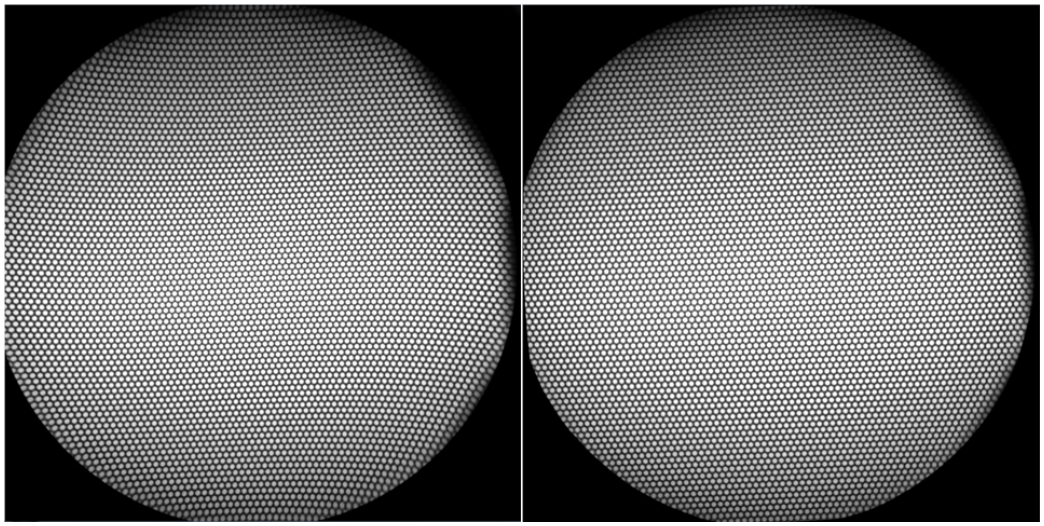

Figure 3.2: Raw distorted image of a machined steel plate with precise hole sizing and spacing on the left and undistorted image on the right

3.4 Calibration

In order to calibrate the 3D space and determine the relative positions and orientations of the each fluoroscopy system a radio-translucent thermoplastic calibration cube with 24cmx24cmx20cm dimensions has been designed enclosing 52 tantalum beads with a diameter of 2 mm and 6 mm as calibration points. The calibration cube consists of four delrin plates with uniform thickness and five stiff plastic rods that are glued in place and hold together the calibration object. The calibration cube and the position of the beads on the plates is illustrated on Figure 3.3. Some of the beads are signified with radio opaque metal icons for further help in orientation and numbering. Additionally, the size of the beads alternate between each level.

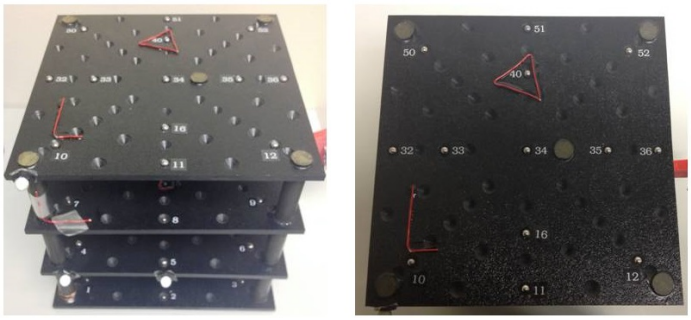

Figure 3.3: Calibration cube with 52 steel beads

The exact position of the beads was obtained by a coordinate measuring machine (CMM) with accuracy of 0.001 in. The 3D relationship of the two fluoroscopy systems is determined after imaging this custom made calibration cube positioned inside the capture volume of the stereo system. The two images are then imported into an open source calibration tool developed by Brown University, which determines the position and orientation of the image intensifiers relative to the calibration cube using a direct linear transformation (DLT) algorithm. DLT is a method of calculating the 3D location of an object (or points on an object) in space using two views of the object and describes a direct connection be-

tween 3D coordinates and image coordinates ([55]). At least 12 calibration points should be visible in both views and four of them should be the ones highlighted with metal rings for simplicity. The technique factors used for capturing the calibration cube were 50 KV, 80 mA, 24 frames/sec and 0.5 msec pulse-width. The undistorted images are imported into this software as well as the framespec file that contains the exact coordinates of the beads from the CMM. Figure 3.4 demonstrates the interface of the software when the images of the two cameras are loaded.

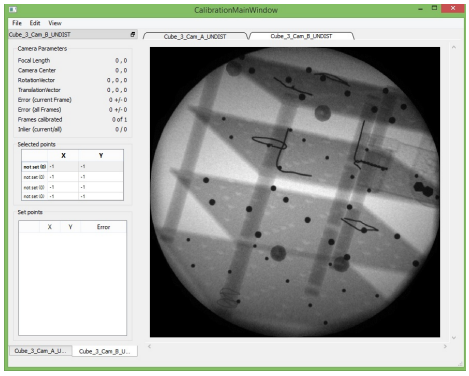

Figure 3.4: XROMM calibration interface

The next step is to load a reference file that contains only four beads as a starting guess, preferably the highlighted ones that are always inside the capturing volume, and mark the reference points onto the image of the first camera. The order and the reference points are shown in the sidebar. After selecting the four reference points the position of the camera can be computed and all the visible points are now being selected and camera parameters are now shown in the sidebar set (Figure 3.5). The matching error of the theoretical projection of the calibration markers with the measured projection of the calibration markers is calculated. The same procedure is applied for the second camera and then we can save all the parameters from both cameras computed with a DLT method.

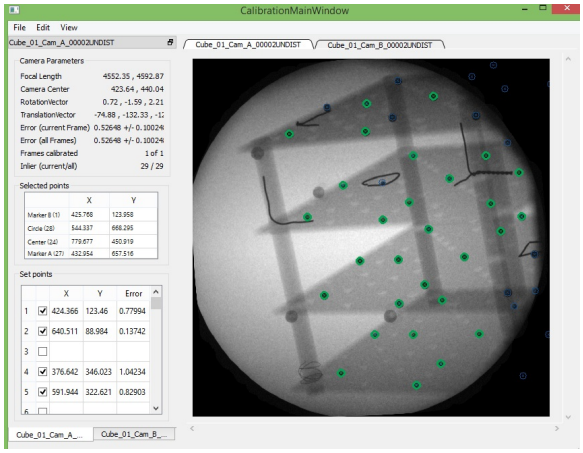

Figure 3.5: All the calibration points are being selected and the camera parameters are shown in the sidebar set

3.5 Validation of system accuracy

In order to validate the system, three methods are used for tracking. Each method quantifies the accuracy of tracking using both idealized and realistic tracking scenarios. Prior to validating methods, all the necessary calibration steps followed by image distortion correction procedures were performed.

3.5.1 Bead Tracking

The two matching custom radiography systems of HSSR were positioned at a relative angle of 60 ^{0}. Emitters allowed capture at 100 frames/sec in a 'low-dose pulsed' radiation mode. The custom calibration cube with 52 enclosed steel beads was used to perform bead tracking. The calibration cube was fixed to a translational and rotational positioning stage (accuracy to 0.025mm and 0.01 degrees respectively) and imaged at seven positions, 4 translations forming a square with 25.4 mm sides, and 3 rotations at 0.00, 5.00, and 10.00 degrees (see Figure 3.6).

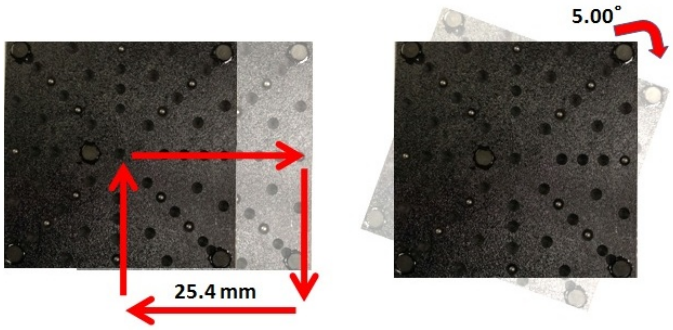

Figure 3.6: Example translation and rotation of the calibration cube for bead tracking

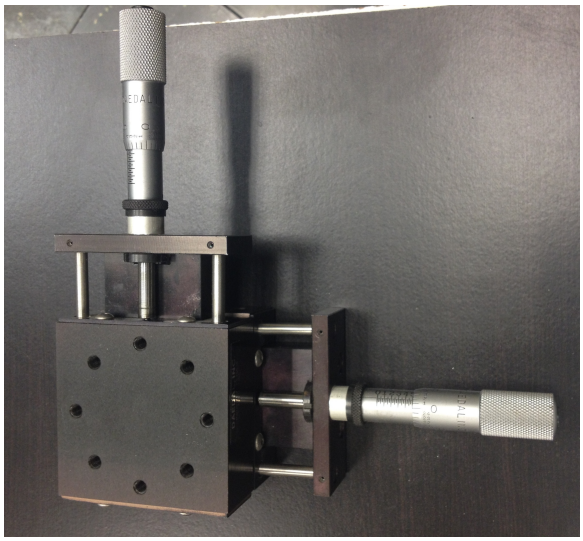

Figure 3.7: Positional stage used for the validation of the HSSR system

The cube was captured in an initial orientation, then translated and rotated, with five radiographs after each step. For bead tracking, custom MATLAB (The MathWorks, Inc., MA) software (XrayProject) was used to identify bead locations in each frame and to calculate the 3D coordinates of the markers. Then the 3D positions of the beads were used to calculate frame by frame motion for each marker set. These beads were easily identified in stereo images as small spheres that have much higher intensity than the background. In order to designate the system's accuracy the same three bead markers were identified and marked on the fluoroscopic images at each position (see Figures 3.8 and 3.9). Using loca-

tions of the beads on each 2D image and the DLT parameters, a 3D reconstruction of the bead centroids can be calculated. Thus bead positions were determined and the cube origin was tracked as a single rigid body.

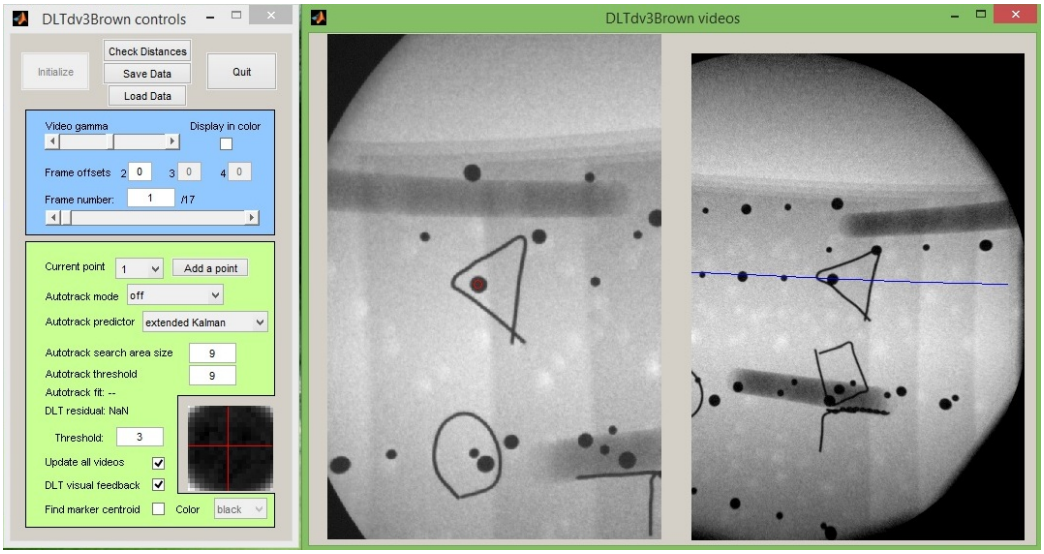

Figure 3.8: Bead Tracking using XrayProject software

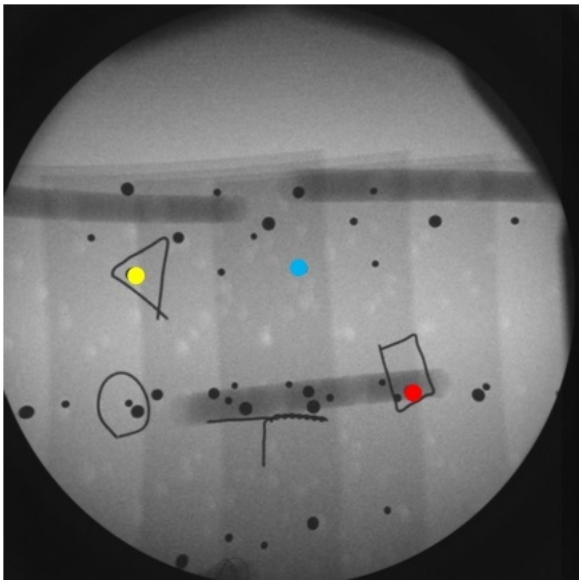

Figure 3.9: Radiograph for bead tracking with example beads for a single plane (yellow,blue,red)

The inter bead distances were compared to the CMM values for each frame. The positions of the cube were averaged over the 5 frames at each position, and the relative 3D translations and rotations between each test were then compared to the absolute measurements from the positional stages, and the average overall errors were calculated. The results for bead tracking revealed an overall mean 3D translational error of 0.2 mm (S.D. 0.1 mm) and a mean 3D rotational error of 0.11 degrees (S.D. 0.03 degrees). Overall average inter bead distance error 1 to 2 was 0.104 mm (S.D. 0.083 mm), 0.106 mm (S.D. 0.050 mm) for beads 1 to 3, and 0.186 (S.D. 0.129 mm) for beads 2 to 3. The overall average error was 0.149 mm (S.D. 0.039 mm) for all beads over the motion. These results prove that HSSR system can track radio-opaque markers with sub-millimeter accuracy.

3.5.2 Implant Tracking

A cobalt-chromium femoral implant (Sigma by DePuy Synthes) and a corresponding CAD model was used in order to perform implant tracking. The femoral implant (Figure 3.10) was fixed via a wooden block to the calibration cube which was fixed to positional stages. The implant was imaged simultaneously with the cube, following translations and rotations identical to that used with beads on calibration cube with five radiographs captured at each position.

Figure 3.10: Femoral implant component

The implant was then tracked using Autoscoper (Brown University, RI) (see Appendix B). The images and the femoral CAD model were imported into this open source shape matching software and Figure 3.11 illustrates stereo radiographs obtained from HSSR and stereo radiographs visualized in Autoscoper for implant tracking. The position and orientation of the 3D bone models of the femoral component was manipulated in 3D space such that the CAD geometries edges were simultaneously matched with the 2D projections of the corresponding silhouette in the fluoroscopic image from each plane.

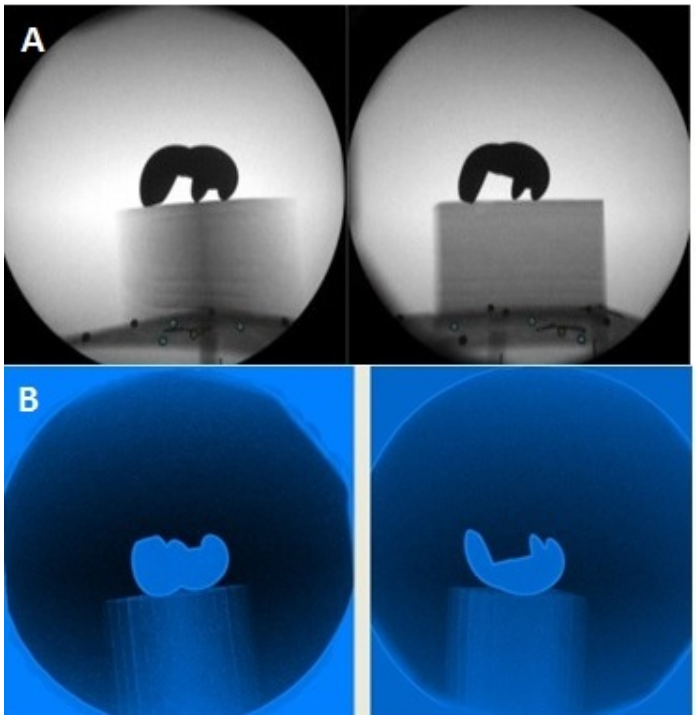

Figure 3.11: A. Stereo radiographs from HSSR system for implant tracking. B. Stereo radiographs visualized in Autoscoper for implant tracking at different time points/positions

After manually positioning the implant component (Figure 3.12) the pose was optimized with a downhill optimization algorithm as a part of the Autoscoper software. The transformation matrices were obtained from Autoscoper and the 3D positions (6DOF) of the implant were averaged over the 5 frames at each position.

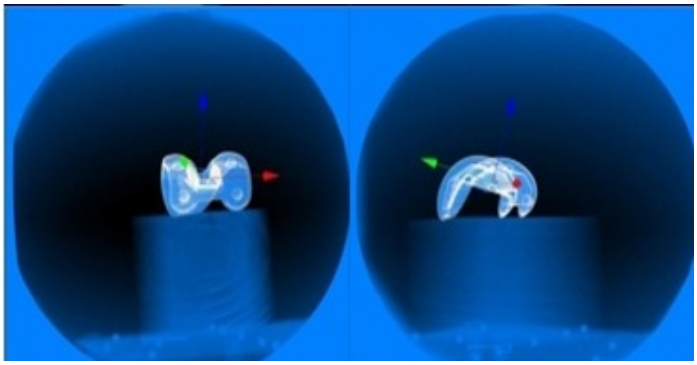

Figure 3.12: CAD model of the femoral component were simultaneously fitted over the 2D projections from each plane. This process was repeated for each position, allowing for 3D positioning to be tracked.

The relative 3D translations and rotations between each test were compared to the precise measurements acquired from the positional stages and translational and rotational errors were calculated. The results showed that the translational error for the implant tracking was 0.9 mm and 0.62 degrees for the rotational error. Based on these results HSSR demonstrates the ability to track implants with sub-millimeter accuracy and thus allows measuring in vivo kinematics for patients with implants with the accuracy required.

3.5.3 Bone Tracking

In order to perform the bone tracking a knee phantom (a full human cadaveric knee joint set in a tissue-surrogate thermoplastic) was used (Figure 3.13). The same method as described for bead and implant tracking is followed for the bone tracking. The knee phantom was fixed on the positional stages, following translational and rotational motions and imaged at 32 positions, 21 translations forming a square pattern with increment of 0.254 mm that traveled in and out of plane with the image intensifiers and 11 rotations with increments of 1^{0} for 5^{0} in both directions. Stereo radiography data were collected for each position at 100 frames per second (Figure 3.14).

Figure 3.13: Knee phantom.

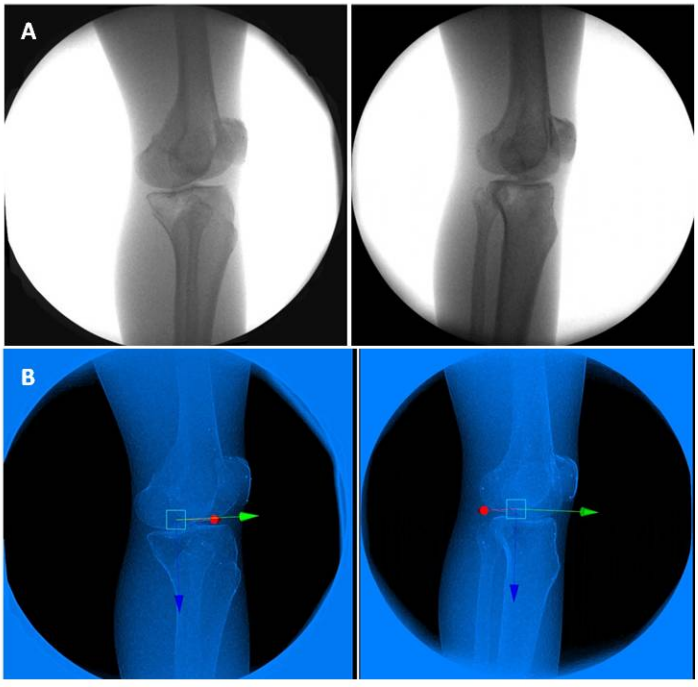

Figure 3.14: A:Stereo radiographs from HSSR for the knee phantom, B:Stereo radiographs when they are imported in Autoscoper

Autoscoper was also used to perform bone tracking. The 3D geometries of the femur, tibia and fibula were extracted from CT bone density data. These 3D geometries, as well as the stereo images of the knee phantom, were then imported in Autoscoper for estimating the 3D position and orientation (pose) of the knee during the translational and rotational motion on the positional stage. After the shape matching is completed (Figure 3.15) The transformation matrices were acquired from Autoscoper and the 3D positions (6DOF) of the knee bones were averaged over the 5 frames at each position. The results showed an overall mean 3D translational error of 0.151 mm (S.D. 0.133 mm) and a mean 3D rotational error of 0.41 degrees (S.D. 0.30 degrees). Table 3.1 summarizes the results for the validation techniques that have been used in order to demonstrate that the HSSR system is capable of tracking beads, implants and bones with sub-millimeter accuracy.

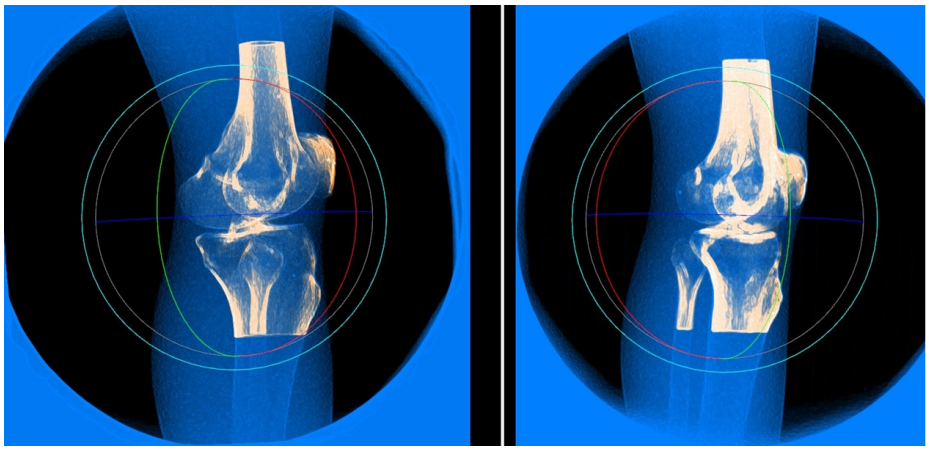

Figure 3.15: Alignment of the 3D model (orange) with the 2D radiographs in Autoscoper

	Translational Error	Rotational Error
Bead Tracking	0.2 mm (0.008") $\pm$ 0.1	$0.11^o \pm 0.03$
Implant Tracking	0.9 mm (0.006") $\pm$ 0.7	$0.62^o \pm 0.59$
Bone Tracking	0.15 mm (0.0063") $\pm$ 0.1	$0.41^o \pm 0.30$

Table 3.1: Average overall error for bead, implant and bone tracking

We see from the results that the bead and bone tracking demonstrated the smallest translational and rotational error with the bead tracking being more accurate in the rotational error. The implant tracking erros were higher although still demonstrating sub-millemeter accuracy. We expect metallic implant edges to be well defined in fluoroscopic images compared to the cortical bone edges. However, it is still challenging due to the opacity of the implants since any internal edges that would help in performing better alignment are not visible. Finally our results are similar with other studies based on model-based tracking methods and using stereo radiography systems. For example in Miranda et al [54] the rotational and translational tracking precision was 0.08 ^{0} and 0.45 mm respectively while in Bey et al [25] the reported results for patellofemoral tracking were 0.877^{0} for rotational accuracy and 0.4 mm for translational accuracy. Finally Massimini et al [35] reported model tracking errors of 0.3 mm and 0.5 degrees.

Chapter 4

Literature Review- Precise Healthy Knee Kinematics measurements

Quantification of knee motion is essential for assessment of joint function for diagnosis of pathology, such as tracking and progression of osteoarthritis and evaluation of outcome following conservative or surgical treatment. Numerous techniques have been developed to study the in vivo human joint motion. Joint motion is driven by a combination of dynamic physical forces (gravitational, inertial and contact), active muscular forces and constraints imposed by passive structures [56]. For a complete biomechanical analysis of the human knee joint, precise measurement systems become highly important. Knee is one of the largest and one of the most biomechanically complex joints in the body and the knee's primary motions are flexion-extension. In addition, anterior-posterior displacements as well as rotation play an important role to its overall function [7]. Figure 4.1 demonstrates the 6 DOFs of the knee, three translations and three rotations.

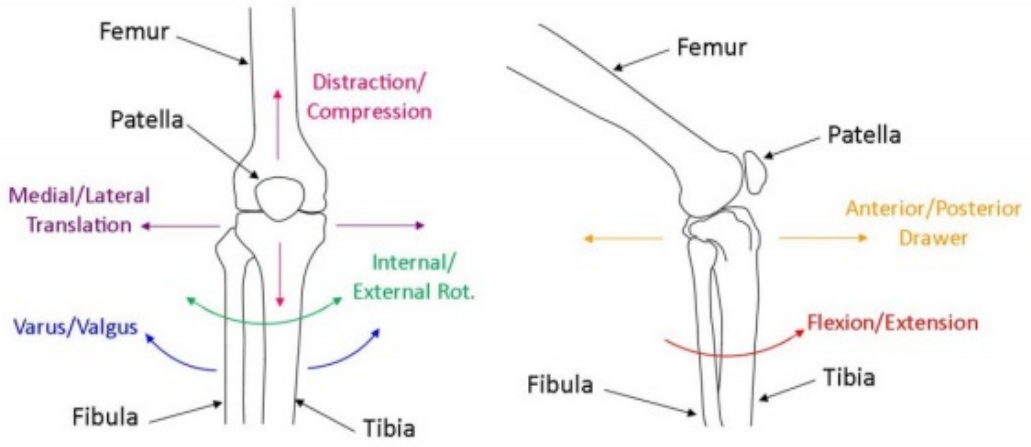

Figure 4.1: The 6 DOFs of the knee

Passive motion of the knee joint is dependent on the interaction between the shape of the articular surfaces and the various ligaments crossing the knee joint (Figure 4.2). Standard coordinate systems for the knee are based on mechanical or anatomical axes. Grood and Suntay, in 1983, presented a joint coordinate system providing a geometric description of the three-dimensional rotational and transnational motion between two rigid bodies, applied to the knee joint [43]. With this method, the described joint displacements became independent of the order in which the components' translations and rotations occur. Investigation of the characteristic knee motion is important for the evaluation and design of contemporary Total Knee Arthroplasty (TKA) that aims to restore normal knee function and achieve full range of knee flexion. Flexion of the human knee occurs along the six degrees of freedom in space and includes rotation along the horizontal axis (flexion), translation along the saggital axis (roll-back of femur) and rotation over the coronal axis (femoral external rotation). Knee flexion progresses as a combination of rolling, gliding, and rotation of the femoral condyles over the tibial plateaus. It has been shown that the kinematics of artificial knees are different than in normal knees, and involve excessive

sliding and rotational motions which may lead to high shear stresses at the joint interface. Motion analysis of normal knees provides references for the analysis of pathological knees, as in cases of osteoarthritis or ligament injury or in the design of total knee prostheses. In Chapter 5, HSSR will be utilized for classifying knee joint kinematics in healthy older adults performing common movements of daily living.

This chapter presents different results of various studies that answer the knee kinematics question. The studies that are presented here are based on precise measurement systems for measuring healthy knee kinematics in vivo based on intra-cortical traction pins, fast-PC MRI, single plane fluoroscopy and dual plane fluoroscopy.

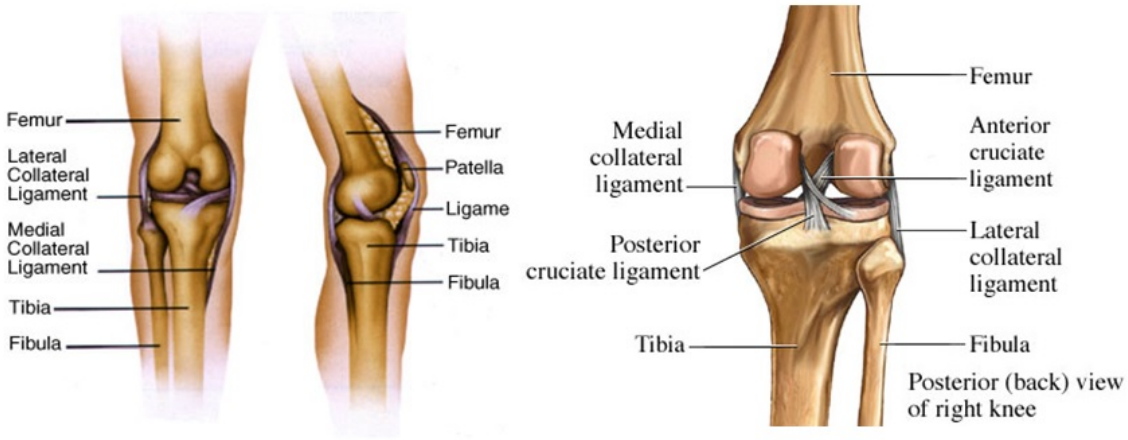

Figure 4.2: Anterior, Medial and Posterior view of the right knee anatomy [1]

Intra-Cortical Pins

Although implantation of traction pins into the bone of human subjects can provide very accurate knee kinematic data due to its highly invasive nature there is a limited population that can be studied using implantation. Paper [1] focuses on measuring 3D kinematics of the tibiofemoral joint during normal walking by fixing target markers to the tibia and femur with the method of intra-cortical traction pins. In order to estimate the position of the target markers relative to internal anatomical structures, radiographs of the lower limb were

captured (Figure 4.3). Five healthy subjects with no history of pathology in their lower limb have participated in this study. The goal of this research was to give an accurate description of the relative angular and linear movements between the tibia and femur during walking. The target markers were attached to intra-cortical pins and then fixed directly into the bones. Photogrammetry was used for providing 3D reconstruction. For measuring 3D coordinates of the target markers in those five healthy subjects during walking, high-speed cine cameras were utilized. The relative motion between the two bones was determined based on a joint coordinate system. For qualifying the motion between the tibia and femur six reference frames were specified. The global and radiographic reference frame, the tibial and femoral anatomical reference frame and the tibial and femoral marker reference frame. The origin and axes of the global and radiographic reference frames were determined, respectively, by the cube that was used to calibrate the 3D volume through which the subjects walked and by the smaller cube which was utilized for the radiographs. After the identification of the bony landmarks on the radiographs, the locations of the origins of the anatomical reference frames as well as the orientations of their axes with respect to the individual bones, were defined. Average kinematic patterns of the tibiofemoral joint were acquired from two trials for each of the five subjects. Results from this research demonstrated that angular motions other than flexion-extension are of relative small amplitudes (5^0 for abduction/adduction and 10^0 for internal/external rotation) as are the translations of the tibia. Also the present findings showed that the tibia rotated internally with respect to the femur as the tibiofemoral joint approached full extension and that puts into question the accepted view that the tibia rotates externally relative to the femur in the late stages of the extension. Generally, findings of this study showed the extent of the significant angular and linear motions that occur about and along each axis of the joint coordinate system that was used to characterize the relative motion between the tibia and femur.

Figure 4.3: View from one of the camera positions as the subject walked with the target triads attached to the femoral and tibial pins [1]

MRI

Magnetic resonance imaging (MRI) is a non-invasive technique has the capacity to depict soft tissues and bony structures and has proven to be an excellent source for dynamic knee joint imaging. The authors in [2] focus on measuring in vivo normative 3D patellofemoral (PF) and tibiofemoral (TF) kinematics during dynamic motion (Figure 4.4). The goals of this investigation were, i). to evaluate whether the knee joint kinematics vary based on gender; ii). and to look into the correlation between the 3D kinematics of patellofemoral and tibiofemoral joints. For fulfilling those goals, a large normative database of six degree of freedom tibiofemoral and patellofemoral combination, obtained in a non invasive way during voluntary knee flexion-extension using fast-PC (dynamic) magnetic resonance imaging (MRI), was established. Twenty-five healthy subjects (14 female, 11

male) with an age average of 26.7±8.8 years participated in this study. In some of the subjects both knees were imaged so data for 34 knees in total were acquired. Dynamic MRI sequences obtained the data from which the 3D kinematics were established. A dynamic exam included three dynamic trials where the subjects were asked to during dynamic imaging to extend and flex their knee form maximum flexion to full extension and back. From all three trials the required anatomic information was obtained and selected from the fast-PC anatomic image representing full extension. 3D rigid body rotations and translations of the femur, tibia and patella were measured through integration of the fast-PC velocity data. The kinematics measured here were based on an anatomical coordinate system which was identified in a single time frame only. The interdependence of six translations and six rotations specifying the PF and TF kinematics was evaluated using a Pearson's linear correlation. In order to generate population averages and to observe differences between groups, each kinematic variable was interpolated to single degree knee angle increments. The results demonstrated that few correlations exist between TF and PF joint kinematics. It was found that only 28 % of the alterability in PF lateral-medial tilt and only 12 % of the alterability in PF interior-superior translation could be explained by internal-external rotation and the knee appears not to have coupled rotations at any joint. Furthermore the results showed that there are no significant differences based on gender. Finally, fast-PC MRI was found to be able to track the combined 3D PF and TF kinematics along with the knee musculature; thus, the entire knee joint can be studied at once.

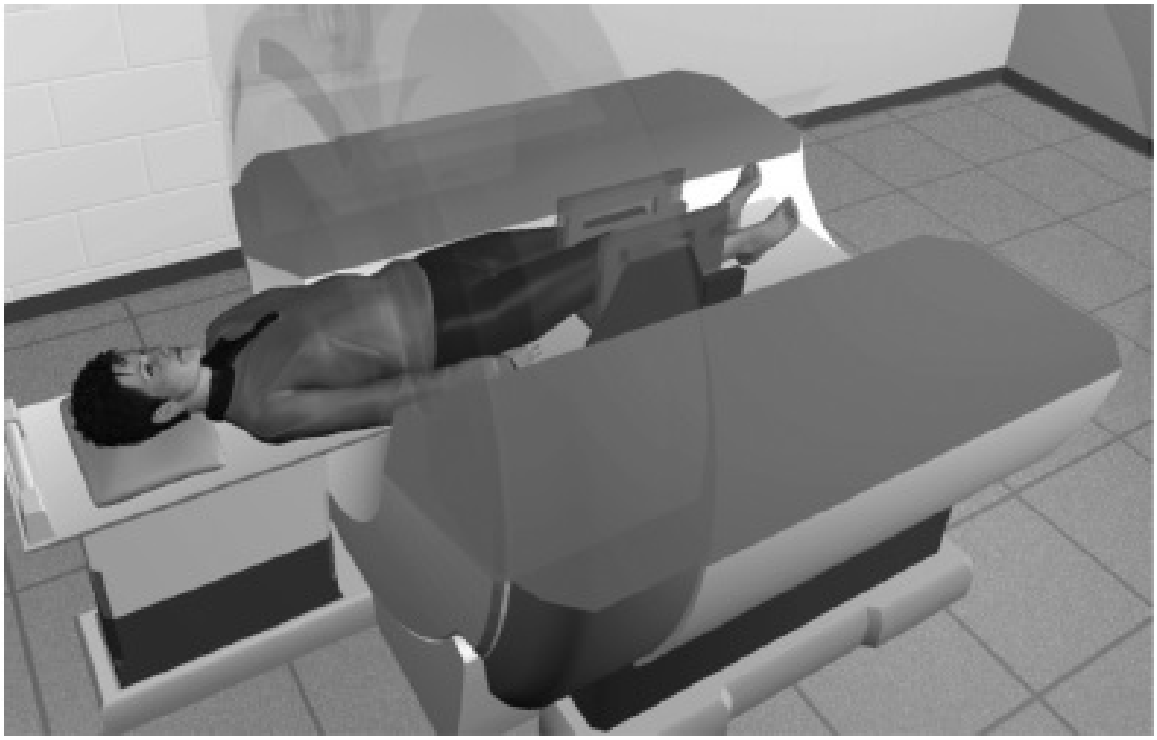

Figure 4.4: Subject position within the MRI imager [2]

Single Plane Fluoroscopy Systems

Single-plane fluoroscopy has been used extensively in order to measure natural knee motion. In [3] in vivo 3D knee motion and surface kinematics during active knee extension under loaded and unloaded conditions were measured by using single plane fluoroscopy with CT bone models (Figure 4.5). Measurement of the changes of the 3-D motion and surface kinematics of the knee under different external loading conditions is important for understanding and evaluating the function of the joint. Specifically in this study, the Knee Extension Exercise (KEE) has been investigated. KEE has been applied extensively in the rehabilitation programs of patients with various knee disorders. The 3D kinematics were measured for eight normal subjects during active knee extension for unloaded and loaded conditions by using a voxel-based method for the registration of single-plane fluoroscopic images with CT bone data. Each subject sat on a chair and performed isolated active

knee extension tests in loaded and unloaded conditions under single-plane fluoroscopic surveillance at a sampling frame rate of 30 frames/sec. The effects of muscle activity in response to external loads on the knee kinematics during movement have not been studied extensively. The main reason for that is that these conditions are difficult to simulate in vitro and the accurate measurement of the in vivo 3-D joint kinematics during dynamic movements is not straightforward [57, 58]. Methods based on the registration of two-dimensional fluoroscopic images and computer models of the components of total knee replacements have been developed for accurate 3-D kinematic analysis of replaced knee joints [19, 21]. However, the application of this method to natural knee kinematics has been limited [59, 12] because human bones have weaker contrast and it becomes more difficult to identify them in fluoroscopic images in comparison to metallic replacement components which leads to reduced accuracy. A voxel-based 2-D to 3-D registration method for more accurate measurement of the natural knee kinematics can be a useful tool for the study of the in vivo 3-D knee motion and surface kinematics during KEE [60]. Results from this study showed that the knee kinematics during unloaded conditions was found to be similar to previous findings. A weight at the ankle did not affect the joint angles but significantly alter the lateral contact positions during knee extension and also reduced the asymmetry of the surface kinematics between the medial and lateral condyles. The voxel-based method used in the current study for the registration of the fluoroscopic images with CT bone model was shown to be highly accurate.

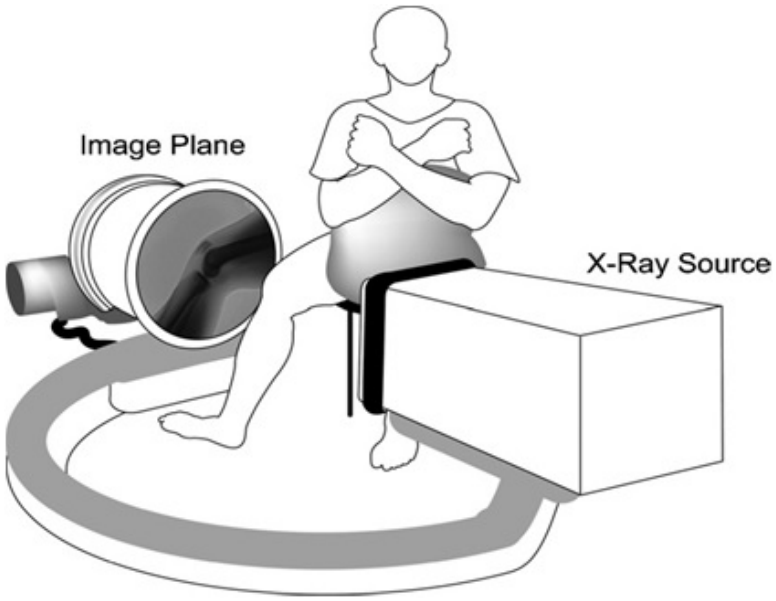

Figure 4.5: Schematic diagram showing a subject performing active knee extension under dynamic single fluoroscopic surveillance [3]

Another fluoroscopic analysis of the normal human knee is presented in study [12]. The purpose of this investigation was to use single-plane fluoroscopy and computed tomography (CT) for determining with high accuracy the 3D,in vivo, weight-bearing kinematics of five normal knees. Three-dimensional computer aided design models (CAD) of each subject's femur and tibia were recreated from the 3-D CT bone density data. Five healthy subjects subsequently did four weight-bearing activities (deep knee bend, normal gait, rising from a chair, stair descent) and these activities have been captured by single plane fluoroscopic images. The results showed that during all five activities the lateral condyle experienced significantly more anterior-posterior translation, leading to axial rotation of the tibia relative to the femur. This research offers an accurate 3-D, in vivo kinematic analysis of the normal knee under weight-bearing conditions, while the subjects did multiple different activities. The presented data may provide useful information for future knee simulation studies and a better baseline of kinematic data for future total knee arthroplasty design.

Single plane fluoroscopy was used to accurately determine the 3-D, in vivo, weight bearing kinematics throughout the entire range of knee flexion of ten normal and five Anterior Cruciate Ligament deficient (ACLD) knees by Douglas et al. [59]. Weight-bearing kinematics of ten normal and five ACLD knees were investigated. Each subject performed subsequently a weight-bearing deep knee bend activity while under fluoroscopic surveillance. During the deep knee bend activity, subjects were asked to begin in full extension and flex the knee of interest to maximum flexion. The fluoroscope maximum frame rate was 30 frames/sec. Image distortion and non-uniform scaling can be compensated for by careful calibration [21]. An advantage of the present experimental model is that it allows analysis under in vivo weight-bearing conditions throughout the entire range of knee flexion. All ten normal knees experienced posterior femoral translation of their lateral condyle and minimal change in the position of the medial condyle. ACLD knee experienced posterior femoral translation of their lateral condyle with increased translation of the medial condyle when compared to normal knee. Normal and ACLD knee subjects demonstrated similar patterns of posterior femoral translation during progressive knee flexion but they exhibited different axial rotation patterns after 30 degrees of knee flexion. All ACLD subjects were evaluated relatively soon ($<$ 6 months) after their ACL injury. Differences in kinematic patterns between normal and ACLD subjects may increase in chronic ACLD subjects due to attenuation of secondary soft tissue stabilizing structures over time. The current study determined that accurate 3-D motion of normal and ACLD knees, under in vivo weight-bearing conditions, can be defined by using single-plane fluoroscopy and a 3-D to 2-D image registration process.

Single plane fluoroscopy systems has proven to be accurate in establishing knee position along the axis parallel to the image plane. However, establishing the knee motion in the direction perpendicular to the image plane has proven to be not accurate enough and biplane fluoroscopy systems are being used instead to overcome this limitation [12, 16, 15].

Dual Plane Fluoroscopy Systems

Biplane fluoroscopy systems enable the accurate measurement of 6 degrees of freedom kinematics of the knee joint during dynamic activities. In Myers et al [26] a study was undertaken to measure, describe and compare tibiofemoral rotations and translations of soft and stiff landings in healthy individuals by using biplane fluoroscopy. Although anterior cruciate ligament (ACL) injury prevention programs have been denoted to be efficient at teaching athletes to avoid stiff landings, the overall occurrence of non contact ACL injury and surgical reconstructions remains high in both men and women. The in vivo 3-D lower extremity knee kinematics of three men and ten women were collected as they performed the landing from a 40-cm height. All subjects were instructed to perform soft and stiff landings. Stiff landings produced significantly greater ground reaction forces (GRFs) and knee extension moments but did not cause increased amounts of anterior tibial translation or knee rotation in either varus / valgus or internal / external rotation when compared with soft landings in healthy individuals under these testing conditions. The results showed the ability of the musculature and soft tissues around the knee joint to keep translations and rotations of the knee within a small, safe range during controlled tasks of differing demand. Also, the same group of Biomechanics research laboratory in Vail used biplane fluoroscopy to measure describe and compare tibiofemoral rotations and translations of healthy individuals measured in vivo during four functional tasks of increasing demand on the quadriceps commonly included in rehabilitation protocols [61]. The ACL has been well defined as the main passive restraint to anterior tibial translation (ATT) in the knee and plays an important role in rotational stability. The kinematics of the knee during different functional tasks is affected by joint position, external forces as well as the balance of active and passive contributory forces across the knee. The in vivo 3-D kinematics of ten adult female patients, with no history of injuries in lower limbs, was measured using biplane fluoroscopy while

the patients completed four tasks that commonly appear in different stages of ACL rehabilitation programs and produce increasing demands. The tasks included an unloaded knee extension from a seated position, walking at a constant pace of 90 steps per minute, a maximum knee isometric extension with the knee in 70 degrees of flexion and a landing from a height of 40 cm. Results demonstrated that ATT significantly increased as the demand on the quadriceps increased. On the other hand, internal rotation was not significantly different between landing, isometric contraction and unweighted knee extension. The knee is able to effectively constrain ATT and internal rotation, this indicates that the healthy knee has a safe envelope of function that is tightly controlled even though task demand is elevated.

A high Knee Valgus (KVA) has been successfully used as a predictor for ACL injury in female athletes [62]. Thus, an accurate assessment of 3-D knee motion and the valgus knee motion particularly would be essential to fully understand the biomechanical mechanisms of knee injury, repair and rehabilitation.

Torry et al [4] uses high speed biplane fluoroscopic imaging techniques (Figure 4.6) to accurately measure and describe the 3-D rotations and translations of the healthy knee during the stiff drop-landing motion . The relationships between knee flexion-extension, varus-valgus and internal-external rotations and between Anterior tibial translation (ATT) and lateral tibial translation (LTT) were determined in order to understand better the coupling of these kinematics during the drop landing. Six male athletes, with no history of lower extremity injury, were instructed to execute a double-legged, drop-landing maneuver by stepping off a $40cm$ high platform onto a force plate. Stiff landings were selected because they may give more interesting results with greater applications to ACL injury than do soft landings. For each landing, biplane fluoroscopy data were collected for 1.0 s at 500 frames per second with a shutter speed of 1/2000 of a second. Image distortion was corrected by imaging an accurately machined aluminum plate with 406 holes in a squared 15mm pattern, directly placed in front of the image intensifier. The focus position of each

fluoroscopy system and the 3-D relationship between them were calculated after imaging a $15cm^3$ calibration cube enclosing 15 tantalum markers position. Kinematic accuracies for tracking tantalum beads and bones using this biplane fluoroscopy system were determined. The results from this study associate increased knee translations with commonly measured performance variables such as knee valgus and internal rotation angles that are predictive of the noncontact ACL injury, in particular the data support the coupling of KVA with knee ATT and lateral translation during drop landings.

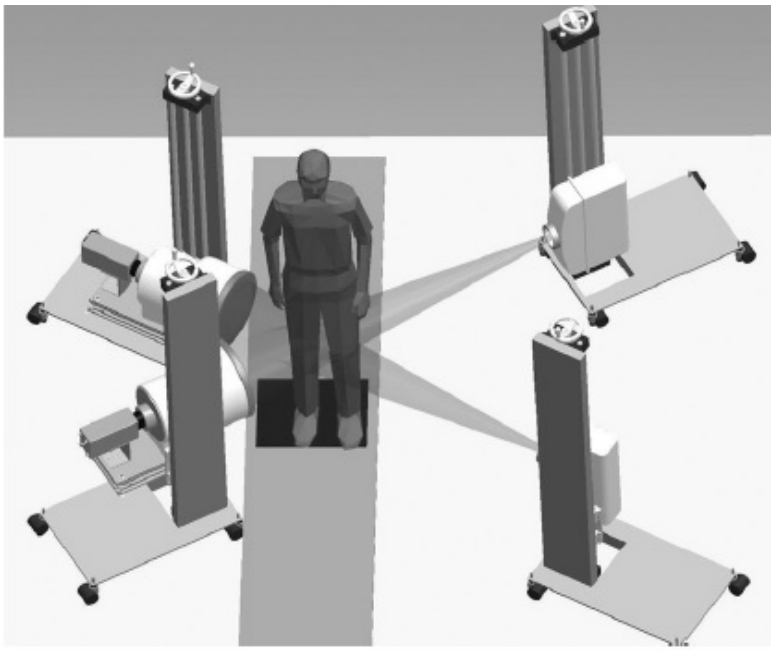

Figure 4.6: Computer rendering of the configuration of the biplane fluoroscopy system [4]

The dual plane fluoroscopic imaging method was used to measure the six-degree of freedom kinematics and condylar motion of the knee during the stance phase of treadmill gait at a speed of 0.67 m/sec. For the purpose of this investigation eight healthy subjects, six males and two females, were recruited in Kozanek et al [63]. The hypothesis was that the 6 DOF knee kinematics estimated during gait will not be similar with those reported for non-weightbearing activities, specifically regarding the phenomenon of the femoral roll-

back and also that during the stance phase of gait the motion of the medial femoral condyle in the transverse plane is bigger than the motion of the lateral femoral condyle. For creating the 3D models a 3-Tesla scanner and a double echo excitation sequence have been used. Then, the dual fluoroscopic imaging system (DFIS) was used to establish knee kinematics during the stance phase of gait. A modeling software was used after, to align the 3D MR-based knee model with the 2D fluoroscopic images. The kinematics were estimated utilizing a joint coordinate system based on transepicondylar axis of the femur. The 6 DOF kinematics of the knee were averaged among all eight subjects during the stance phase of gait. Th relation between the flexion-extension motion of the knee and motion in the other DOF was established using a square of Pearson product moment correlation coefficient (r^2). For comparing the range of motion of the medial and lateral condyles in the transverse plane, the Student t-test was used. Findings from this study confirmed both hypotheses. The patterns of motion were different from those referenced in non weight-bearing activities. The knee demonstrated consistent patterns in all rotations and translations. Internal-external and varus-valgus rotation, as well as anterior-posterior translation indicated clear correlation with the pattern of flexion-extension. Furthermore, the medial femoral condyle excursions were bigger than those of the lateral femoral condyle. In addition, regarding the phenomenon of femoral rollback, the femur was observed to move posteriorly with extension and anteriorly with flexion. Finally, these results establish that knee kinematics is activity dependent and motion patterns of one activity can not be generalized to explicate a different one.

In Li et al [64] a treadmill was integrated into a dual fluoroscopic imaging system (DFIS) in order to formulate a gait analysis system. For showing the application of this system one healthy subject performed gait on the treadmill at different speeds :1.5, 2.0, 2.5 and 3.0 mile/hour MPH. The knee joint was captured from heel strike to toe-off during three consecutive strides with DFIS. The 3D bone model of the knee was reconstructed by

tracing the bony contours on saggital plane magnetic resonance (MR) images of the knee in solid modeling software. The alignment of the model and the 2D fluoroscopic images was performed using a visual DFIS environment where the in vivo positions of the knee were reproduced by matching projections of the models to their outlines on the 2D images. The results showed that the duration of the stance phase decreased with the treadmill speed. With increasing speed, the amplitude of the knee flexion during stance phase increases. Knee kinematics demonstrated similar patterns for the rotations and translation under different treadmill speeds.

Precise knowledge of the dynamic knee motion in vivo is essential for comprehending normal and pathological functions of the knee joint. Although, intra-cortical traction pins method gives results with high accuracy, it is limited due to its highly invasive nature. Fast-PC MRI imaging is one of the promising techniques in precise measurement of knee kinematics but it can not capture the full range of motion during dynamic activities like walking. Single plane fluoroscopy can provide accurate results during dynamic activities in the in plane motion; however, it is imprecise in the out of plane motion. Finally all the above limitations can be overcome with the dual plane fluoroscopy that is capable of measuring knee kinematics with sub-millimeter accuracy during a wide range of activities of daily living. Table 4.1 summarizes the studies presented here that have used precise techniques for assessment of healthy knee kinematics and these data can provide a baseline knowledge for the analysis of pathological knees.

<table>
<tr><th>Methods</th><th>Subject's Age (yr.)</th><th>Activities</th><th colspan="4">Accuracy</th></tr>
<tr><td>Intra-Cortical Traction Pins
(Lafortune et al. 1992)</td><td>27.2
(5M)</td><td>Gait
(TF)</td><td colspan="2">Abduction/Adduction
5^o</td><td colspan="2">IE
10^o</td></tr>
<tr><td>MRI (A.R Seisler
and F.T Sheehan et al.
2007)</td><td>27±9
(14F + 11M)</td><td>Extension -
Flexion
(TF)</td><td colspan="4">Average Difference
0.2^o - 2.5^o
1.3 - 1.9 mm</td></tr>
<tr><td rowspan="4">Single-Plane Fluor.
(T.W Lu et al.
2008)</td><td rowspan="4">20.7± 0.9
(8 F/M)</td><td rowspan="4">Knee extension for loaded and
unloaded conditions</td><td colspan="4">Mean ± Std for Medial and Lateral Contact points</td></tr>
<tr><td colspan="2">AP (mm)</td><td colspan="2">ML (mm)</td></tr>
<tr><td>Unload</td><td>Load</td><td>Unload</td><td>Load</td></tr>
<tr><td>MLC 11.2 ± 4.0</td><td>11.5 ± 3.9</td><td>5.0 ± 3.4</td><td>5.8 ± 2.4</td></tr>
<tr><td>LCP 16.5 ± 2.1</td><td>12.5 ± 3.3</td><td>6.6 ± 1.8</td><td>4.9 ± 1.2</td></tr>
<tr><td rowspan="7">Single Plane Fluor.
(R.D Komistek et al.
2003)</td><td rowspan="7">37.2
(4 F/M)</td><td rowspan="7">i). Deep Knee Bend
(DKB)
ii). Chair Sit
iii). Chair Rise
iv). Gait
v). Stair Descent
(FT)</td><td colspan="3">Average AP
(mm)</td><td>Average Axial
Rotation (^{o})</td></tr>
<tr><td></td><td>MC</td><td>LC</td><td></td></tr>
<tr><td>DKB</td><td>-1.5</td><td>-14.1</td><td>16.8</td></tr>
<tr><td>Chair Sit</td><td>-2.9</td><td>-12.8</td><td>13.1</td></tr>
<tr><td>Chair Rise</td><td>2.2</td><td>16.9</td><td>19.4</td></tr>
<tr><td>Gait</td><td>-0.9</td><td>-4.3</td><td>4.4</td></tr>
<tr><td>Stair Descent</td><td>2.0</td><td>-3.9</td><td>7.8</td></tr>
<tr><td rowspan="2">Single - Plane Fluor.
(D.A Dennis et al.
2005)</td><td rowspan="2">37
(10 F/M)</td><td rowspan="2">Deep Knee Bend
(FT)</td><td colspan="2">Average AP
(mm)</td><td colspan="2">Average Axial Rotation
(^{o})</td></tr>
<tr><td>MC:
1.94±1.86</td><td>LC:
21.07±9.30</td><td colspan="2">23.67±6.09</td></tr>
</table>

Biplane Fluor. (C.A Myers et al. 2011)	6M - 29.7± 7.9 10F - 26.7± 6.7	Soft and Stiff Landings (TF)	Soft Landing		Stiff Landing	
			AP (mm)			
			Aver: 2.8±12 Max: 4.7±1.6		Aver: 3.0±1.4 Max: 4.4±0.8	
			IE (^{o})			
			Aver: 3.7±5.1 Max: 5.6±5.5		Aver: 2.7±4.3 Max: 4.9±4.7	
			VV (^{o})			
			Aver: 0.2±1.2 Max: 1.7±1.2		Aver: 0.2±1.8 Max: 1.6±0.9	
Biplane Fluor. (C.A Myers et al. 2012)	29.7± 7.9 (10F)	i) Unloaded Knee Extensions(KE); ii) Walk; iii) Maximum Isometric Knee Extension (IKE); iv) Landing (TF)		Peak ATT (mm)	Peak IE (^{o})	
			Walk	3.1±2.2	3.9±4.2	
			Landing	5.6±1.9	19.4±5.7	
			KE	2.6±2.1	14.5±7.7	
			IKE	5.0±1.9	15.9±6.7	
Biplane Fluor. (M.R Torry et al. 2011)	34.1± 7.9 (6M)	Stiff Drop Landing (TF)		Peak ATT (mm)	Peak LTT (mm)	
			Mean	4.3±0.7	1.5±1.4	
			Excursion	2.1±0.9	2.6±1.6	
Dual plane Fluor. (M. Kozanek et al. 2009)	32-49 (6M/2F)	Gait (FT)	Average AP Excursion		Medial Femoral Condyle	Lateral Femoral Condyle
			5 mm		17.4±2mm	7.4±6.1mm
Dual plane Fluor. (G. Li et al. 2009)	45(1M)	Gait (TF)	AP Range (mm)			
			5 (midstance)to -2.5 (toe off)			

Table 4.1: Summary of the studies presented here that have used precise techniques for assessment of healthy knee kinematics. M: Male, F:Female, TF:Tibiofemoral, FT:Femorotibial, IE:Internal-External, AP:Anterior-Posterior, ML:Mediolateral, MC:Medial COndyle, LC: Lateral Condyle, ATT:Anterior tibial translation, LTT:Lateral tibial translation

Chapter 5

Application to Normal Knee

5.1 Introduction

Quantification of knee motion is essential for assessment of joint function for diagnosis of pathology, such as tracking and progression of osteoarthritis and evaluation of outcome following conservative or surgical treatment. Osteoarthritis (OA), appears in the knee more than any other joint and disease development and progression are influenced by abnormal joint kinematics under dynamic weight bearing conditions. Total knee arthroplasty (TKA) is an invasive treatment for arthritic pain and functional disability and it is used for deformed joint replacement with implants in order to restore joint alignment. Additionally, precise measurements of knee kinematics provide input to computational models used to predict joint function. It is important to describe knee kinematics in healthy individuals for comparison in diagnosis of pathology and understanding treatment to restore normal function. Thus, the quality of biomechanical models, the accuracy of treatment evaluation and diagnosis and the design of implants, are all contingent on the quality of the experimental methods used in their creation. However, measuring the in vivo dynamic knee biomechanics in six degrees of freedom (position and orientation) with an accuracy that is acceptable

has been proven to be technically challenging. Traditional marker-based motion capture has been extensively used for assessing dynamic knee motion but these methods include errors due to skin and soft tissue motion [11]. For overcoming the inherent inaccuracy of skin mounted markers, intra-cortical pins methods have been used instead [1] that provide some of the best quantitative data during dynamic motion. However, due to its highly invasive nature its application is limited for human studies. Medical imaging such as magnetic resonance imaging (MRI) and computed tomography (CT) allow assessing movement of the underlying bone directly but limit the analysis to quasi-static conditions, thus, these methods have inadequate dynamic measurement capabilities for capturing the knee joint during higher demand activities of daily living. Recently, fluoroscopic imaging techniques have been used for the analysis of knee joint motion during dynamic activities. Single plane fluoroscopy have proven to be precise method for establishing knee position along the axis parallel to the image plane with sub-mm accuracy. However, its accuracy in establishing the knee motion in the direction perpendicular to the image plane has proven to be imprecise [12, 16]. Dual plane fluoroscopy systems provide accurate three-dimensional quantification of six DOF knee kinematics. Researchers have used dual plane fluroscopy systems to evaluate normal knee kinematics during a baseline knee extension and during dynamic activities such as normal gait [63, 64], landing [4, 26] and step-up activity [65]. However, most descriptions of knee kinematics have been for younger adults and for a limited span of activities. Furthermore, joint pathology occurs more frequently in older adults and movement patterns change as we age [13, 66, 67]. As stated in [68] the ability of older people to perform activities of daily living decline with age and this may be caused because during activities like walking, ascending or descending stairs, it requires a substantially greater effort in older people compared with younger people relative to their available maximal capacity. Studies have shown that older subjects tend to slow down their pace and do shorter strides while walking when compared to younger people [69] and

they adopt a different way of walking in order to increase stability and for fall prevention. Furthermore, the high prevalence of knee pain, osteoarthritis, TKA in subjects over the age of 55 requires a baseline description of healthy knee function during demanding activities of daily living. To our knowledge, no others have assessed normal knee function for a cohort age-matched to TKA recipients and during activities that patients with TKA often report to be troublesome, namely descending a step and executing a turn during walking. Our purpose was to classify joint kinematics in healthy older adults performing common movements of daily living like straight walking and during higher demand activities in order to establish a useful baseline for the envelope of healthy knee motion for subsequent comparison with patients with TKA. We have used a high speed stereo radiography system (HSSR) with high frame rates and two view planes for three-dimensional tracking of bones and implants with sub-millimeter accuracy. We hypothesized that the amount of motion in DOFs that are primarily constrained by soft tissue (internal-external (IE) rotation and anterior-posterior (AP) translation) would be more activity dependent as compared with DOFs partially constrained by articular geometry (varus-valgus (VV) rotation). Also, we hypothesized that higher demand activities would elicit greater IE and AP than normal gait.

5.2 Methods and Materials

Subjects

This study had an Institutional Review Board approval and all participants signed an informed consent. The doses caused from HSSR were calculated using industry standard software (PCXMC STUK - Radiation and Nuclear Safety Authority, Helsinki, Finland)(Appendix A). The volunteers had no history of injuries or surgeries to the lower limbs. The in vivo three-dimensional knee kinematics of 6 healthy subjects (means $\pm$

standard deviations : age=61.67 $\pm$ 5.37 years, body mass= 74.6 $\pm$ 7.72 kg, body mass index [BMI]= 26.7 $\pm$ 4.4 kg/m^2, height = 168.2 $\pm$ 13.7 cm, see also Table 5.1) were measured using the HSSR system while the subjects completed four tasks. The subjects were instructed to perform an unloaded knee extension in which the individuals were in seated position and asked to slowly extend their knee from high flexion to full extension; to walk at a self selected pace over approximately 9 meters(Figure 5.1); to step down from a 7 inch platform; and walk into the imaging volume and perform a 90^0 direction change with the planted foot of the imaged knee (pivoting).

Subjects	Gender	Height (cm)	Weight (kg)	Age	BMI
KS02	Female	163	65.8	56	24.8
KS03	Male	174	74.8	61	24.7
KS04	Female	143.5	72.6	57	35.5
KS06	Male	181.61	88.9	70	27
KS07	Male	177.2	74.4	60	23.7
KS08	Male	170.18	71.1	66	24.6

Table 5.1: Subjects Specifications

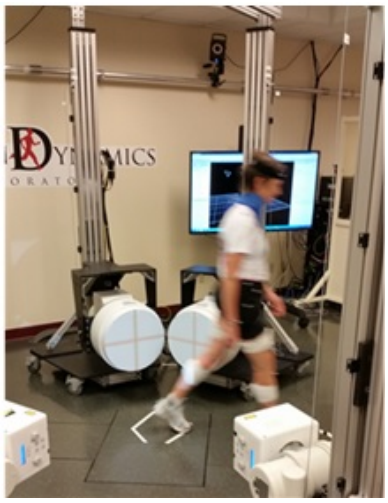

Figure 5.1: Healthy knee subject during normal gait

HSSR description

HSSR system is composed of two matching custom radiography systems with 40 cm (16") diameter image intensifiers (Thales Inc., TH 9447 QX). High-speed image acquisition was achieved through integration of high-speed, high-definition (1080x1080) digital cameras (Miro M-120, Vision Research Inc.,12 bit) onto the image intensifiers. Emitters, powered by 480 V generators, along with the high speed high definition cameras, enable capture at 100 frames/sec in a 'low-dose pulsed' mode.

HSSR validation and calibration

The use of the HSSR system to investigate the relative position and orientation of three-dimensional bones was validated by using a bead tracking and a bone tracking method. Stereo radiographic images were collected with the two image planes of the HSSR positioned at a relative angle of 60 ^{0}. For the bead tracking a custom calibration cube with 52 enclosed steel beads was used and was fixed to a translation and rotational positioning stage (accuracy to 0.025mm and 0.01 degrees respectively) and imaged at seven positions, 4 translations forming a square with 25.4 mm sides, and 3 rotations at 0.00, 5.00, and 10.00 degrees. For bead tracking, custom MATLAB (The MathWorks, Inc., MA) software (XrayProject) was used to identify bead locations in each frame and to calculate the 3D coordinates of the markers by using standard DLT techniques. The average translational error was 0.2 $\pm$ 0.1 mm and the rotational error was 0.11 $^0\pm$ 0.03^0. These results are comparable with other stereo radiography and tracking methods such as in Tashman et al reported tracking bead precision of 0.064 mm and 0.31^0 [41]. For the bone tracking a human knee phantom was fixed to a translational and rotational positioning stage (accuracy to 0.025mm and 0.01 degrees respectively) and imaged at 32 positions, 21 translations forming a square pattern with increment of 0.254 mm that traveled in and out of plane with

the image intensifiers and 11 rotations with increments of 1^{0} for 5^{0} in both directions. The bone tracking was performed using Autoscoper a program developed at Brown University (Brown University, RI). The accurate 3D geometries of the femur, tibia and fibula were extracted from CT bone density data. These 3D geometries, as well as the stereo images of the knee phantom, were then imported in Autoscoper for estimating the 3D position and orientation (pose) of the knee during the translational and rotational motion on the positional stage. The overall mean translational error was 0.151 $\pm$0.133 mm and the overall rotational tracking error was $0.41^{0}\pm$ 0.30^{0}. These results are similar to other studies based on model-based tracking methods and using stereo radiography systems. For example in Miranda et al [54] the rotational and translational tracking precision was 0.08^{0} and 0.45 mm, respectively while in Bey et al [25] the reported results for patellofemoral tracking were 0.4 mm for translational accuracy and 0.877^{0} for rotational accuracy.

Image intensifiers introduce significant geometric distortion that must be corrected in order to perform motion tracking. This can be achieved by imaging a commercially available radio opaque squared mesh with known positions of the holes (9255T641, McMaster-Carr, Robinson, NJ). Then the transformation, for removing distortion from the images, was calculated by using the XROMM Undistorter (Brown University,RI) software and was applied to all subsequent images. The relative positions and orientations of each fluoroscopy system were obtained after imaging a custom calibration cube enclosing 52 steel beads of precisely known position and size, positioned inside the capturing volume of the HSSR. The relative bead positions from each two-dimensional fluoroscopic image were then digitized by using a custom XROMM calibration tool from Brown University and established algorithms such as the direct linear transformation (DLT) algorithm [70].

In Vivo HSSR data collection

The in vivo HSSR data collection for the four different tasks consisted of two parts. Firstly, the bone tracking 3-D bone models are required and secondly, collecting the HSSR data during the four activities. The accurate 3D geometries of the knee bones were reconstructed from the CT data where for each subject a static bone CT with slice thickness of either 0.6 mm or 1.0 mm using a Siemens scanner, was obtained. Commercial software Scanip (Simpleware) was used to reconstruct the three-dimensional geometries of femur and tibia. The HSSR data of the subjects during the unloaded knee extension were captured at collection frequency of 50 Hz while for the remaining activities the collection frequency was 100 Hz. Bone tracking was performed using the XROMM Autoscoper software which optimized the positions of the three-dimensional bone models to the two-dimensional stereo radiography images in order to quantify pose (translation and rotation). The software allows the user to rotate and translate the 3D CT volume in order to perform 2D-3D matching for determining the tibiofemoral tracking throughout the range of motion [53] (Figure 5.2).

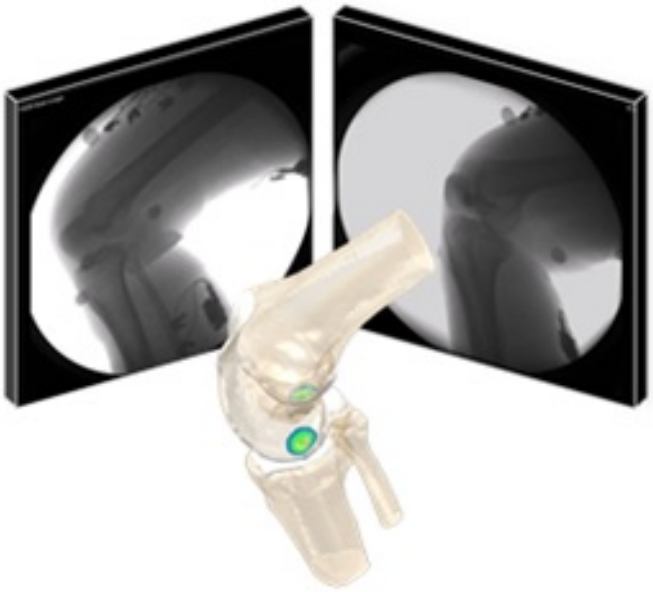

Figure 5.2: An image of the reconstructed femur and tibia/fibula. Autoscoper was used to align the projected contours of the imported bone geometries to the stereo images

To define the origin of the femoral coordinate system we used the same method as the one described in [61]. A cylinder was fitted to the medial and lateral posterior condyles and the center of the coordinate system was placed at the midpoint of the cylinder center line. The mediolateral axis (ML) was defined as the line through the long axis of the cylinder while the superior-inferior (SI) axis was aligned to the posterior line of the femur. The Anterior-posterior (AP) axis was defined as the cross product of the ML and SI axes. The femoral coordinate system was assigned to the tibia at full extension during the knee extension activity and it was set to be the ”zero” position (Figure 5.3). Using these coordinate systems, kinematics of the tibia relative to femur were calculated using methods described by Grood and Suntay [43].

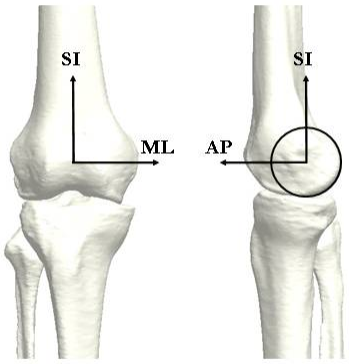

Figure 5.3: Representative bone geometry model derived from the CT scan depicting coordinate axis used to determine the reference position of the femur and tibia: superior(+)-inferior (SI), anterior(+)-posterior (AP), medial(+)-lateral (ML)

Data Analysis

Comparisons between the excursion and average values of internal-external and varus-valgus rotation, and anterior-posterior translation were made across subjects and activities. Our data during the dynamic trials have been normalized to percent cycle. Kinematics were filtered using a 4^{th} order low-pass Butterworth filter with a cutoff frequency of 15 Hz.

5.3 Results

During a baseline knee extension all subjects exhibited the same behavior throughout the 3DOF except from one participant who had different varus-valgus rotation with respect to the other subjects. Figure 5.4 shows the knee extension trial for all subjects for internal-

external (IE) and varus-valgus (VV) rotation and anterior-posterior translation (AP) with respect the flexion-extension (FE) angle. At full flexion the knee was internally rotated for all subjects and while knee was getting closer to full extension the rotation was constantly decreasing. The anterior tibial translation (ATT) was similarly higher at full extension and steadily decreased while the knee was extended. For varus-valgus rotation most subjects showed a consistent varus rotation throughout the range of knee extension trial except from one subject who had valgus rotation instead.

The dynamic activities, walking, pivoting and step descending, for IE, VV rotation and AP translation are presented with respect the percent cycle (Figures 5.5, 5.6,5.7). The tracking data for gait are for the stance period where the 0% represents the heel strike while the 100% is for the toe off. The average flat foot (FF) phase occurred at approximately 19% and the heel off (HO) phase at 48% which are somewhat similar to the existing data for gait analysis.

During the normal gait the majority of the subjects moved interiorly and the maximum internal rotation was 9^0. Most of the subjects for the same activity showed consistency regarding the varus-valgus rotation where five of them rotated into varus with a maximum angle of 6.5 ^{0} while only one subject rotated into valgus. The ATT maximum range was approximately 7mm and four subjects had more posterior translation while three subjects at full flexion started posteriorly and ended anteriorly at full extension.

Throughout the pivoting trial there was some variation among the subjects for the IE rotation and AP translation while for the VV rotation the subjects followed the same behavior as they did for knee extension. For the pivoting activity the 0% stands for heel strike and the 100% stands for the toe off. The highest average IE rotation among subjects was 8.38 $^0\pm3.75^0$, the highest average AP translation was 3.07mm$\pm$3.08mm and the highest average varus rotation was 4.87 $^0\pm0.78^0$ while for the valgus was $3.63^0\pm0.55^0$.

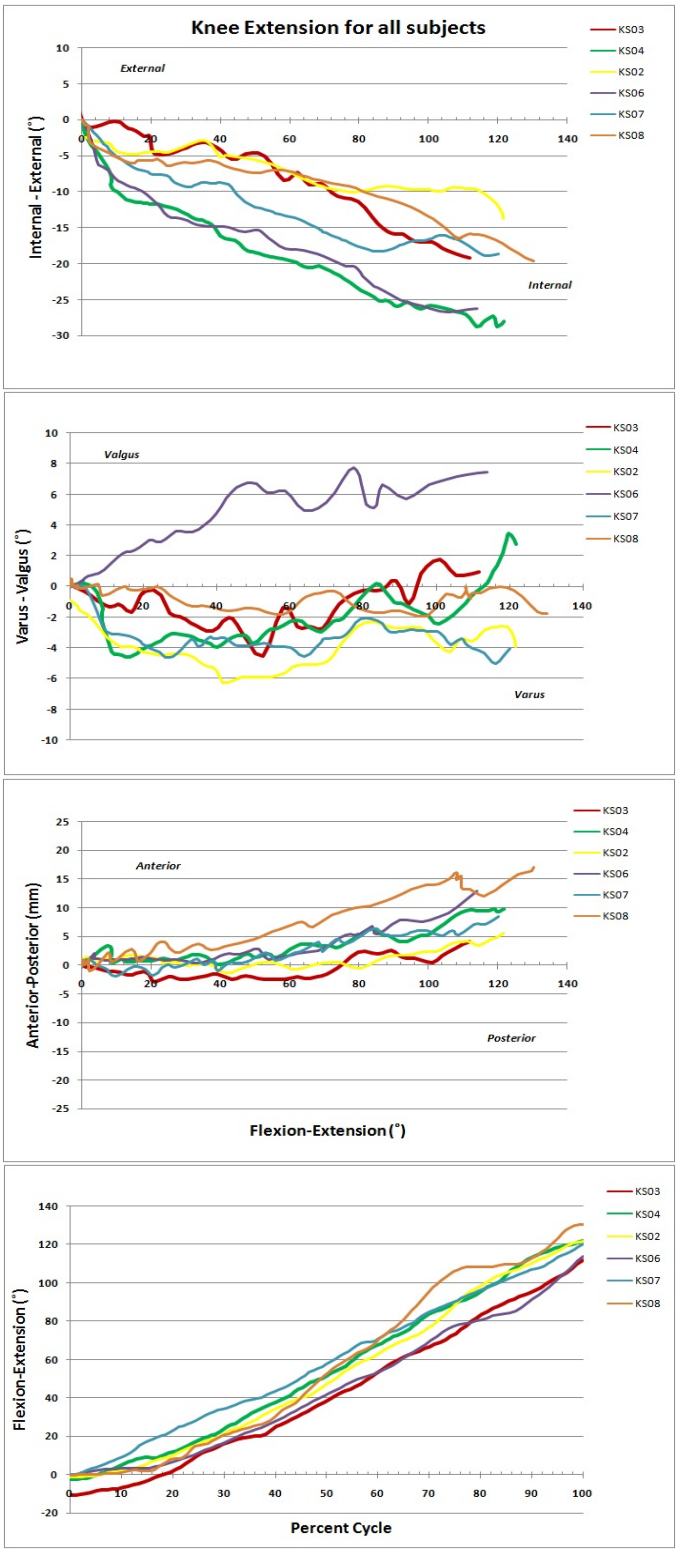

Figure 5.4: Knee Extension trial for 3DOF with respect flexion angle and Knee Extension with respect percent cycle

External and valgus rotations for walking and step descending activities as well as IE rotation for knee extension are found to be predominately negative. For step descending activity, 0% represents the first impact with the floor and the 100% represents the heel off. Full weight acceptance (FWA) was between approximately 10-22% and only for one participant the FWA happened at 47%. All subjects rotated internally and the highest average was $11.41^0 \pm 3.29^0$. For ATT the highest average was 3.36mm$\pm$1.21mm and for VV $-3.84^0 \pm 0.84^0$ and $4.31^0 \pm 0.86^0$ for varus and valgus rotation respectively.

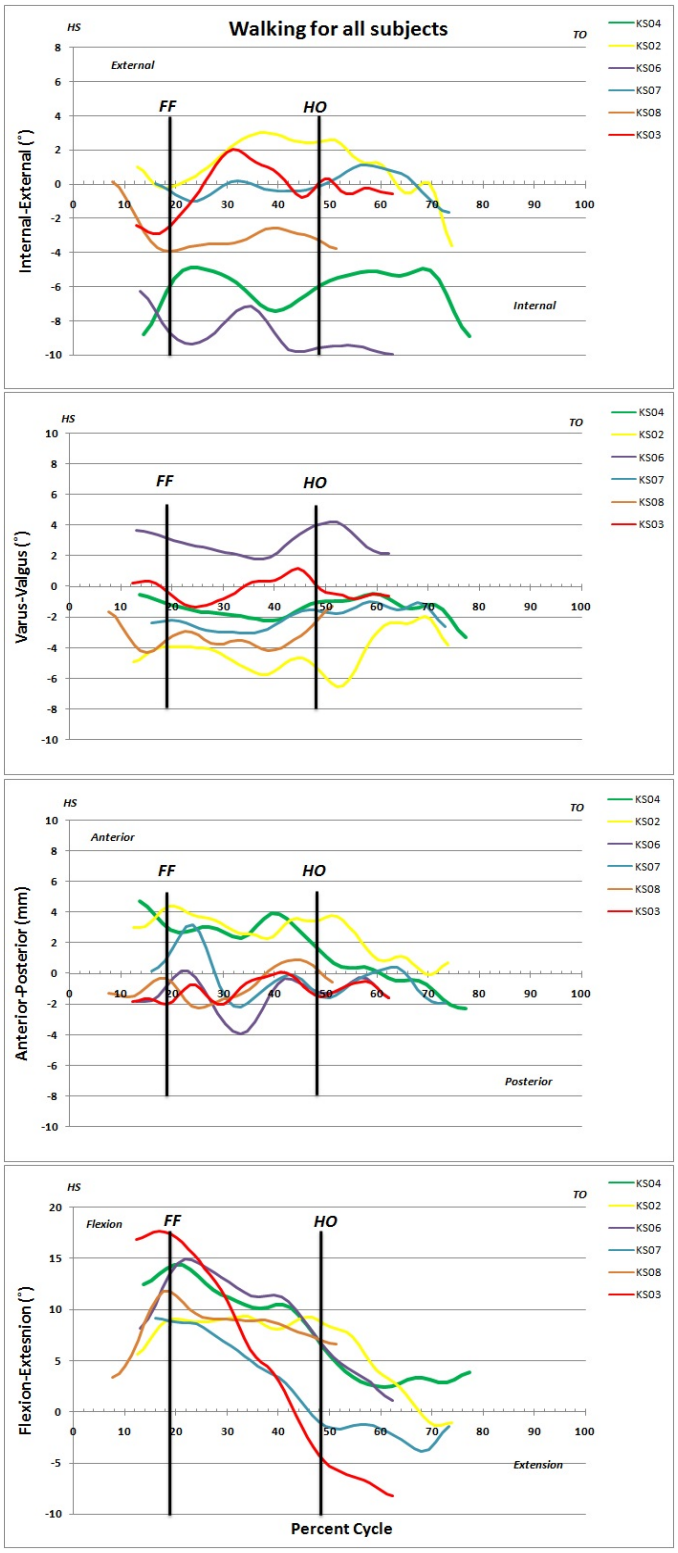

Figure 5.5: Normal Gait for the 3DOF and the Knee Extension trial

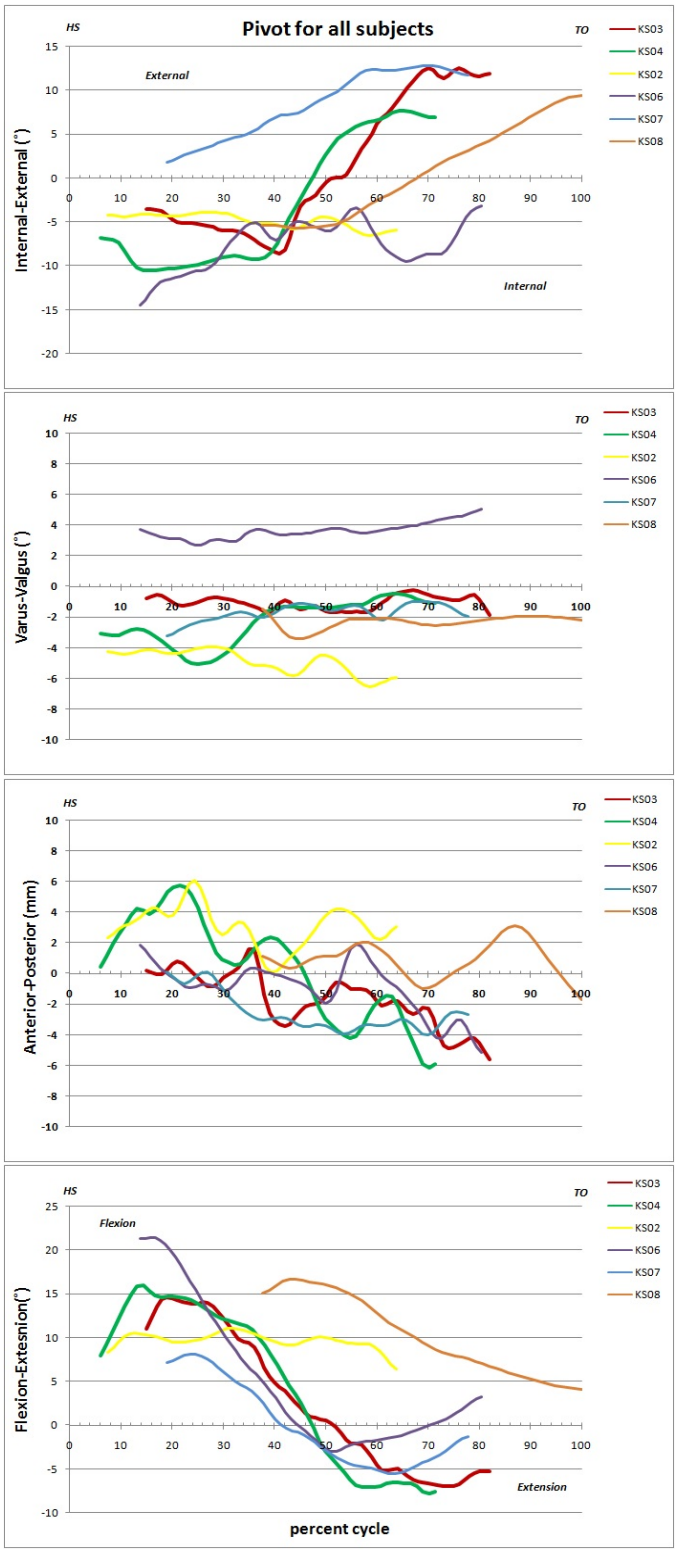

Figure 5.6: Pivot for the 3DOF and the Knee Extension trial

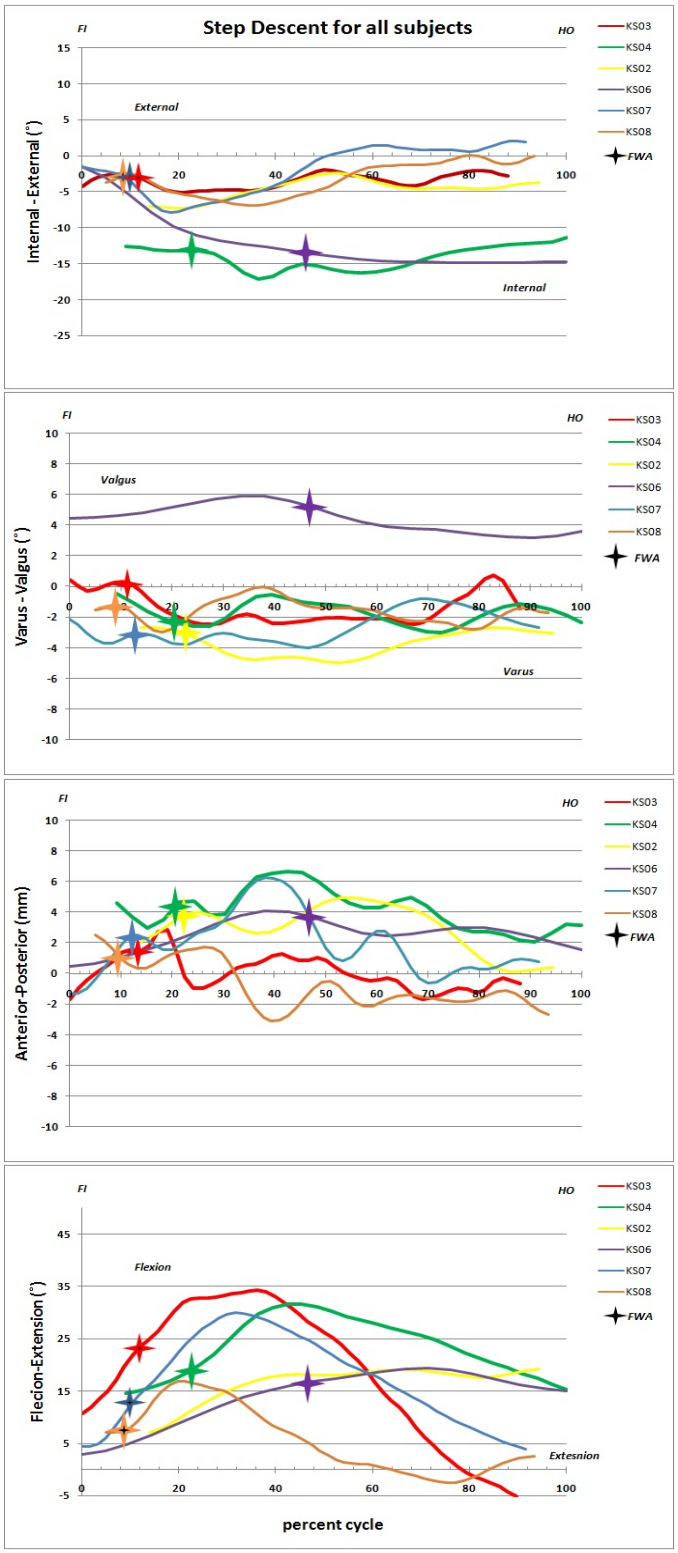

Figure 5.7: Step Descent for the 3DOF and the Knee Extension trial

Excursions during normal gait were lower than during the higher demand activities of pivoting and step descending as well as from a baseline knee extension. Figure 5.8 demonstrates the excursion data for all subjects along the activities. Greatest excursions among the dynamic activities are observed for IE rotation and AP translation throughout pivoting and step descending. The maximum excursion is 21.17^0 for IE rotation during the pivoting activity. The average values for excursion for IE rotation are 14.91$\pm$4.09, 8.64$\pm$4.32 and 4.36$\pm$1.32 for pivoting step descending and walking respectively, 2.55$\pm$1.06, 3.26$\pm$0.79, 2.92$\pm$0.89 for VV rotation and 6.61$\pm$3.07, 6.40$\pm$1.49, 4.36$\pm$1.71 for AP translation. Thus, IE rotation for step descent and pivot is two or three times greater than normal gait while for VV rotation only small differences are noted. The AP translation for pivot and step descent tasks is roughly 50% greater than walking. Table 5.2 summarizes all the average and excursion values for the 3DOF described here for all 4 activities and subjects. Excursion is calculated as the difference between the maximum and the minimum for each DOF. The greatest average excursion among the 4 activities is observed for the knee extension for all 3DOF with 20.59 $\pm$ 9.57 and 5.75$\pm$2.53 for IE and VV rotations respectively and 8.64$\pm$3.28 for the AP translation.

Finally Figure 5.9 demonstrates all the activities together for each subject individually for IE, VV rotation and AP translation. The data points in these graphs help us to investigate the correlation with the knee flexion angle and demonstrate that V/V rotation is less activity dependent in comparison with the IE rotation and AP translation. These results can also be supported from Tables 5.3 and 5.4 that show the standard deviations of the average standard deviations and the standard deviation for the excursions for the 3DOF across the activities.

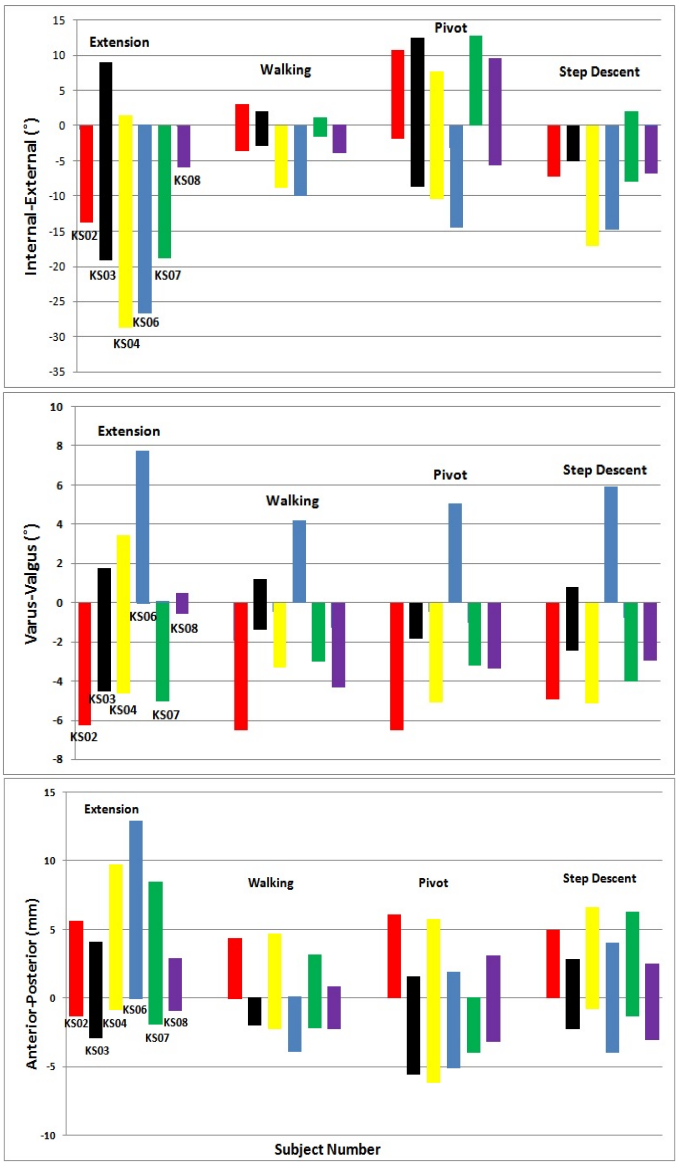

Figure 5.8: Excursion plots for the 3DOF for all the activities.I/E (top), V/V (middle), A/P (bottom)

Variable	Subjects	Average ± Standard Deviation /Excursion			
		Knee Extension	Pivot	Step Descent	Walking
Int.- Ext.(^{o})	KS02	-6.41±3.22	3.13±3.57	-4.73±1.54	1.15±1.49
		13.29	12.58	4.93	6.65
	KS03	-5.38±7.53	1.12±7.57	-3.49±1.03	-0.28±1.37
		28.20	21.17	3.20	4.93
	KS04	-17.13±8.58	-3.02±7.24	-11.22±3.95	-6.07±1.14
		30.15	18.15	13.47	4.03
	KS06	-7.65±4.55	-7.57±2.78	-11.41±3.29	-8.80±1.03
		26.92	11.32	13.35	3.66
	KS07	-12.11±5.36	8.38±3.75	-1.96±3.20	-0.09±0.69
		18.96	10.94	9.92	2.77
	KS08	-2.31±2.28	1.54±5.62	-3.23±2.32	-2.98±1.00
		6.00	15.30	6.97	4.10
Var.- Val.(^{o})	KS02	-3.67±1.53	-4.87±0.78	-3.84±0.84	-4.28±1.22
		6.08	2.58	2.26	4.57
	KS03	-0.97±1.39	-1.03±0.43	-1.37±1.06	-0.24±0.69
		6.31	1.63	3.25	2.58
	KS04	-1.73±2.03	-2.37±1.46	-2.45±1.22	-1.43±0.63
		8.08	4.59	4.68	2.87
	KS06	4.07±2.55	3.63±0.55	4.31±0.86	2.89±0.75
		7.79	2.38	3.24	2.43
	KS07	-3.21±1.14	-1.71±0.54	-2.65±0.99	-2.04±0.66
		5.10	2.23	3.21	2.01
	KS08	-0.0001±0.23	-2.33±0.40	-1.63±0.75	-3.32±0.80
		1.11	1.89	2.94	3.04
Ant.- Post. (mm)	KS02	1.21±1.60	3.07±3.08	3.36±1.21	2.56±1.29
		6.97	3.15	4.60	4.46
	KS03	-0.82±1.68	-1.66±1.79	-0.004±1.13	-1.09±0.61
		7.03	7.19	5.09	2.08
	KS04	3.37±3.04	0.33±3.37	2.87±2.04	1.51±1.95
		10.57	11.89	7.47	6.98
	KS06	2.96±2.88	-1.20±1.74	0.42±2.37	-1.40±1.12
		12.94	7.04	8.07	4.10
	KS07	2.57±2.81	-2.57±1.24	1.75±2.05	-0.33±1.39
		10.44	4.05	7.63	5.39
	KS08	0.70±0.90	0.53±1.54	-0.78±1.51	-0.79±0.97
		3.86	6.33	5.56	3.16

Table 5.2: Average and Excursion values for the 3 DOF for all subjects and activities

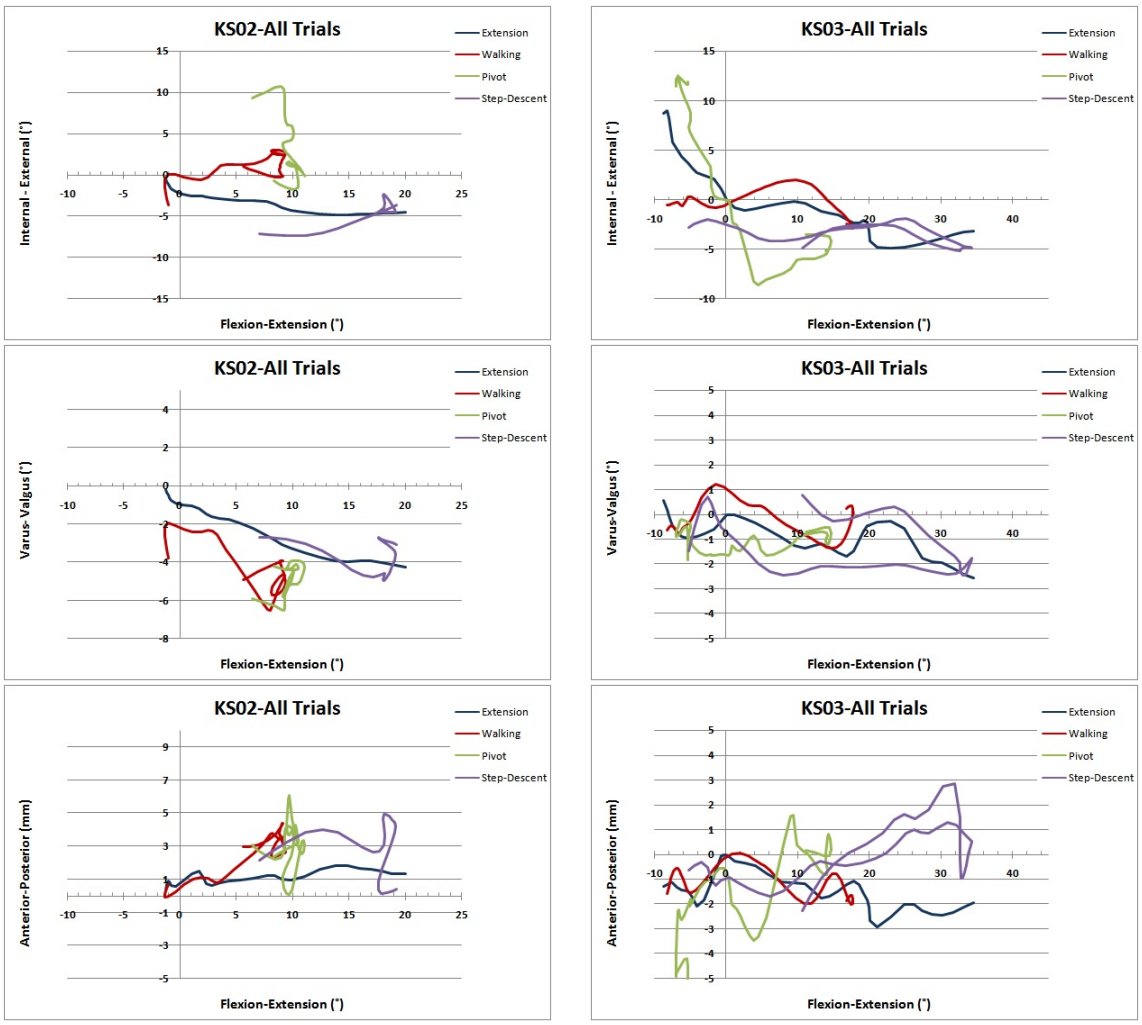

Stand Deviation of the Excursion			
Activities	**IE**	**VV**	**AP**
Extension	7.12	1.24	2.57
Gait	1.32	0.89	1.71
Pivot	4.58	1.12	3.07
Step Descent	4.74	0.87	1.49

Table 5.3: Standard deviation of the Excursion

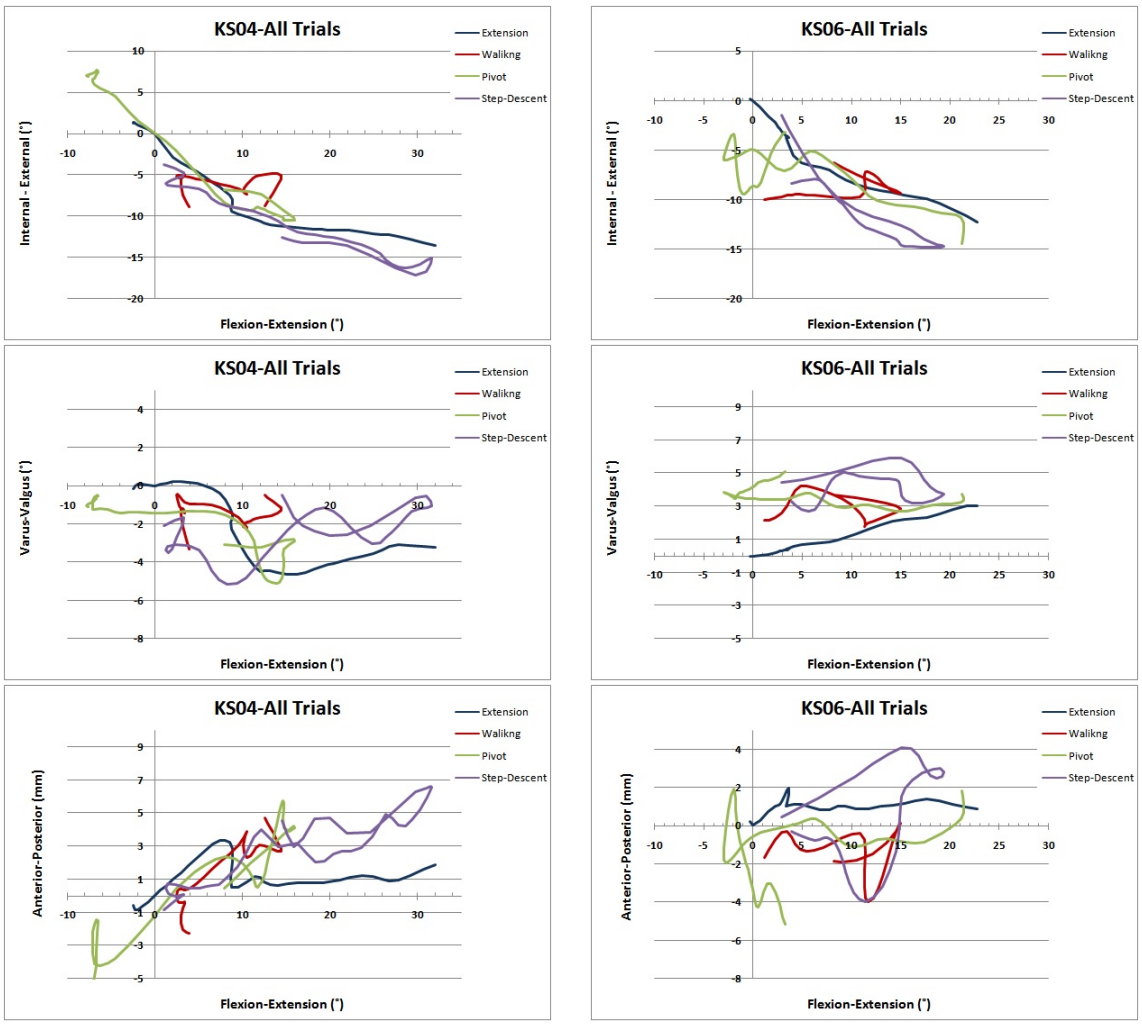

Stand Deviation of the Averages Stand. Deviation			
Activities	**IE**	**VV**	**AP**
Extension	2.44	0.79	0.88
Gait	0.29	0.22	0.45
Pivot	2.02	0.40	0.88
Step Descent	1.12	0.17	1.49

Table 5.4: Standard Deviation of the average standard deviations

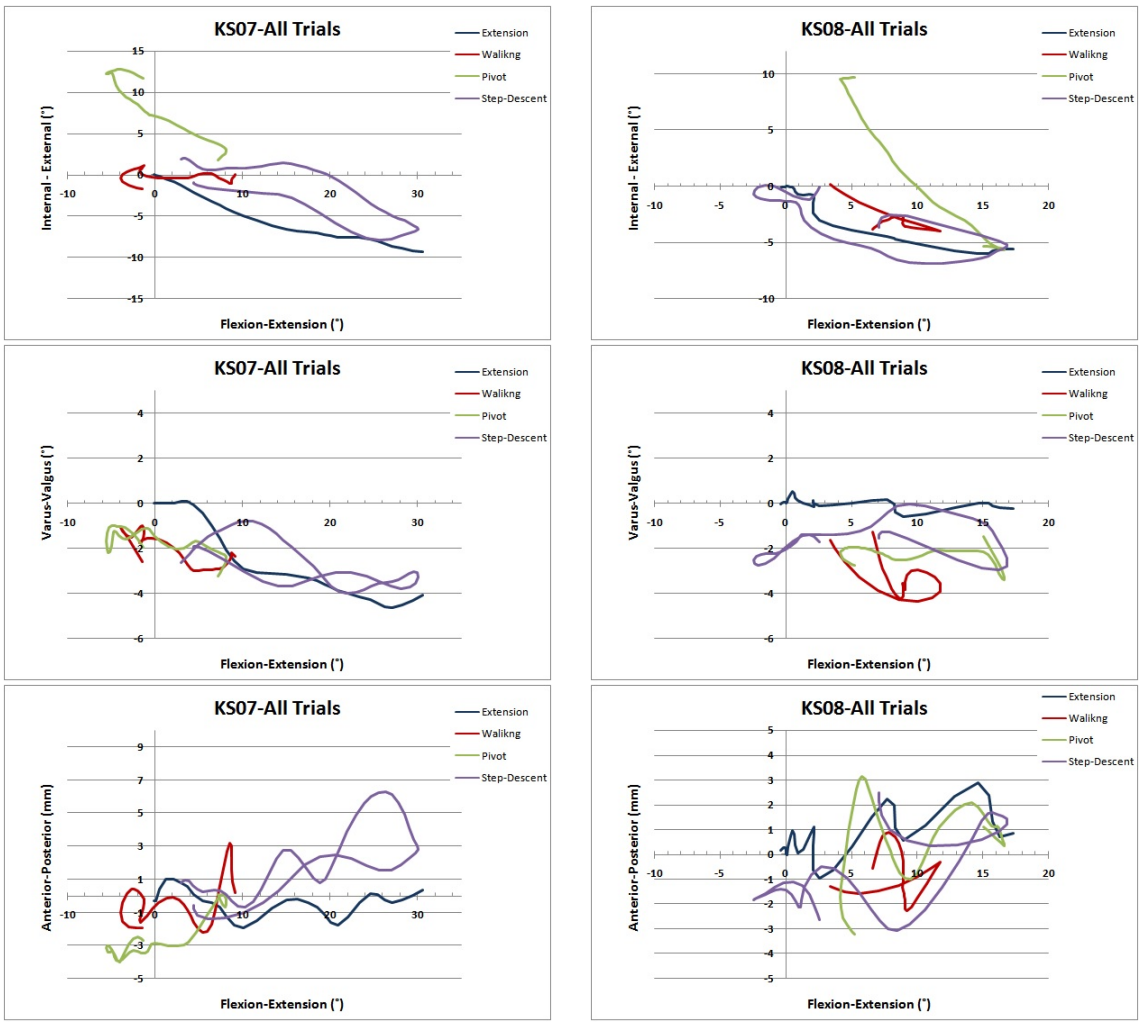

Figure 5.9: All trials together for each subject individually

5.4 Discussion

Accurate knowledge of 6DOF normal knee kinematics is essential for providing information on the function of the knee that can be used in order to improve current treatments of knee pathology. In this chapter we used high speed stereo radiography system to investigate the kinematics of six healthy knees of older people during a baseline knee extension and during dynamic activities of daily living including walking, pivoting and step descending.

The results confirmed our hypotheses that the IE rotation and AP translation are more activity dependent as compared to VV rotation based on the excursion plots. Excursion in VV was approximately 3^0 for the three dynamic activities while IE and AP had different excursion among the trials with the highest IE excursion reported for the pivoting (14.91^0). Furthermore, IE and AP were greater during the higher demand activities than normal gait. The average values for excursion for IE rotation are 14.91 ± 4.09, 8.64 ± 4.32 and 4.36 ± 1.32 for pivoting step descending and walking respectively and 6.61 ± 3.07, 6.40 ± 1.49, 4.36 ± 1.71 for AP translation. These results are consistent with those found by Myers et al [61] regarding the IE rotation where landing ($8.9^0\pm2.5^0$), maximum isometric contraction ($16.6^0\pm7.2^0$) and unweighted full knee extension ($16.1^0\pm6.8^0$), each produced higher IE rotation range than walking ($4.2^0\pm4.0^0$).

While there has been no study in vivo that compared tibiofemoral kinematics in older people during pivoting and step descending, the unloaded knee extension and walking have been investigated and our data are similar to those reported for walking and landing. Our measurements for walking with respect to axial rotation of the knee showed an internal rotation with an average value of 3^0 and this is similar with the values reported in Kozanek et al [63] ($1.6\ ^0$ at heel strike to $7.4\ ^0$ at toe off). IE had the greater excursion value among the activities and the biggest variation in the way participants performed the pivoting trial. During step descending is also observed a relative high range of IE ($8.64^0\pm4.31^0$) and is interesting that this value matches with the one found by Myers et al for landing activity [61] ($8.9^0 \pm 2.5\ ^0$). Our peak internal rotation was found to be $18.9^0 \pm 8.4^0$ for knee extension, $8.4^0\pm 5.9^0$ for pivoting, $9.9^0\pm4.9^0$ for step descent and $-5.2^0\pm3.4^0$ for walking. These results are different with the ones reported in Myers et al [61] where the corresponding peak IE values are $14.5^0 \pm 7.7\ ^0$ for knee extension, $19.4^0 \pm 5.7\ ^0$ for landing and $3.9^0 \pm 4.2^0$ for walking.

ATT had an average excusrion of approximately 6.5mm for the higher demand activities of pivoting and step descending and 4.4 mm for the normal gait. Li et al [64] measured knee kinematics for one healthy individual during walking and found similar values that showed ATT to range from approximately 5 mm during midstance to -2.5mm at toe off. Kozanek et al [63] also used dual plane fluoroscopy for measuring knee kinematics of 8 healthy individuals during gait and the average excursion for the AP directions were approximately 5mm. Our results are also very similar with those one found by Myers et al [26]. In Myers et al the tibiofemoral kinematics of soft and stiff drop landings for 16 healthy subjects were investigated and the maximum absolute of ATT translation was 6.4mm$\pm$2.4mm and 6.7mm$\pm$2.9mm for stiff and soft landings respectively. However, in another study of Myers et al [61], where the tibiofemoral kinematics during activities of increasing demand were measured, the results for the AP translation range were 2.9 $\pm$ 1.7mm for landing, 3.9 $\pm$ 2.6mm for walking and 3.3 $\pm$ 1.8mm for unweighted knee extension which are somewhat lower than the ones we found for the AP translation during the dynamic activities. In the same study [61] the peak ATT translation was reported to be 5.6 $\pm$ 1.9mm for landing, 3.1 $\pm$ 2.2 mm for walking and 2.6 $\pm$ 2.1mm for the unweighted knee extension whereas in our study the peak ATT was found to be higher for knee extension (7.3 $\pm$ 3.8mm) the step descend (4.5 $\pm$ 1.7mm) showed similar value with the one found for landing while the for pivoting the peak ATT was found to be smaller (3.1 $\pm$ 2.4mm). Similar results were found for the walking activity (2.2 $\pm$ 2.1 mm) as well. In Torry et al [64] they measured tibiofemoral kinematics during drop landings and the value reported for the total ATT excursion was 2.1 $\pm$ 0.9mm. This value is lower because tibial translations and rotations measured during landing were referenced to un unloaded knee extension.

Regarding the abduction-adduction motion of the knee, VV rotation was consistent along the different activities and the highest average range was noted during step descending ($3.26^0 \pm 0.79^0$). Five out of six subjects showed a consistent varus rotation of the tibia

relative to the femur across all activities. Only one subject rotated into valgus for all trials. These results are consistent with other studies that have reported the knee to rotate into varus [71, 72] during the stance phase of gait and other researchers found valgus rotation as in Lafortune et al [1] who investigated the tibiofemoral kinematics during normal gait by means of intracortical traction pins placed in the femur and tibia of 5 healthy participants. Seisler et al [2] measured tibiofemoral kinematics during a voluntary knee extension-flexion using fast-PC (dynamic) magnetic resonance imaging and found an average for varus rotation of 1^0.

The limitations of our study should be noted. We measured knee kinematics for six healthy older subjects in a controlled laboratory environment and some of the subjects showed some difficulty in naturally behaving throughout the tasks although prior to the data collection the participants took several practices in how to perform the activities. In addition, the amount of subjects may be considered relatively small so follow-up work should include more subjects for better representation of the analysis of the tibiofemoral kinematics. We also measured kinematics during the stance phase of gait and our tracking data did not include the heel strike or toe off phase due to the limitation of the HSSR system because it is difficult to capture the entire motion. That can be corrected by running separate activities and capturing the ranges of motion we are interested in.

In conclusion, this study investigated the 6DOF of healthy knee kinematics for a cohort age-matched to TKA recipients during four activities. The data showed that pivoting can be the most challenging activity since it showed the biggest variation and excursion among the activities. We saw that higher demand tasks, pivoting and step descending, as well as a baseline knee extension had greater IE rotation and AP translation than normal gait. Furthermore, IE rotation and AP translation, proved to be more activity dependent than VV rotation. We believe that these data will establish a useful baseline for the envelope of healthy knee motion. One of the future goals is to measure knee kinematics during the same

activities to older subjects with TKA for subsequent comparison with the findings reported from this study. Additionally, a further investigation should be conducted for comparing healthy knee kinematics between younger and older people sring the same activities and to establish whether they have similar kinematic patterns.

Bibliography

[1] M.A. Lafortune, P.R. Cavanagh, H.J. Sommer, and A. Kalenak. Three-dimensional kinematics of the human knee during walking. *Journal of Biomechanics 25, 347-357*, 1992.

[2] A.R. Seisler and F.T. Sheehan. Normative three-dimensional patellofemoral and tibiofemoral kinematics: A dynamic in vivo study. *IEEE transactions on biomedical engineering 54, 1333-1341*, 2007.

[3] Tung-Wu Lu, Tsai Tsung-Yuan, Kuo Mei-Ying, Hsu Horng-Chaung, and Chen Hao-Ling. In vivo three-dimensional kinematics of the normal knee during active extension under unloaded and loaded conditions using single-plane fluoroscopy. *Medical Engineering and Physics 1004-1012*, 2008.

[4] M.R Torry, K.B.Shelburne, D.S.Peterson, J.E.Giphart, J.P.Krong, C.A.Myers, J.R. Steadman, and S.L. Woo. Knee kinematic profiles during drop landings a biplane fluoroscopy study. *Medicine and Science in Sports and Exercise 43, 533-541*, 2011.

[5] V.M. Goldberg and B.D. Henderson. The freeman-swanson iclh total knee arthroplasty. *Journal of bone and Joint Surgery 62A, 1338-1344*, 1988.

[6] O.M. Mahoney, P.C.Nobel, D.D.Rhoads, J.W.Alexander, and H.S.Tullos. Posterior cruciate function following total knee arthroplasty. *Journal of Arthroplasty 9, 569-578*, 1988.

[7] P.T. Andriacchi, S.T. Stanwyck, and J.O. Galante. Knee biomechanics and total knee replacement. *Journal of Arthroplasty, Vol 1*, 1985.

[8] S.A. Wilson, P.D.MaCann, and R.S.Gotlin. Comprehensive gait analysis in posterior-stabilized knee arthroplasty. *Journal of Arthroplasty 11, 359-357*, 1996.

[9] D.A. Dennis, R.D.Komistek, , and J.B.Stiehl. Range of motion after total knee arthroplasty: the effect of implant design and weight-bearing conditions. *Journal of Arthroplasty 13, 748-752*, 1998.

[10] J.B. Stiehl, D.A. Dennis, R.D.Komistek, and P.A.Keblish. In vivo kinematic analysis of a mobile bearing total knee proshesis. *Clinical of Orthopaedics and Related Research 345, 60-66*, 1997.

[11] R. Stagni, S. Fantozzi, A.Cappello, and A.Leardini. Quantification of soft tissue artefact in motion analysis by combining 3d fluoroscopy and stereophotogrammetry: a study on two subjects. *Clinical Biomechanics 20, 320-329*, 2005.

[12] R.D. Komistek, D.A.Dennis, and M.Mahfouz. In vivo fluoroscopic analysis of the normal human knee. *Clinical orthopaedics and related research 410,69-81*, 2003.

[13] S. Fukagawa, A. Leardini, B. Callewaert, P.D. Wong, L. Labey, and K. Desloovere. Age-related changes in kinematics of the knee joint during deep squat. *The Knee 19, 208-212*, 2012.

[14] J.P. Holden, J.A. Orsini, and S.J.Stanhope. Estimates of skeletal motion:movement of surface-mounted targets relative to bone during gait. *Biomedical Engineering Recent Developments , 1035-1038*, 1994.

[15] B.M. You, P.Siy, W.Anderst, and S.Tashman. In vivo measurement of 3-d skeletal kinematics from sequences of biplane radiographs:application to knee kinematics. *IEEE Transactions on Medical Imaging 20(6),514-525.*, 2001.

[16] G. Li, T.H.Wuerz, and L.E.Defrate. Feasibility of using orthogonal fluoroscopic images to measure in vivo joint kinematics. *Journal of Biomechanical Engineering 126(2), 314-318*, 2004.

[17] B.J. Fregly, Haseeb A.Rahman, and Scott A.Banks. Theoritical accuracy of model-based shape matching for measuring natural knee kinematics with single-plane fluoroscopy. *Journal of Biomechanical Engineering Vol.127*, 2005.

[18] M.R. Mahfouz, S.M.Traina, R.D.Komistek, and D.A.Dennis. In vivo determination of knee kinematics in patients with a hamstring or patellar tendon acl graft. *Journal of Knee Surgery 16, 197-202*, 2003.

[19] A. Banks and W.A. Hodge. Accurate measurement of three-dimensional knee replacement kinematics using single-plane fluoroscopy. *IEEE transactions on Biomedical Engineering, Vol.43, N0 6*, 1996.

[20] National Hospital Disacharge Survey. *National canter of Health Statistics*, 1991.

[21] M. R. Mahfouz, W.A. Hoff, and D.A. Dennis. A robust method for registration of three-dimensional knee implant models to two-dimensional fluoroscopy images. *IEEE Trans Med Imaging 22, 1561-74*, 2003.

[22] W.A. Hoff, R.D.Komistek, D.A. Dennis, S.M.Gabriel, and S.A.Walker. Three-dimensional determination of femoral-tibial contact positions under in vivo conditions using fluoroscopy. *Clin.Biomechanics 13, 455-472*, 1998.

[23] S. Acker, R.Li, H. Murray, P.S.John, S.Banks, S.Mu, U.Wyss, and K.Deluzio. Accuracy of single-plane fluoroscopy in determining relative position and orientation of total knee replacement components. *Journal of Biomechanics 44 784-787*, 2011.

[24] N. Nishinaka, H.Tsutsui, K. Mihara, K. Suzuki, D. Makiuchi, Y. Kon, T.W. Wright, M.W. Moser, K. Gamada, H. Sugimoto, and S.A. Bansks. Determination of in vivo glenohumeral translation usinf fluoroscopy and shape-matching techniques. *J Shoulder Elbow Surg, 319-322*, 2008.

[25] M.J. Bey, Stephanie K Kline, Scott Tashman, and Roger Zauel. Accuracy of biplane x-ray imaging combined with model-based tracking for measuring in-vivo patellofemoral joint motion. *Journal of orthopaedic Surgery and Research;3:38.*, 2008.

[26] C.A. Myers, M.R. Torry, D.S. Peterson, K.B. Shelburne, J.E. Giphart, J.P. Krong, S.L. Woo, and J.R. Steadman. Measurements of tibiofemoral kinematics during soft and stiff drop landings using biplane fluoroscopy. *The American Journal of Sports Medicine 39, 1714-1722*, 2011.

[27] G. Li, S.K. Van de Velde, and J.T. Bingham. Validation of a non-invasive fluoroscopic imaging technique for the measurement of dynamic knee joint motion. *Journal of Biomechanics 41, 1616-1622*, 2008.

[28] E.A. Ijsseldijki, E.R. Valstar, B.C. Stoel, R.G.H. Nelissen, J.H.C. Reiber, and B.L. Kaptein. The robustness and accurcy of in vivo linear wear measurements for knee prostheses based on model-based rsa. *Journal of Biomechanics 44, 2724-2727*, 2011.

[29] A.H. Prins, B.L. Kaptein, B.C. Stoel, R.G.H. Nelissen, J.H.C. Reiber, and E.R. Valstar. Integrated contour detection and pose estimation for fluoroscopic analysis of knee implants. *Journal of Engineering in Medicine 225*, 2011.

[30] B.L. Kaptein, E.R. Valstar, B.C. Stoel, P.Rozing, and J.H.C. Reiber. A new model-based rsa method validated using cad models and models from reversed engineering. *Journal of Biomechanics 36, 873-882*, 2003.

[31] J. Canny. A computational approach to edge detection. *IEEE Trans. Pattern Anal. Machine Intell. 8, 679-698*, 1986.

[32] S. Zuffi, A.Leardini, F.Catani, S.Fantozzi, and A. Cappello. A model-based method for the reconstruction of total knee replacement kinematics. *IEEE Trans. Med. Imag 18, 981-991*, 1999.

[33] W.R. Ledoux, R. Tsai, M.Fassbind, B.J.Sangeorzan, and D.R.Haynor. Using biplane fluoroscopy to quantify foot bone motion. *Conference of the Annual Meeting of the American Soc, 597*, 2010.

[34] M.J. Bey, R. Zauel, M.Fassbind, S.K.Brock, and S.Tahman. Validation of a new model-based tracking technique for measuring three-dimensional, in vivo gleno-humeral joint kinematics. *Journal of Biomechanical Engineering 128, 604-609*, 2006.

[35] D.F. Massimini, J.J.P. Warner, and G.Li. Non-invasive determination of coupled motion of the scapula and humerous-an in vitro validation. *Journal of Biomechanical Engineering 44, 408-412*, 2011.

[36] D.E. Martin, N.J. Greco, B.A. Klatt, V.J. Wright, W.J. Anderst, and S. Tashmann. Model-based tracking of the hip: Implications for novel analysis of hip pathology. *The Journal of Arthroplasty 26, 88-97*, 2011.

[37] G. Li, S. Wang, P. Passias, Q. Xia, G. Li, and K. Wood. Segmental in vivo vertebral motion during functional human lumbar spine activities. *Eur Spine J 18, 1013-1021*, 2009.

[38] B.J. Fregly, H.A. Rahman, and S.A. Banks. Theoretical accuracy of model-based shape matching for measuring natural knee kinematics with single-plane fluoroscopy. *Journal of Biomechanical Engineering 127, 692-699*, 2005.

[39] D.C. Ackland, F. Keynejad, and M.G. Pandy. Future trends in the use of x-ray fluoroscopy for the measurement and modelling of joint motion. *Journal of Engineering in Medicine 225*, 2011.

[40] P.W. de Bruin, B.L. Kaptein, B.C. Stoel, J.H. Reiber, P.M. Rozing, and E.R. Valstar. Image-based rsa: Roentgen sterophotogrammetric analysis based on 2d-3d image registration. *Journal of Biomechanics 41(1),155-164*, 2008.

[41] S. Tashman and W. Anderst. In vivo measurement of dynamic joint motion using high speed biplane radiography and ct: Application to canine acl deficiency. *ASME Journal of Biomechanics Eng.125(2), 238-245*, 2008.

[42] H.J. Woltring. Planar control in multi-camera calibration for 3-d gait studies. *Journal of Biomechanics 13, 39-48*, 2008.

[43] E.S. Grood and W.J. Suntay. A joint coordinate system for the clinical description of three dimensional motions: Application to knee. *Journal of Biomechanical Engineering , 105-137*, 1983.

[44] E. Garling, B. Kaptein, K. Geleijns, R. Nelissen, and E. Valstar. Marker configuration model-based roentgen fluoroscopic analysis. *Journal of Biomechanics 38(4), 893-901*, 2005.

[45] R.O. Duda and P.E. Hart. Pattern classifications and scene analysis. *John Wiley and Sons, New York*, 1973.

[46] G. Selvic. Roentgen stereophotogrammetry. a methd for the study of the kinematics of the skeletal system. *Acta Orthopaedica Scandinavica 231, 1-51*, 1989.

[47] J. Ranstam, L. Ryd, and I. Onsten. Accurate accuracy assessement: review of basic principles. *Acta Orthopaedica Scandinavica 71(1), 106-108*, 2000.

[48] G.B Sharma, S.K. Saevarsson, S. Amiri, S. Mondogomery, H. Ramm, D.D. Lichti, R. Lieck, S. Zachow, and C. Anglin. Radiological method for measuring

patellofemoral tracking and tibiofemoral kinematics before and after total knee replacement. *Bone Joint Res 1(10), 263-271*, 2012.

[49] M.J. Bey, S.K. Kline, R. Zauel, T.R Lock, and P.A. Kolowich. Measuring dynamic in vivo glenohumeral joint kinematics: technique and preliminary results. *Journal of Biomechanics 41(3), 711-714*, 2008.

[50] H. Graichen, T. Stammburger, H. Bonel, E. Karls-Hans, M. Reiser, and F. Eckstein. Glenohumeral transaltion dyring active and passive elevation of the shoulder, a 3d open-mri study. *Journal of Biomechanics 33(5),609-613*, 2000.

[51] R.M. von Eisenhart-Rothe, A. Jager, K.H. Englmeier, T.J. Vogl, and H. Graichen. Relevance of arm position and muscle activity on three-dimensional glenohumeral translation in patients with traumatic and atraumatic shoulder instability. *American Journal of Sports of Medicine 30(4), 514-522*, 2002.

[52] J. E. Giphart, Christofer A.Zirker, Casey Myers, W. Wesley Pennigton, and Robert F. Laprade. Accuracy of a contour-based biplane fluoroscopy technique for tracking knee joint kinematics of different speeds. *Journal of Biomechanics*, 2012.

[53] D.L. Miranda, J.B. Scwartz, A.C. Loomis, E.L. Brainerd, B.C. Fleming, and J.J. Crisco. Static and dynamic error of a biplanar videoradiography system using marker-based and markerless tracking techniques. *J Biomech Eng. 133(12)*, 2011.

[54] D.L. Miranda, P.D. fadale, M.J. Hulstyn, R.M. Shlvoy, J.T. Machan, and B. C. Fleming. Knee biomechanics during a jump-cut maneuver: Effects of gender and acl surgery. *Med Sci Sports 45(5), 942-951*, 2013.

[55] S. Thompson. Direc linear transformation. *ME EN 363 notes*, 2011.

[56] K.L. Markolf, B.L. William, S. C.Shoemaker, and H.C.Amstutz. The role of joint load in knee stability. *Bone Jt. Surg. 63, 570-585*, 1981.

[57] P.A. Torzilli, X.Deng, and R.F. Warren. The effect of joint-compressive load and quadriceps muscle force on knee motion in the intact and anterior cruciate ligament-sectioned knee. *Am J Sports Med 22, 105-112*, 1994.

[58] G. Bergmann, F.Graichen, and A.Rohlmann. Hip joint loading during walking and running, measured in two patients. *Journal of Biomechanics 26, 969-90*, 1993.

[59] D. A. Douglas, Mohamed R. Mahfouz., R. D. Komistek, and W. Hoff. In vivo determination of normal and anterior cruciate ligament-deficient knee kinematics. *Journal of biomechanics 38 ,241-253*, 2005.

[60] T.Y. Tsai, T.W.Lu, M.Y Kuo, and H.C. Hsu. A volumetric model-based 2-d/3-d registration method for measuring kinematics of natural knees with single-plane fluoroscopy. *Journal of Medical Physics 37, 0094-2405*, 2010.

[61] C.A. Myers, M.R.Torry, D.S.Peterson, K.B.Shelburne, Giphart R.F. Laprade, S.L.Woo, and J.R.Steadman. In vivo tibiofemoral kinematics during 4 functional tasks of increasing demand using biplane fluoroscopy. *The American journal of Sports Medicine,Vol 40.No. 1*, 2012.

[62] T.E. Hewett, G.D.Myer, and K.R.Ford. Biomechanical measures of neuromuscular control and valgus loading of the knee predict anterior cruciate ligament injury risk in female athletes a prospective study. *Am J Sports Med 33, 492-501*, 2005.

[63] M. Kozanek, A. Hosseini, F. Liu, S.K Van de Velde, T.J. Gill, H.E. Rubash, and G. Li. Tibiofemoral kinematics and condylar motion during the stance phase of gait. *Journal of Biomechanics 42(12), 1877-1884*, 2009.

[64] G. Li, M. Kozanek, A. Hosseini, F. Liu S.K. Van De Velde, and H.E. Rubash. New fluoroscopic imaging technique for investigation of 6dof knee kinematics during treadmill gait. *J of Orthopaedic Surgery and Research, 1-6*, 2009.

[65] J.S. Li, A. Hosseini, L. Cancre, N. Ryan, H.E. Rubash, and G. Li. Kinematic characteristics of the tibiofemoral joint during a step-up activity. *Gait and Posture 38, 712-716*, 2013.

[66] J. L. Pfeiffer, S. Zhang, and C.E. Miller. Knee biomechanics during popular recreational and daily activities in older men. *The Knee 21, 683-687*, 2014.

[67] I.H. Chen, Y.R. Yang, S.J. Cheng, and R.Y. Wang. Differences in kinematic and electromyographic characteristics between young and older adults during circular turning. *International Journal of Gerontology 7, 162-166*, 2013.

[68] T. Hortobagyi, C. Mizelle, S. Beam, and P. DeVita. Old adults perform activities of daily living near their maximal capabilities. *Journal of Gerontology 58(5), 453-460*, 2003.

[69] S.J Olney, M.P. Griffin, and I.D McBride. Temporal, kinematic and kinetic variables related to gait speed in subjects with hemiplegia: a regression approach. *Phys Ther 74, 872-885*, 1994.

[70] E.L. Brainerd, D.B. Baier, S.M Gatesy, T.L. Hedrick, K.A. Metzger, S.L. Gilbert, and J.J. Crisco. X-ray reconstruction of moving morphology (xromm): precision, accuracy and applications in comparative biomechanics research. *J Exp Zool A Ecol Genet Physiol 313(5), 262-279*, 2010.

[71] T.P Andriacchi, E.J. Alexander, M.K. Toney, C. Dyrbry, and J. Sum. A point cluster method for in vivo motion analysis: applied to a study of knee kinematics. *J Biomech 120(6), 743-749*, 1998.

[72] X.M. Li, B. Liu, B. Deng, and S.M. Zhang. Normal six-degree-of-freedom motions of the knee joint during level walking. *J Biomech 118(2), 258-261*, 1996.

[73] M. Tapiovaara and T. Siiskonen. Pcxmc a monte carlo program for calculating patient doses in medical x-ray examinations. *STUK-A231*, 2008.

[74] A. Servomaa and M. Tapiovaara. Organ dose calculation in medical x-ray examinations by the program pcxmc. *Radiation Protection Dosimetry 80, 213-219*, 1998.

Appendices

Appendix A

A.1 PCXMC

PCXMC is a computer program for estimating patients' organ doses and the effective dose in medical x-ray examinations. It permits a free adjustment of the x-ray projection and other examination conditions of projection radiography and fluoroscopy. The anatomical data are based on the mathematical hermaphrodite phantom models of Cristy and Eckerman (1987), with some modifications and user-adjustable phantom sizes [73]. The program also estimates the risk of death based on cancers generated from radiation exposure [73] The organ doses are estimated in 29 organs and tissues. The program determines the effective dose with both the new tissue weighting factors of ICRP Publication 103 (2007) and the old tissue weighting factors of ICRP Publication 60 (1991) [74] .

A.2 Using the program

The dose estimation for a new test condition with changes of patient age, patient size or examination geometry from the previously determined cases includes three steps and these steps require (1) defining the examination conditions, (2) performing the Monte Carlo simulation, and (3) calculating the organ doses for a specified x-ray spectrum and patient input dose.

Figure B.1 shows the first graphical user interface where the three buttons on the top row are executed successively from left to right. If the risk is estimated from the calculated doses, the risk assessment button is pressed after the three steps above.

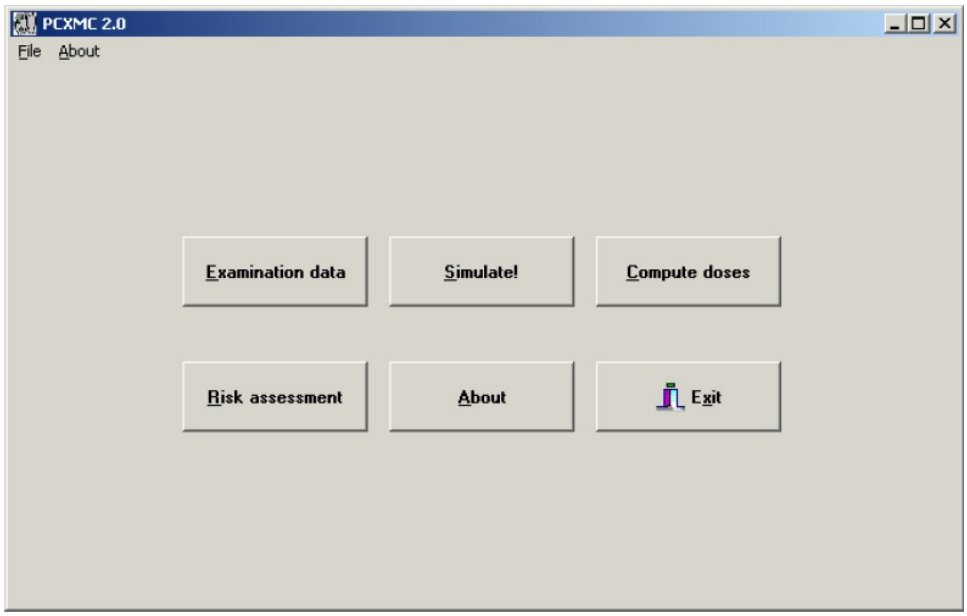

Figure A.1: The main form of PCXMC

If the patient data and the geometric data of the examination are the same from a previous calculation then the first two of the above steps can be discarded, and the patient dose calculation is done by applying the step (3) only. Thus, the user does not need to perform the Monte Carlo simulation again, if just the x-ray spectrum or the amount of radiation have changed.

The program generates files of different extensions that adds automatically in order to keep track of the files. The files that include the examination and patient parameters for Monte Carlo simulation have the extension '.df2', the data files generated by the Monte Carlo estimation have the extension '.en2', and the final dose estimations for specific x-ray spectra and input dose have the extension '.mG2'. Finally, the risk assessment data use the extension '.txt'.

Examination Data Button

By clicking the examination data button it opens a new window (Figure B.2) where the user can define the patients characteristics like the height, weight. The age will be defined by checking the proper button. There are also some standard values for the height and weight according to the age that will be chosen. For the geometric data of the X-ray beam the focus to skin distance (FSD) must be defined as well as the dimensions of the field of view (FOV) and the unit of length is assumed to be cm. The 'Beam width' and 'Beam

height' refer to the lateral and vertical dimensions of the x-ray beam, as measured at the distance FSD from the focal spot of the X-ray tube and in the plane that is vertical to the central axis of the x-ray beam and they do not refer to the x-ray field size at the image receptor. The 'Xref', 'Yref' and 'Zref' are the coordinates of an arbitrary point inside the phantom which is shown on the top right, through which the central axis of the x-ray beam is directed and these data can be used for specifying the location of the x-ray beam with respect to the phantom. The phantom image and the 'radiograph'(located on the bottom right) can be used as a guidance in finding proper coordinates for the reference point.

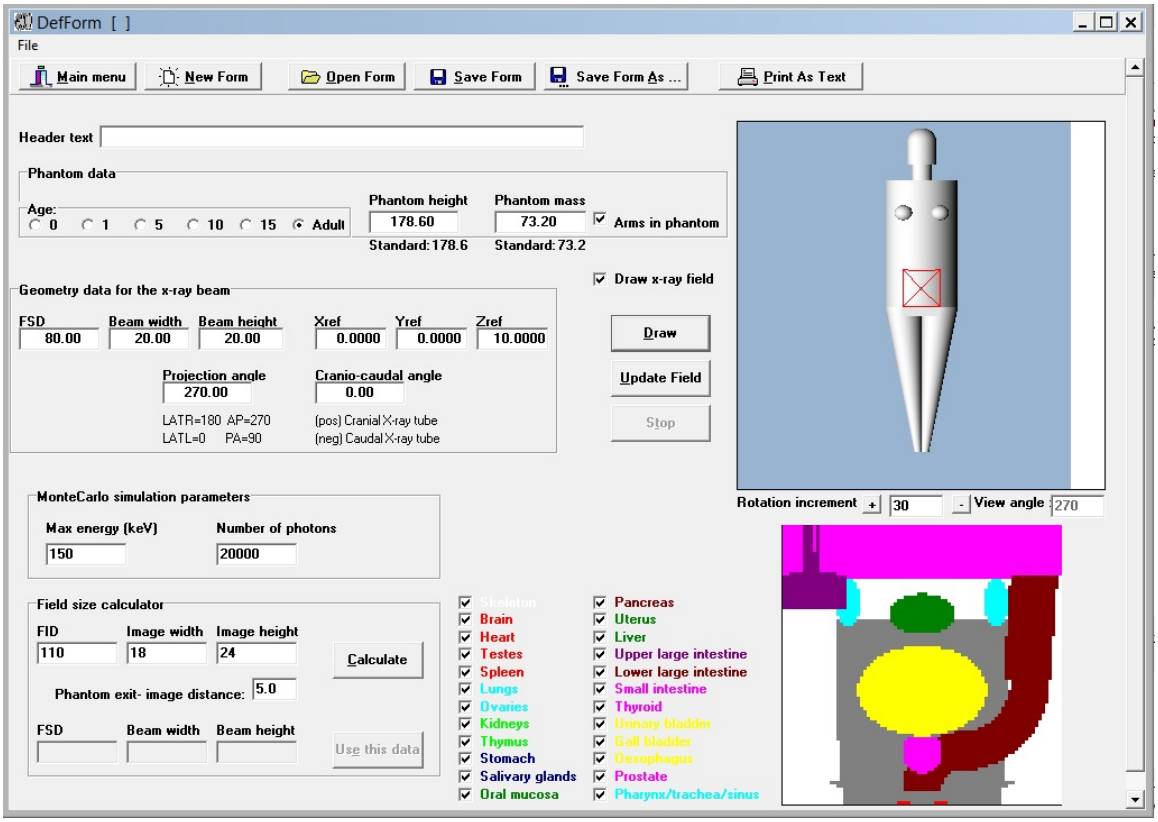

Figure A.2: The X-ray examination input form of PCXMC

The Projection angle and Cranio-caudal angle can define the direction of the X-ray beam regarding with the phantom. For the Monte Carlo simulation parameters the maximum energy shoule be remained at 150 KeV because we do not ant to limit the allowable X-ray tube voltages. The number of photons is an important factor in defining the statistical precision that will be achieved in the Monte Carlo simulation. The minimum value should be 10 000 but in order to improve the accuracy of your doe estimation results the

number of photons should be increased accordingly every time. The 'Draw' button displays the currently specified phantom and examination geometry and when something has been modified then the Draw button should be clicked again. After drawing the phantom image, the program shows also a simulated 'radiograph' which demonstrates the organs in the specified x-ray beam as viewed from the x-ray tube focal spot.

The field size calculator can be used in order to calculate the FSD and the width and height of the x-ray beam at the patient's entrance and when th Use this Data button is being clicked only then these data influence the dose calculations. For using the calculator, the x-ray beam size at the image receptor plane, the distance between the x-ray source and the image intensifier (FID), and the distance between the patient's exit surface and the image intensifier , must be known. Since we always have in mind though to calculate dose based on conservative values always a big FOV should used. After finishing editing the data they can be saved by clicking the 'Save Form' or 'Save Form As' buttons.

Simulate Button

The simulate button opens a new form to perform the Monte Carlo simulation (see Figure B.3). Clicking the 'Open data for Monte Carlo simulation' button you can choose a definition file for the simulation. Several files can be chosen simultaneously by keeping the ¡Ctrl¿ button pressed while choosing definition files. Then the program will simulate these conditions one after another automatically, without the user interfering.

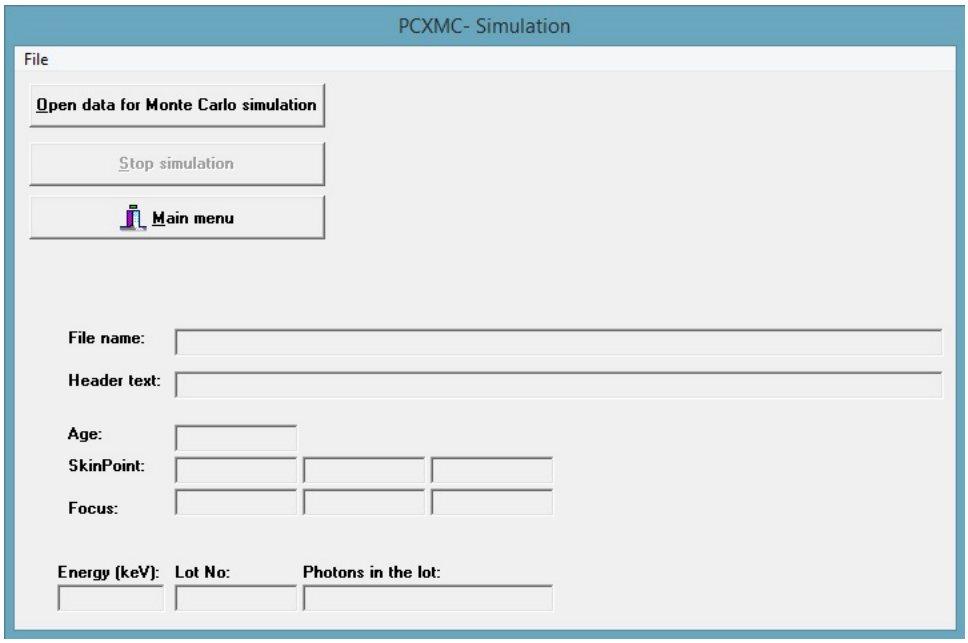

Figure A.3: The Monte Carlo Simulation form

The Energy displays the photon energy during calculation, 'Lot No' displays the number (1 to 10) of the current batch, and 'Photons in the lot' displays the number of photons simulated at the current energy level in the current batch. The outcomes of the simulation are automatically saved with same name used for the definition file of the simulation conditions, but the extension '.df2' is substituted by '.en2'.

Compute Doses Button

Compute Doses button opens a form (see Figure B.4) for estimating the patient's organ doses in an X-ray test. The data for the presently loaded x-ray energy spectrum defined by the x-ray tube voltage (kV), anode angle and total filtration) are displayed on window.

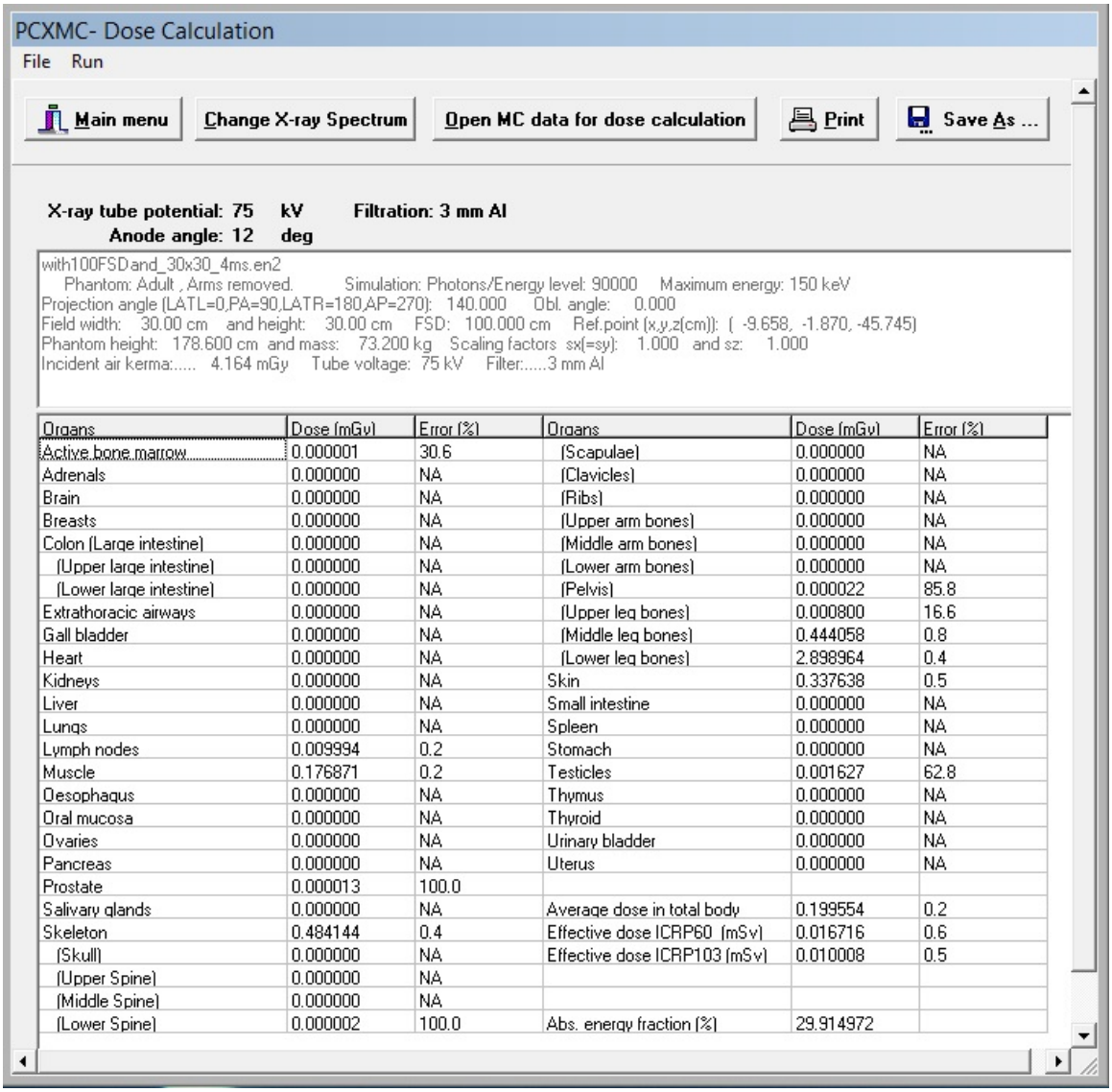

Organs	Dose (mGy)	Error (%)	Organs	Dose (mGy)	Error (%)
Active bone marrow	0.000001	30.6	(Scapulae)	0.000000	NA
Adrenals	0.000000	NA	(Clavicles)	0.000000	NA
Brain	0.000000	NA	(Ribs)	0.000000	NA
Breasts	0.000000	NA	(Upper arm bones)	0.000000	NA
Colon (Large intestine)	0.000000	NA	(Middle arm bones)	0.000000	NA
(Upper large intestine)	0.000000	NA	(Lower arm bones)	0.000000	NA
(Lower large intestine)	0.000000	NA	(Pelvis)	0.000022	85.8
Extrathoracic airways	0.000000	NA	(Upper leg bones)	0.000800	16.6
Gall bladder	0.000000	NA	(Middle leg bones)	0.444058	0.8
Heart	0.000000	NA	(Lower leg bones)	2.898964	0.4
Kidneys	0.000000	NA	Skin	0.337638	0.5
Liver	0.000000	NA	Small intestine	0.000000	NA
Lungs	0.000000	NA	Spleen	0.000000	NA
Lymph nodes	0.009994	0.2	Stomach	0.000000	NA
Muscle	0.176871	0.2	Testicles	0.001627	62.8
Oesophagus	0.000000	NA	Thymus	0.000000	NA
Oral mucosa	0.000000	NA	Thyroid	0.000000	NA
Ovaries	0.000000	NA	Urinary bladder	0.000000	NA
Pancreas	0.000000	NA	Uterus	0.000000	NA
Prostate	0.000013	100.0			
Salivary glands	0.000000	NA	Average dose in total body	0.199554	0.2
Skeleton	0.484144	0.4	Effective dose ICRP60 (mSv)	0.016716	0.6
(Skull)	0.000000	NA	Effective dose ICRP103 (mSv)	0.010008	0.5
(Upper Spine)	0.000000	NA			
(Middle Spine)	0.000000	NA			
(Lower Spine)	0.000002	100.0	Abs. energy fraction (%)	29.914972	

Figure A.4: The dose calculation form. Before a file has been opened the table is empty

In order to change the spectrum accordingly for each test every time the user must click on the 'Change X-ray Spectrum' button and determine the x-ray tube voltage, target angle, and total filtration in the form that appears (Figure B.5). For the HSSR system the X-ray tube Anode angle is going to be 12 ^{0} and for filtering the AI 13 material with 3.00 mm thickness will be entered. After all the parameters are specified then someone can exit by pressing either Exit:generate this spectrum or Exit: Keep old spectrum.

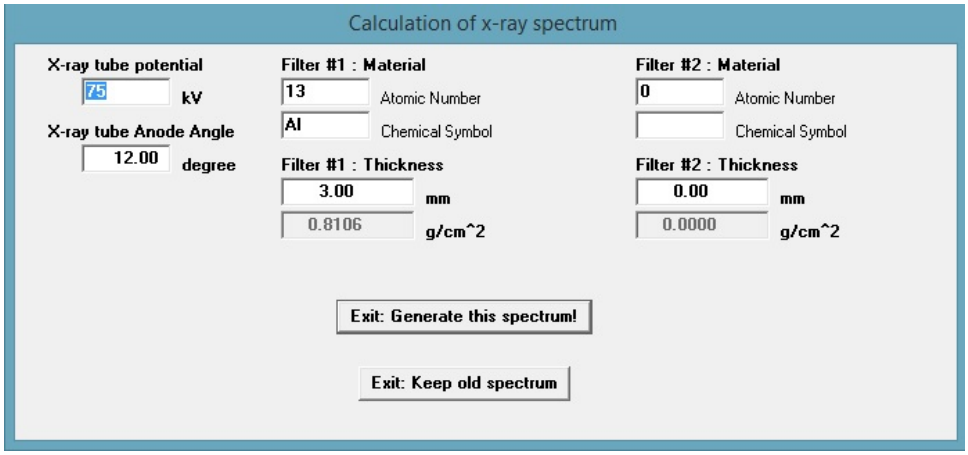

Figure A.5: Calculation of th X-ray spectrum form of PCXMC

Clicking the 'Open MC data for dose calculation' button asks to select an .en2 file which already has been calculated from previous steps and choose the file you wish to estimate results for and open it. A new window will appear (see Figure B.6) and then you will need to specify the input dose. In our case the x-ray tube current-time product (mAs) will be used. Then the input dose quantity is being converted to incident air kerma in milligrays.

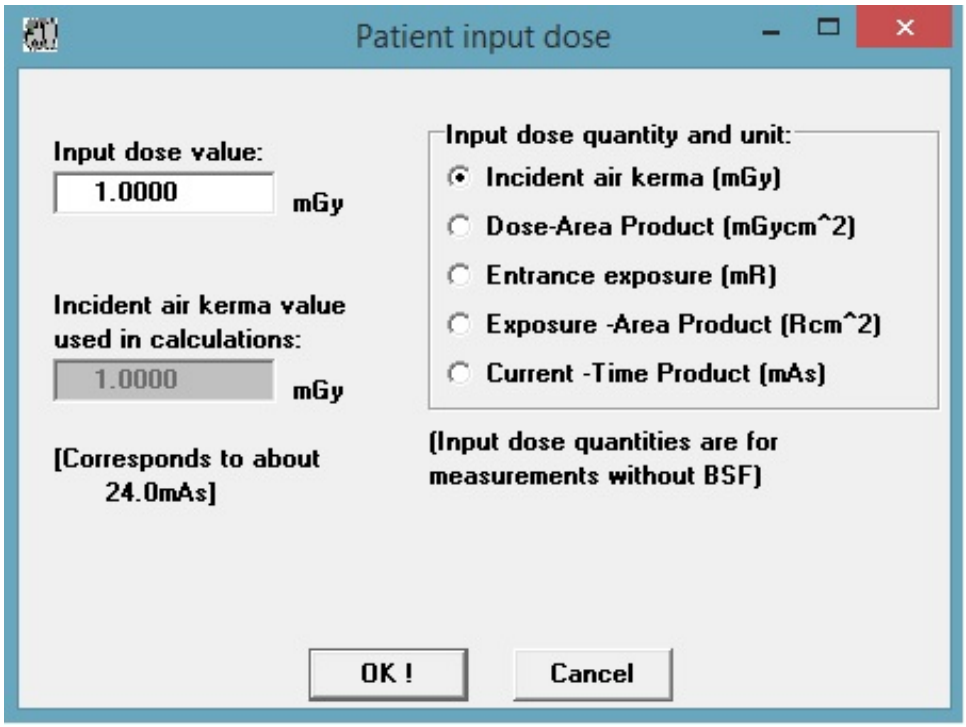

Figure A.6: The patient input dose specification form of PCXMC

Then the estimated organ doses and other dose quantities are shown (in milligray, or equivalently, in millisievert) as well as their estimated statistical precision. If the user does not like the statistical precision results, the Monte Carlo simulation should be repeated with a higher number of photons (greater value of 'Number of photons' in the Examination data form). For saving the data press the 'Save as' button and then you can exit by pressing the main menu button in order to continue to the next step for calculating the Risk Assessment if you wish.

Risk Assessment Button

This button opens a form (see Figure B.7) for obtaining the risk of radiation-induced cancer death. PCXMC also informs the user whether high doses are found that may cause deterministic health effects.

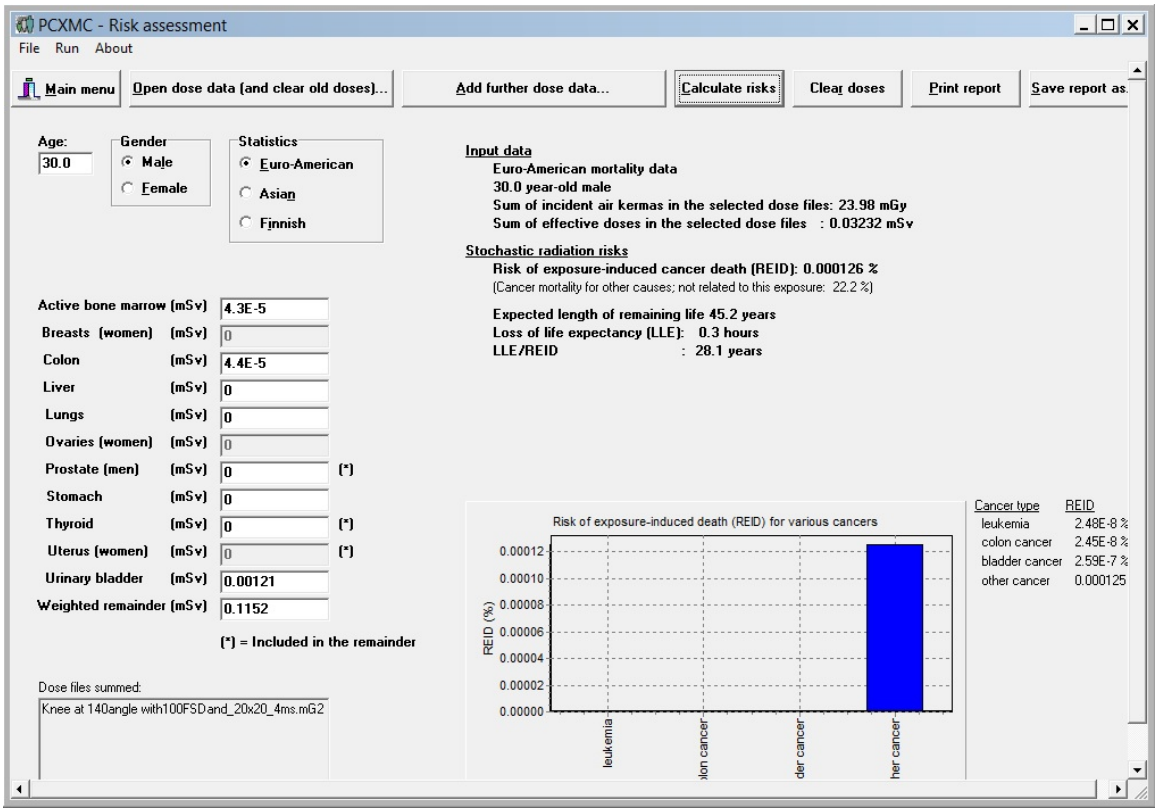

Figure A.7: The risk assessment form of PCXMC. WHen it is firstly open the form shows data of 30 yeal old European with no radiation exposure

For that step the user needs to enter correct patient data for the age, gender and mortality

statistics (Euro-American, Asian or Finnish). These data can be manually entered or to obtain them from previously calculated dose files (.mG2). If the equivalent doses have been acquired from dose files (.mG2) estimated with PCXMC, then the program takes care of the proper value of the weighted remainder dose. You can chose the already estimated equivalent doses by clicking the 'Open dose data (and clear old doses)' button. If some of the estimated doses are really high (more than 10 Sv), the corresponding fields will become yellow, and if the dose has too great value for a successful estimation, the color of the field is red. After defining all the input data the risk assessment will be calculated by clicking on the 'Calculate Risks' button. A yellow warning label 'Risk data have not been updated: Click 'Calculate risks' on the window shows that input data have been edited, and do not anymore match with the risk data shown on the form. The data are up to date and this warning label will disappear when the user presses the 'Calculate risks' button or that label. The risk calculation defines the person's risk of exposure induced cancer death (REID), the expected length of his/her remaining life, the mean loss-of-life (LL E) and the mean loss of life in case that the radiation induced cancer is realized (LL E/REID). This form also demonstrates a bar chart of the probability (the site-specific REID value) of several cancer types generated from radiation exposure.

A.2.1 Dose estimations for HSSR projects

Knee

	Subjects	Pulse Width (ms)	Field of View (FOV) (cm)	Height (cm)	Mass (kg)	Acc. Voltage (kVp)	Tube Current (mA)	Time (s)	Current-Time product (mAs)	# frames	FSD (cm)	Angle (deg, i=interbeam)	Total Effective Dose (mSv)
PCMXC-Dose Estimates for Healthy Knees by using Pulsed radiographic mode	KS01	1	40x40	150	57	60	63	2 sec	6.3	50	100	150 210	0.0012
		0.5						1 sec	3.15	100		150 210	0.0006
		0.5						1 sec	3.15	100		150 210	0.0006
		1						2 sec	6.3	50		150 210	0.0012
		0.75						1 sec	2.36	50		150 210	0.00045
												Total	0.00405

Figure A.8: Dose Estimates for KS01 healthy knee subject

	Subjects	Pulse Width (ms)	Field of View (FOV) (cm)	Height (cm)	Mass (kg)	Acc. Voltage (kVp)	Tube Current (mA)	Time (s)	Current-Time product (mAs)	# frames	FSD (cm)	Angle (deg, i=interbeam)	Total Effective Dose (mSv)
PCMXC-Dose Estimates for Healthy Knees by using Pulsed radiographic mode	KS02	0.75	40x40	163	66	60	63	4 sec	9.45	50	100	150 210	0.00168
								1 sec	4.725	100		150 210	0.00084
								2 sec	9.45	100		150 210	0.0017
								2 sec	4.725	50		150 210	0.00084
								1 sec	4.725	100		150 210	0.00084
								2 sec	9.45	100		150 210	0.0017
								2 sec	9.45	100		150 210	0.0017
												Total	0.0093

Figure A.9: Dose Estimates for KS02 healthy knee subject

	Subjects	Pulse Width (ms)	Field of View (FOV) (cm)	Height (cm)	Mass (kg)	Acc. Voltage (kVp)	Tube Current (mA)	Time (s)	Current-Time product (mAs)	# frames	FSD (cm)	Angle (deg, i=interbeam)	Total Effective Dose (mSv)
PCMXC-Dose Estimates for Healthy Knees by using Pulsed radiographic mode	KS03	0.75	40x40	174	75	60	63	3 sec	7.088	50	100	150 210	0.0012
								1 sec	4.725	100		150 210	0.00081
								1 sec	4.725	100		150 210	0.00081
								2 sec	4.726	50		150 210	0.00081
								1 sec	4.725	100		150 210	0.00081
								3 sec	7.088	50		150 210	0.0012
								3 sec	7.088	50		150 210	0.0012
												Total	0.007

Figure A.10: Dose Estimates for KS03 healthy knee subject

	Field of View (FOV) (cm)	Height (cm)	Mass (kg)	Acc. Voltage (kVp)	Tube Current (mA)	Time (s)	Current-Time product (mAs)	# frames	FSD (cm)	Angle (deg, i=interbeam)	Effective dose (mSv)	Total Effective Dose (mSv)
PCMXC- Dose Estimates for the knee by using Pulsed radiographic mode for 1ms of exposure	20x20	178.6	73.2	90	100	10 sec	100	100	100	140	0.00807	**0.01683**
										200	0.00876	
	25x25	178.6	73.2	90	100	10 sec	100	100	100	140	0.0124	**0.02333**
										200	0.0109	
	28x28	178.6	73.2	90	100	10 sec	100	100	100	140	0.0147	**0.02689**
										200	0.01219	
	30x30	178.6	73.2	90	100	10 sec	100	100	100	140	0.0162	**0.02937**
										200	0.01317	

Figure A.11: Knee Dose Estimates by using pulsed radiographic mode for 1 ms of exposure

	Field of View (FOV) (cm)	Height (cm)	Mass (kg)	Acc. Voltage (kVp)	Tube Current (mA)	Time (s)	Current-Time product (mAs)	# frames	FSD (cm)	Angle (deg, i=interbeam)	Effective dose (mSv)	Total Effective Dose (mSv)
PCMXC- Dose Estimates for the knee by using Pulsed radiographic mode for 4ms of exposure	20x20	178.6	73.2	90	100	10 sec	400	100	100	140	0.0323	**0.0673**
										200	0.03504	
	25x25	178.6	73.2	90	100	10 sec	400	100	100	140	0.0496	**0.0932**
										200	0.0436	
	28x28	178.6	73.2	90	100	10 sec	400	100	100	140	0.0589	**0.1076**
										200	0.0487	
	30x30	178.6	73.2	90	100	10 sec	400	100	100	140	0.0649	**0.1176**
										200	0.0527	

Figure A.12: Knee Dose Estimates by using pulsed radiographic mode for 4 ms of exposure

Hip

	Pulse Width (ms)	Field of View (FOV) (cm)	Height (cm)	Mass (kg)	Acc. Voltage (kVp)	Tube Current (mA)	Time (s)	Current-Time product (mAs)	# frames	FSD (cm)	Angle (deg, i=interbeam)	Effective dose (mSv)	Total Effective Dose (mSv)
PCMXC- Dose Estimates for the Hip by using Pulsed radiographic mode for 1ms of exposure	1ms	40x40	178.6	73.2	60	80	1sec	2.4	30	80	150	0.0014	**0.005**
											210	0.0036	
			178.6	73.2	60	80	10sec	24		80	150	0.0145	**0.0505**
											210	0.036	
			178.6	73.2	60	80	1sec	4	50	80	150	0.0024	**0.0084**
											210	0.006	
			178.6	73.2	60	80	10sec	40		80	150	0.024	**0.084**
											210	0.06	

Figure A.13: Dose estimates for hip by using pulsed radiographic mode for 1 ms of exposure

	Pulse Width (ms)	Field of View (FOV) (cm)	Height (cm)	Mass (kg)	Acc. Voltage (kVp)	Tube Current (mA)	Time (s)	Current-Time product (mAs)	# frames	FSD (cm)	Angle (deg, i=interbeam)	Effective dose (mSv)	Total Effective Dose (mSv)
PCMXC- Dose Estimates for the Hip by using Pulsed radiographic mode for 5ms of exposure	5ms	28x28	178.6	73.2	60	80	1sec	12	30	80	150	0.004	0.023
											210	0.019	
			178.6	73.2	60	80	10sec	120		80	150	0.04	0.234
											210	0.194	
			178.6	73.2	60	80	1sec	40	100	80	150	0.013	0.073
											210	0.06	
			178.6	73.2	60	80	10sec	400		80	150	0.13	0.78
											210	0.65	

Figure A.14: Dose estimates for hip by using pulsed radiographic mode for 5 ms of exposure

	Pulse Width (ms)	Field of View (FOV) (cm)	Height (cm)	Mass (kg)	Acc. Voltage (kVp)	Tube Current (mA)	Time (s)	Current-Time product (mAs)	# frames	FSD (cm)	Angle (deg, i=interbeam)	Effective dose (mSv)	Total Effective Dose (mSv)
PCMXC- Dose Estimates for the Hip by using Pulsed radiographic mode for 0.4ms/1ms of exposure	0.4ms	40x40	178.6	73.2	100	50	1sec	2	100	80	150	0.008	0.023
											210	0.015	
			178.6	73.2	100	50	10sec	20		80	150	0.081	0.237
											210	0.156	
	1ms		178.6	73.2	60	40	1sec	4		80	150	0.002	0.008
											210	0.006	
			178.6	73.2	60	40	10sec	40		80	150	0.024	0.084
											210	0.06	

Figure A.15: Dose estimates for hip by using pulsed radiographic mode for 1/0.4 ms of exposure and for 100 f/sec

	Pulse Width (ms)	Field of View (FOV) (cm)	Height (cm)	Mass (kg)	Acc. Voltage (kVp)	Tube Current (mA)	Time (s)	Current-Time product (mAs)	# frames	FSD (cm)	Angle (deg, i=interbeam)	Effective dose (mSv)	Total Effective Dose (mSv)
PCMXC- Dose Estimates for the Hip by using Pulsed radiographic mode	1	40x40	163	113.4	115	125	1sec	3	24	100	150	0.0085	0.0255
											210	0.017	
	1.25		163	113.4	120	125		3.75			150	0.012	0.036
											210	0.024	
	1		163	113.4	80	80		1.92			150	0.0015	0.005
											210	0.0035	
	2		163	113.4	115	125		6			150	0.017	0.051
											210	0.034	
	4		163	113.4	115	125		12			150	0.034	0.103
											210	0.069	
	3		163	113.4	100	100		7.2			150	0.013	0.04
											210	0.027	
	2		163	113.4	115	100		4.8			150	0.014	0.042
											210	0.028	
	5		163	113.4	115	100		12			150	0.034	0.103
											210	0.069	

Figure A.16: Dose estimates for hip by using pulsed radiographic mode for different pulsed widths

	Pulse Width (ms)	Field of View (FOV) (cm)	Height (cm)	Mass (kg)	Acc. Voltage (kVp)	Tube Current (mA)	Time (s)	Current-Time product (mAs)	# frames	FSD (cm)	Angle (deg, i=interbeam)	Effective dose (mSv)	Total Effective Dose (mSv)
PCMXC- Dose Estimates for Cadaver Hip by using Pulsed radiographic mode	1ms	40x40	178.6	73.2	90/95	125	1 sec	3	24	80	210	0.023	0.033
											140	0.01	
	2ms		178.6	73.2	70/80	125		6			210	0.028	0.037
											140	0.009	
			178.6	73.2	65/80	160		7.68			210	0.035	0.118
											140	0.083	
	1ms		178.6	73.2	90/95	125		6.25	50		210	0.049	0.072
											140	0.023	
	2ms		178.6	73.2	70/80	125		12.5			210	0.06	0.078
											140	0.018	
			178.6	73.2	65/80	160		16			210	0.074	0.091
											140	0.017	

Figure A.17: Dose estimates for Cadaver hip by using pulsed radiographic mode

Shoulder

	Pulse Width (ms)	Field of View (FOV) (cm)	Height (cm)	Mass (kg)	Acc. Voltage (kVp)	Tube Current (mA)	Time (s)	Current-Time product (mAs)	# frames	FSD (cm)	Angle (deg, i=interbeam)	Effective dose (mSv)	Total Effective Dose (mSv)
PCMXC- Dose Estimates for the Shoulder by using Pulsed radiographic mode for 4ms of exposure (Shoulder Arthroplasty Fluoro IRB Narrative, VAIL)	4ms	20x20	178.6	73.2	65	13	10 sec	15.6	30	100	230	0.019	0.025
											290	0.006	
		25x25	178.6	73.2	65	13	10 sec	15.6		100	230	0.038	0.054
											290	0.016	
		20x20	178.6	73.2	65	13	10 sec	52	100	100	230	0.063	0.083
											290	0.02	
		25x25	178.6	73.2	65	13	10 sec	52		100	230	0.126	0.18
											290	0.054	
In the IRB document in VAIL they used 65 KV, 13 mA, for 10sec and 30 fps (FSD and pulse width are unknown)													
PCMXC- Dose Estimates for the Shoulder by using Pulsed radiographic mode for 8ms of exposure (Shoulder Arthroplasty Fluoro IRB Narrative,VAIL)	Pulse Width (ms)	Field of View (FOV) (cm)	Height (cm)	Mass (kg)	Acc. Voltage (kVp)	Tube Current (mA)	Time (s)	Current-Time product (mAs)	# frames	FSD (cm)	Angle (deg, i=interbeam)	Effective dose (mSv)	Total Effective Dose (mSv)
	8ms	20x20	178.6	73.2	65	13	10 sec	31.2	30	100	230	0.038	0.05
											290	0.012	
		25x25	178.6	73.2	65	13	10 sec	31.2		100	230	0.075	0.107
											290	0.032	
		20x20	178.6	73.2	65	13	10 sec	104	100	100	230	0.126	0.167
											290	0.041	
		25x25	178.6	73.2	65	13	10 sec	104		100	230	0.252	0.36
											290	0.108	

Figure A.18: Dose estimates for Shoulder by using pulsed radiographic mode

	Pulse Width (ms)	Field of View (FOV) (cm)	Height (cm)	Mass (kg)	Acc. Voltage (kVp)	Tube Current (mA)	Time (s)	Current-Time product (mAs)	# frames	FSD (cm)	Angle (deg, i=interbeam)	Effective dose (mSv)	Total Effective Dose (mSv)
PCMXC- Dose Estimates for Cadaver Shoulder by using Pulsed radiographic mode	1.5ms	35x35	178.6	73.2	75	100	1 sec	4.5	30	100	230	0.12	**0.223**
											290	0.103	
			178.6	73.2	70/75	125/160		5.65/7.2			230	0.04	**0.09**
											290	0.05	
			178.6	73.2	80/85	200/250		9/11.25			230	0.08	**0.189**
											290	0.109	
			178.6	73.2	75	100		15	100		230	0.035	**0.066**
											290	0.031	
			178.6	73.2	70/75	125/160		18.75/24			230	0.12	**0.286**
											290	0.166	
			178.6	73.2	80/85	200/250		30/37.5			230	0.3	**0.59**
											290	0.29	

Figure A.19: Dose estimates for Cadaver Shoulder by using pulsed radiographic mode

Foot

	Pulse Width (ms)	Field of View (FOV) (cm)	Height (cm)	Mass (kg)	Acc. Voltage (kVp)	Tube Current (mA)	Time (s)	Current-Time product (mAs)	# frames	FSD (cm)	Angle (deg, i=interbeam)	Effective dose (mSv)	Total Effective Dose (mSv)
PCMXC- Dose Estimates for the Foot by using Pulsed radiographic mode for 5ms of exposure	5ms	25x25	178.6	73.2	60	80	5 sec	200	100	80	130	0.005	**0.009**
											190	0.004	
			178.6	73.2	60	80	7 sec	280		80	130	0.0076	**0.0126**
											190	0.005	
			178.6	73.2	60	80	10 sec	400		80	130	0.0156	**0.0256**
											190	0.01	

Figure A.20: Dose estimates for Foot by using pulsed radiographic mode for 5 ms of exposure

Pelvis

	Pulse Width (ms)	Field of View (FOV) (cm)	Height (cm)	Mass (kg)	Acc. Voltage (kVp)	Tube Current (mA)	Time (s)	Current-Time product (mAs)	# frames	FSD (cm)	Angle (deg, i=interbeam)	Effective dose (mSv)	Total Effective Dose (mSv)
PCMXC- Dose Estimates for the Pelvis Area by using Pulsed radiographic mode for 5ms of exposure	5ms	28x28	178.6	73.2	60	80	1 sec	40	100	80	230	0.105	**0.235**
											290	0.13	
			178.6	73.2	60	80	2 sec	80		80	230	0.211	**0.471**
											290	0.26	
			178.6	73.2	60	80	1 sec	12	30	80	230	0.032	**0.07**
											290	0.038	
			178.6	73.2	60	80	2 sec	24		80	230	0.064	**0.142**
											290	0.078	
			178.6	73.2	60	80	1 sec	12		80	220	0.024	**0.061**
											280	0.037	
			178.6	73.2	60	80	2 sec	24		80	220	0.049	**0.124**
											280	0.075	
			178.6	73.2	60	80	5 sec	60		80	220	0.124	**0.311**
											280	0.187	

Figure A.21: Dose estimates for Pelvis by using pulsed radiographic mode for 5 ms of exposure

Torso

	Pulse Width (ms)	Field of View (FOV) (cm)	Height (cm)	Mass (kg)	Acc. Voltage (kVp)	Tube Current (mA)	Time (s)	Current-Time product (mAs)	# frames	FSD (cm)	Angle (deg, i=interbeam)	Effective dose (mSv)	Total Effective Dose (mSv)
PCMXC- Dose Estimates for the Torso by using Pulsed radiographic mode for 5ms of exposure	5ms	28x28	178.6	73.2	60	80	2 sec	24	30	80	230	0.16	**0.34**
											290	0.18	
			178.6	73.2	60	80		24		80	270	0.19	**0.33**
											210	0.14	
			178.6	73.2	60	80		24		80	320	0.16	**0.34**
											260	0.18	
			178.6	73.2	60	13		3.9		80	230	0.026	**0.055**
											290	0.029	
			178.6	73.2	60	80		80	100	80	230	0.54	**1.15**
											290	0.61	

Figure A.22: Dose estimates for Torso by using pulsed radiographic mode for 5 ms of exposure

Appendix B

B.1 2D-3D matching process

Autoscoper software is used for estimating the 3D position and orientation (pose) of the human joint that we are interested in. The software allows the user to rotate and translate the 3D CT volume in order to perform 2D-3D matching for determining the tracking throughout the range of motion. After the shape matching is completed the transformation matrices, between the origin of the system which is defined from the calibration cube and the coordinate system of the 3D bone model (as defined from the CT) ,are acquired for estimating the 3D joint kinematics.

B.1.1 Autoscoper Tracking Tutorial

Step 1. Create a new Trial in Autoscoper

To create a new trial manually, open up a text editor, like an notepad. For each camera in the file enter the text below substituting the text with the correct specifications. VolumeFlip allows you to flip the axes of your bone model. 1 means flip and 0 means do not flip. x and y correspond to the axis within a single image slice, and z corresponds to the axis across the slices (Default is 0 0 0 meaning no flip and use the default setting. YOU DO NOT FLIP!).

Camera 1 mayaCam_csv complete path including file name to mayacam file for camera 1 CameraRootDir complete path to undistorted video frames for camera 1

Camera 2 mayaCam_csv complete path including file name to mayacam file for camera 2 CameraRootDir complete path to undistorted video frames for camera 2

VolumeFile complete path including file name to tif file containing bone volume VoxelSize in plane x in mm in plane y in mm slice thickness in mm VolumeFlip x y z

After you entered all of the information required, save the text file. Use File/Open menu

command to open and work with this trial in Autoscoper. An example of a configuration file is illustrated in the Figure B.1 below.

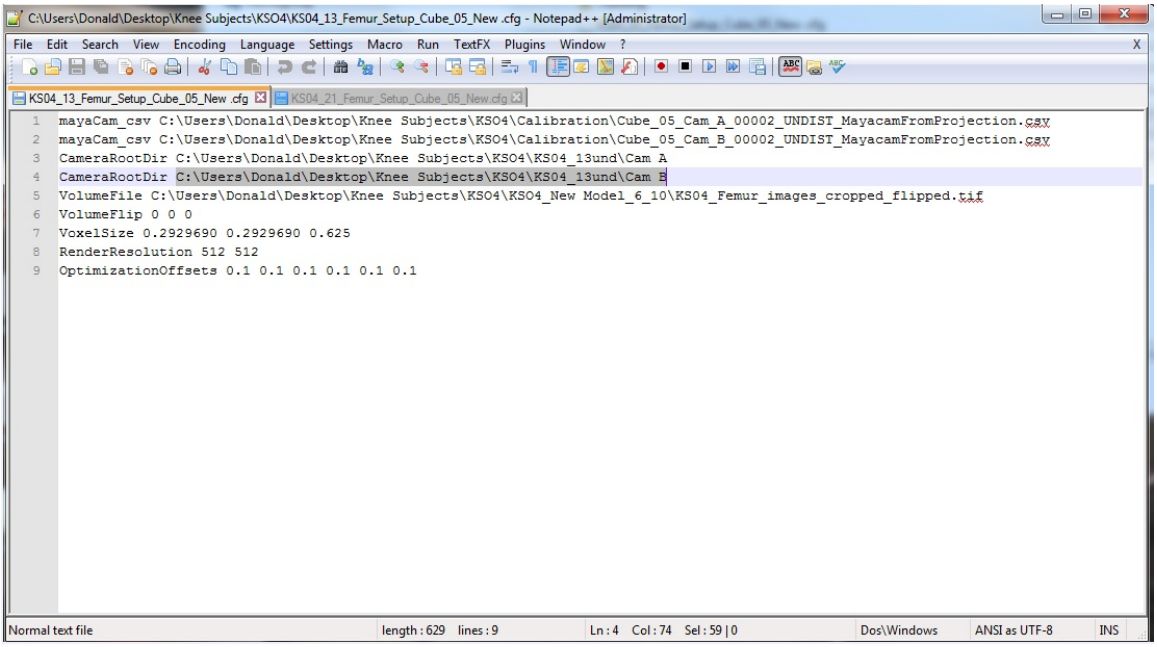

Figure B.1: An example of a configuration file

Step 2. Update file paths in .cfg file

Step 3. Load.cfg file via [Open Trial] and you will see the new created tracking project (Figure B.2

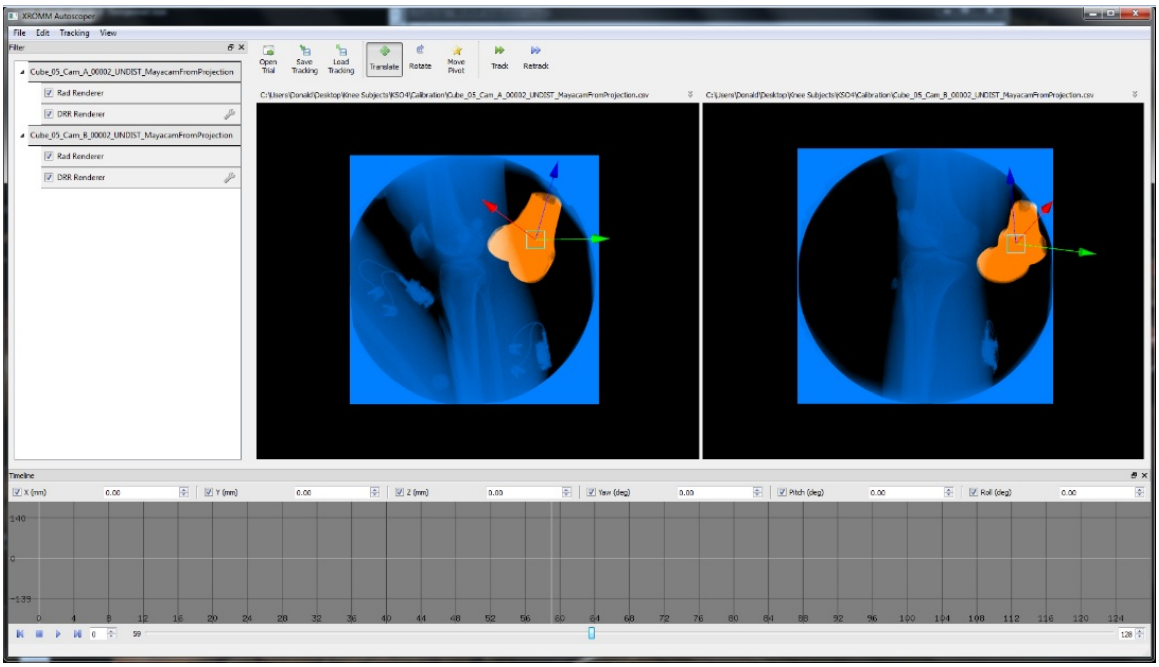

Figure B.2: When the configuration file is loaded in Autoscoper

Step 4. Apply or load saved filters

In order to add a filter, right click on either DRRender or RadRender under a particular view and select the filters you want to utilize (Sobel, Contrast, Gaussian and Sharpen filter). Adjust the numbers in the filters until you are satisfied with the result. You can adjust the values for the filters by pressing the small icon which looks like a wrench (see Figure B.3). The sobel filter allows for control of edge detection and the Contrast filter changes object/image contrast. The DRRRender is the 3D bone model being tracked. The RadRender is the X-ray video that you are tracking on. Apply the filters that you want for each DrrRenderand RadRender for each camera.

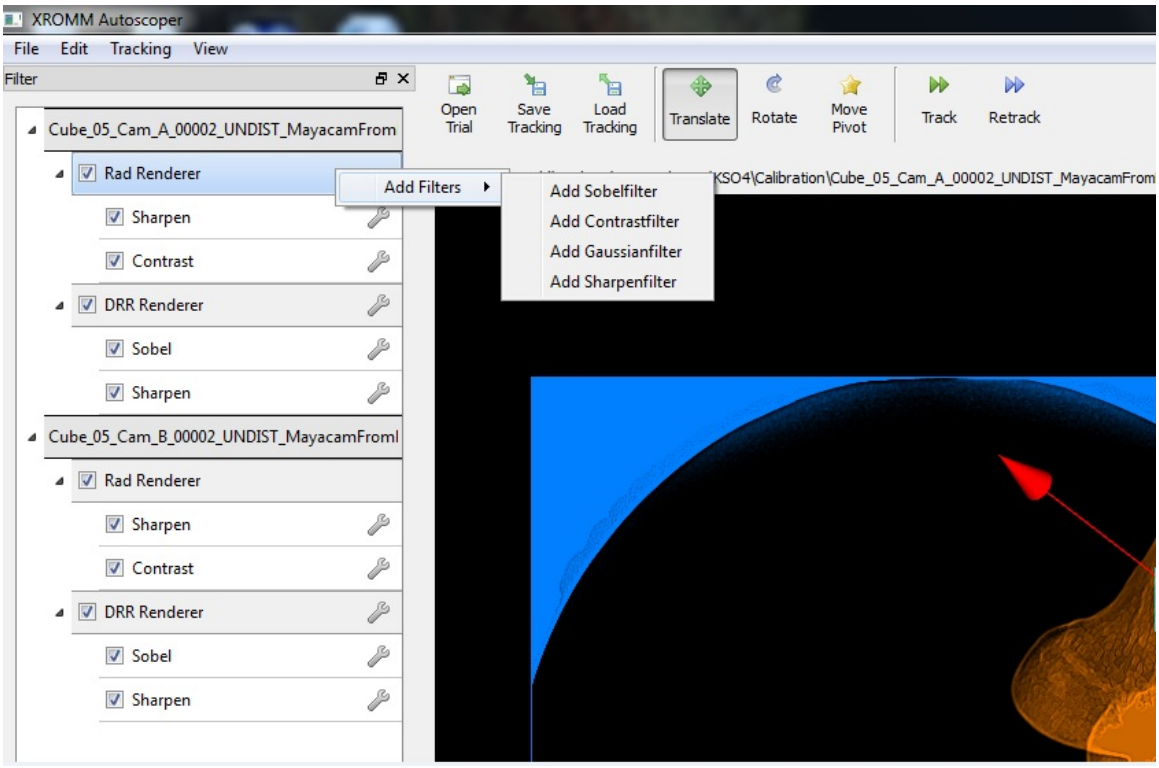

Figure B.3: Illustration of how to add filters in Autoscoper

(** For the DRRRender you have an extra choice, to change the sample distance , the X-ray intensity and the X-ray cut off. Changing the sample distance will affect processing and redraw times (Figure B.4).)

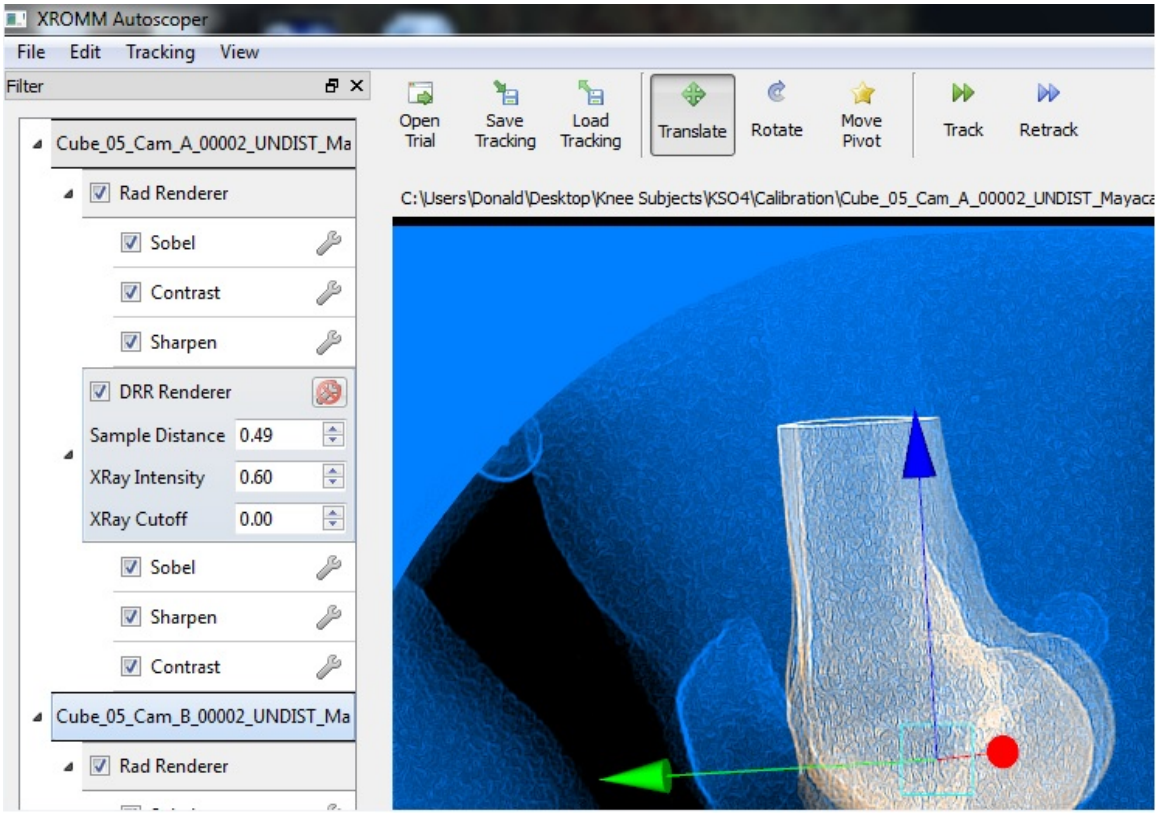

Figure B.4: Options for the DRRender in Autoscoper

Load saved filters:

Right click on View 1 with correspondence name and choose Load settings. Do the same for view 2. For saving instead of Load Settings choose Save Settings (Figure B.5).

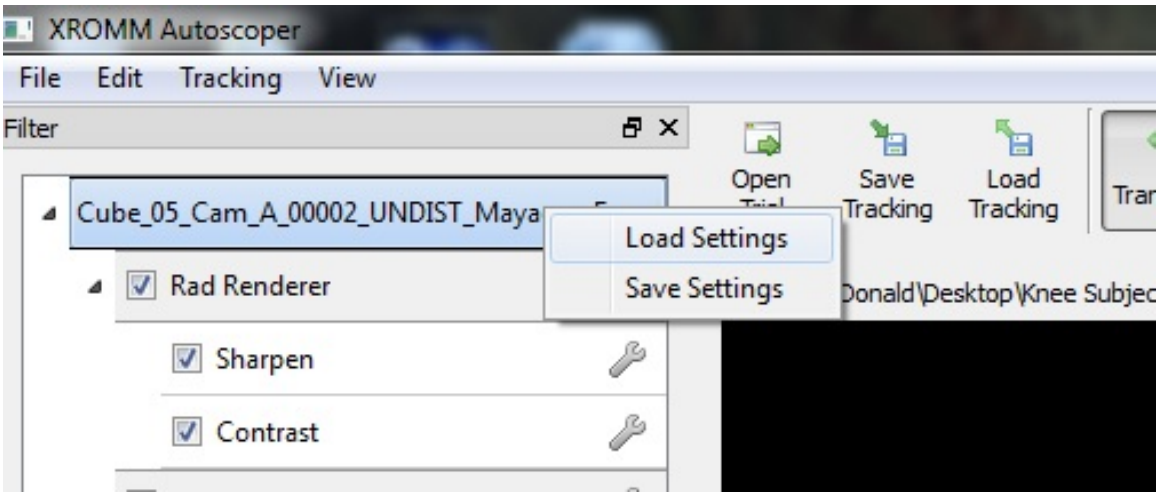

Figure B.5: Load or Save filters in Autoscoper

The Trial with filters applied and is demonstrated on (Figure B.6).

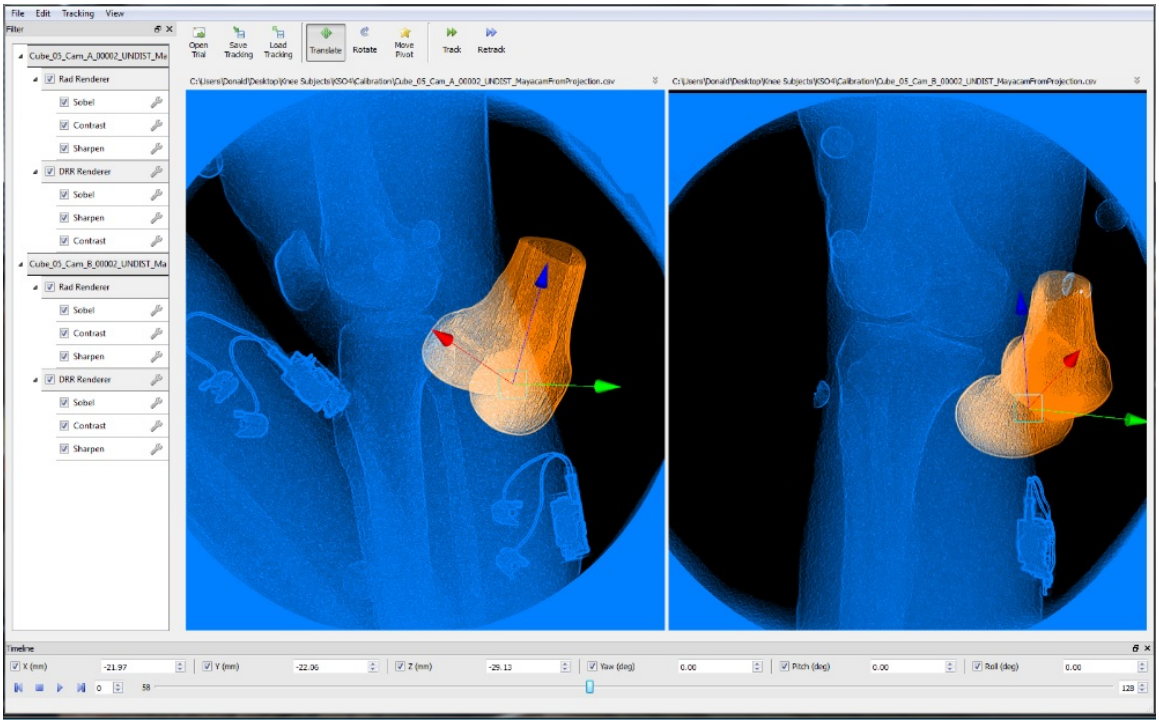

Figure B.6: Demonstration of the knee joint in Autoscoper when the filters are applied

Step 5. 3D view

To see the 3-D view, press on the View button and choose the 'see World view' (Figure B.7).

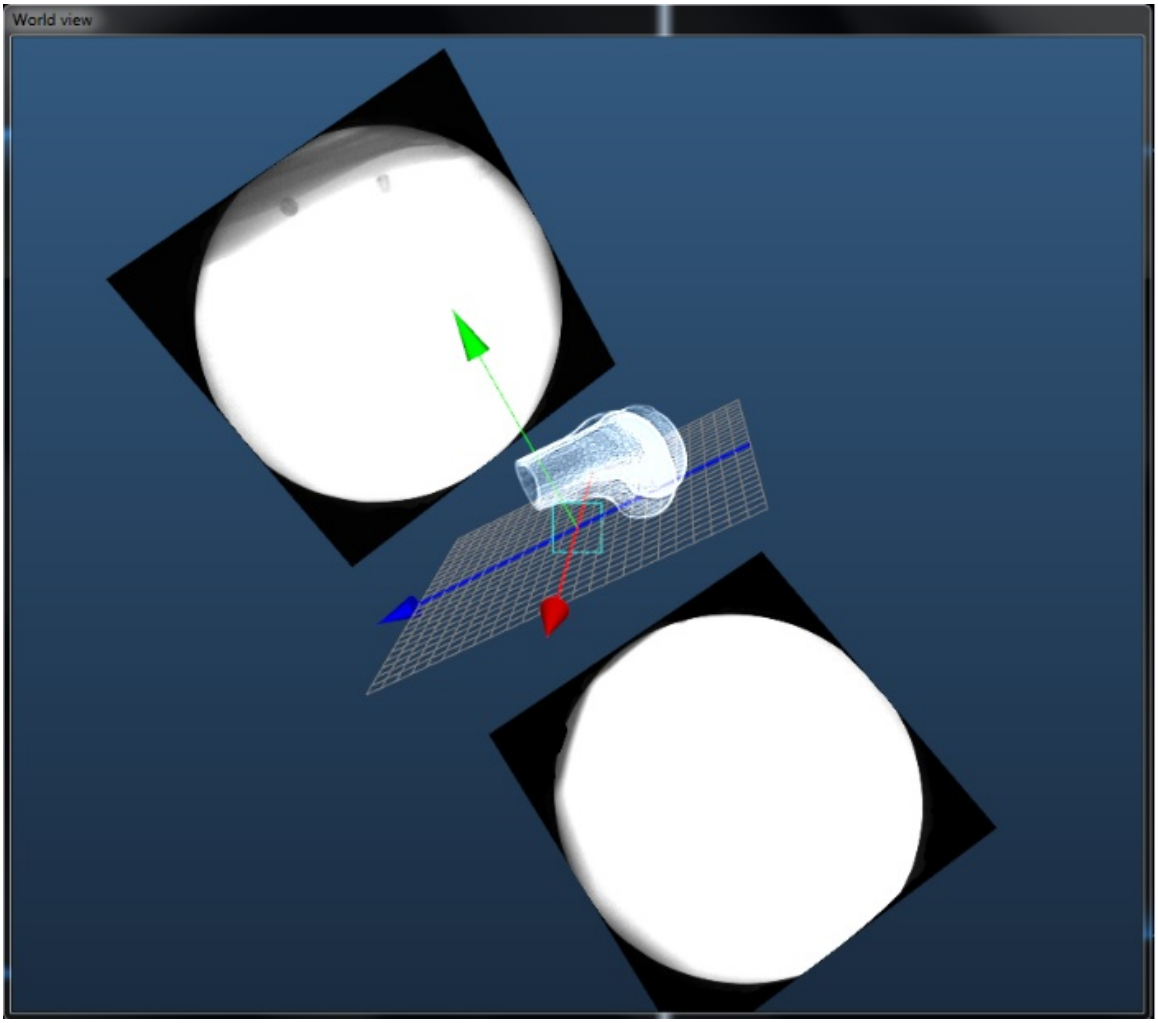

Figure B.7: World view in Autoscoper

It is significant to move the tracking pivot to the center of the bone model (e.g. knee joint center) and in order to do that select 'MovePivot' . When it is centered, click the 'Move Pivot' button again to set the pivot and you can unclick the 'see World view' for now (Figure B.8).

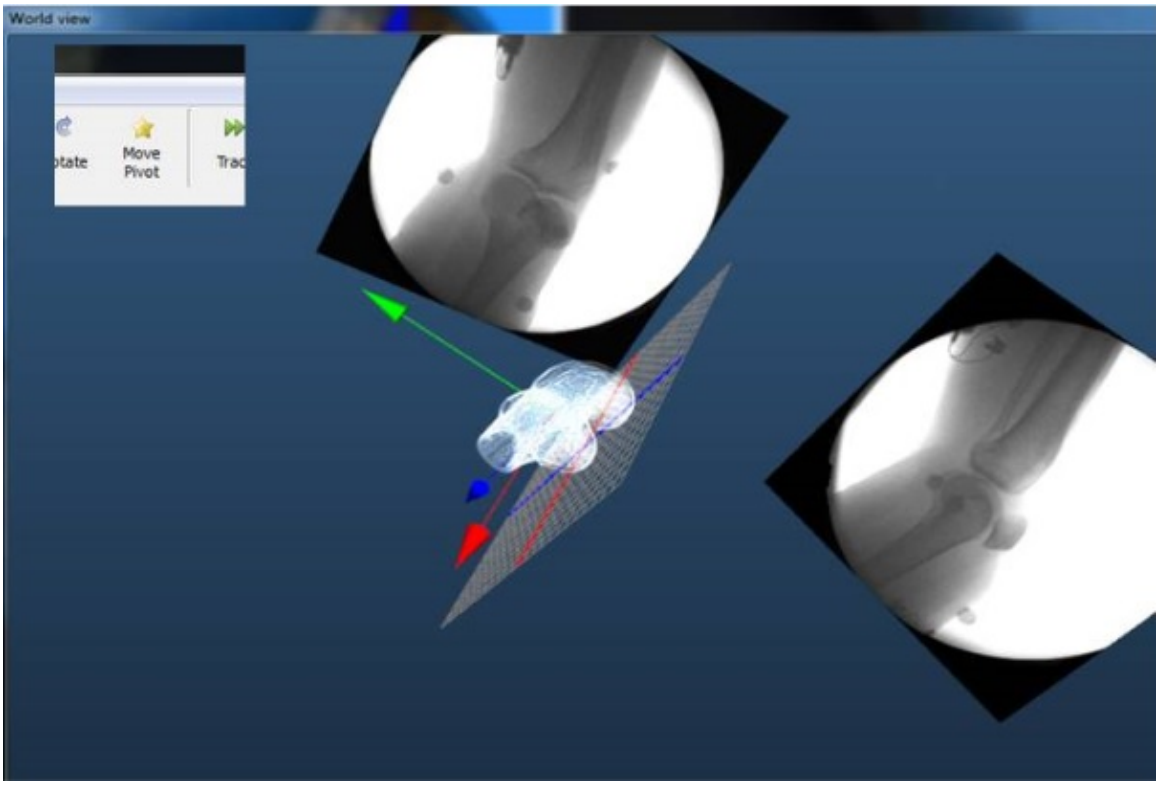

Figure B.8: Demonstration of positioning the pivot in the center of the femoral component using the World view

Step 6. Bone Tracking in Autoscoper

By selecting the pivot center or one of the directional arrows, drag the bone render to the approximate location on the RadRender. It may be also important to Rotate the model by clicking on the ”Rotate” button and do the same. Use ’Translate’ and ’Rotate’ buttons to align the 3D model to 2D images until good alignment is achieved (Figure B.9) (to translate, click and drag the arrows, to rotate click and drag the circles). It is often helpful to alternate adjustments between planes. When you are done with your alignment save that position by clicking the S button on your clipboard (Always remember to save your alignment by pressing S for each frame).

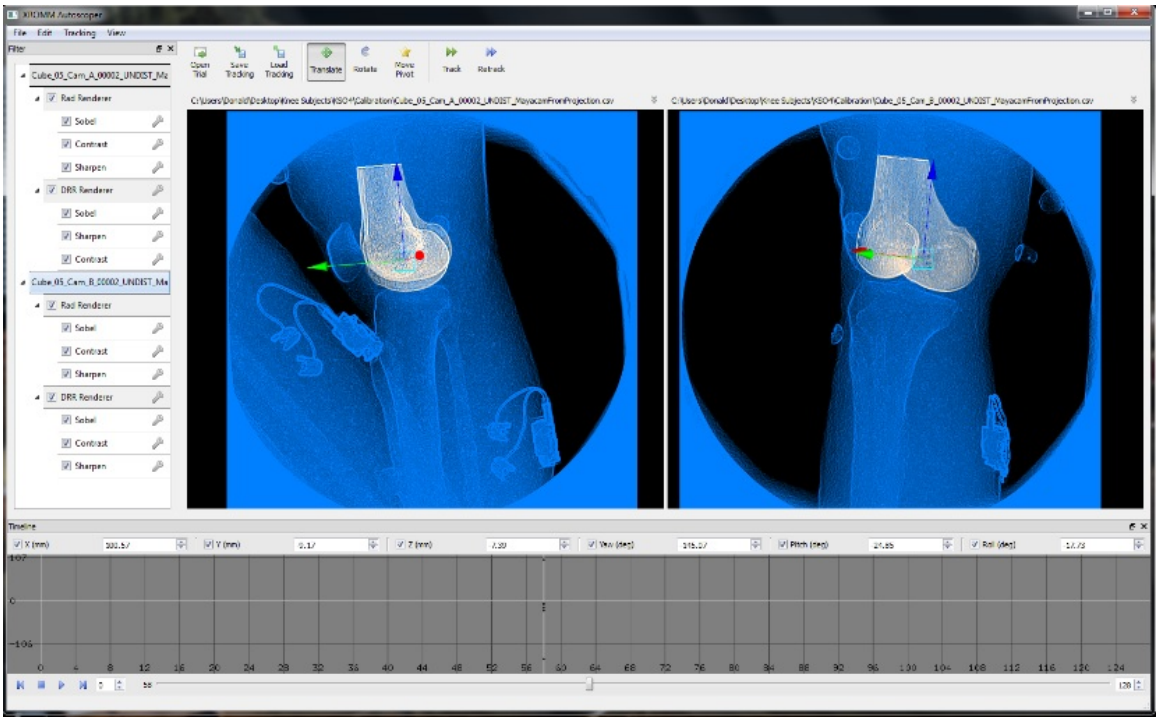

Figure B.9: 2D-3D alignment of the femoral component as shown in Autoscoper

When you have finished with the manual alignment, you can perform a Track by clicking the 'Track' button and this window will appear as illustrated in Figure B.10. Tracking performs a downhill Simplex optimization to try to best fit the location of the registered model over the 2D image.

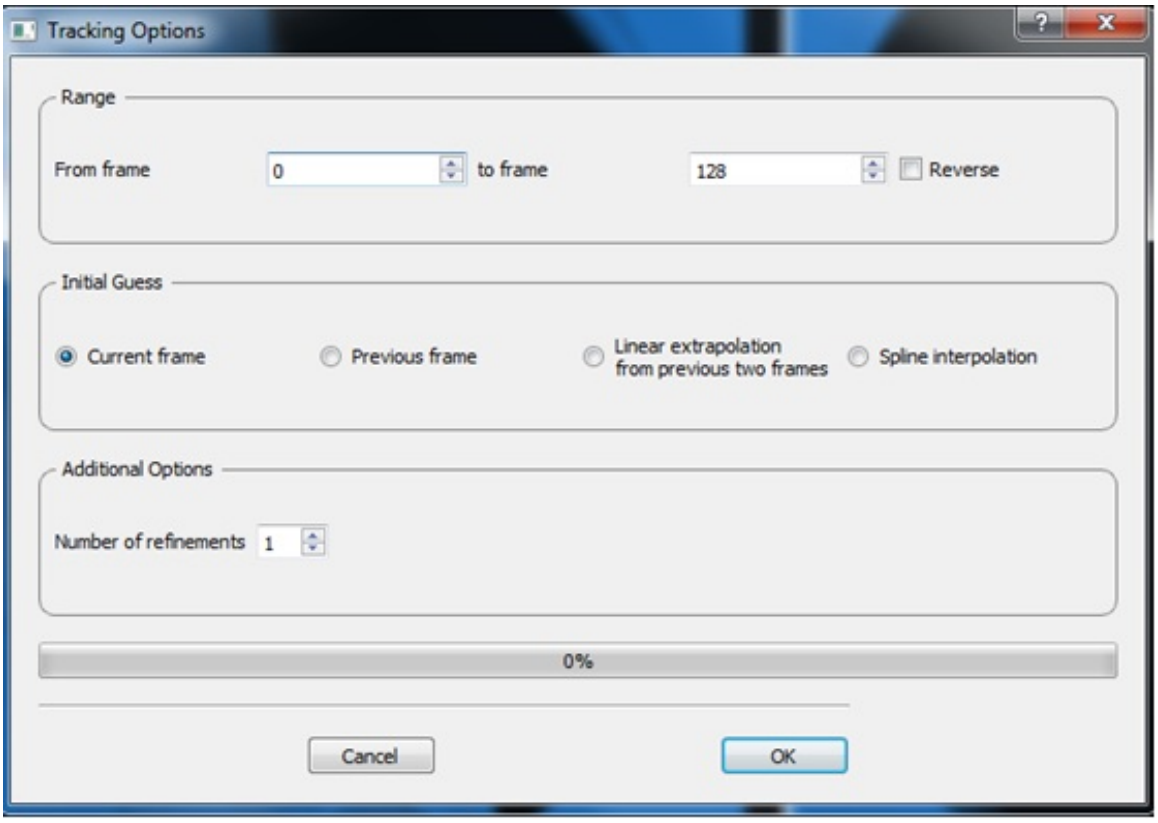

Figure B.10: Tracking options in Autoscoper

In both the From Frame and To Frame Prompt, enter the current frame that you are tracking and keep the Number of Refinements to be 1. For Initial guess select Current Frame and then press OK. Check the DOS window which will show progress messages (e.g. Frame 0 done in x iterations) (Figure B.11). Then select ”Retrack” button and wait for progress messages to appear in DOS window. Keep pressing ’Retrack’ until the same numbers of iterations are consecutively reached 3 times.

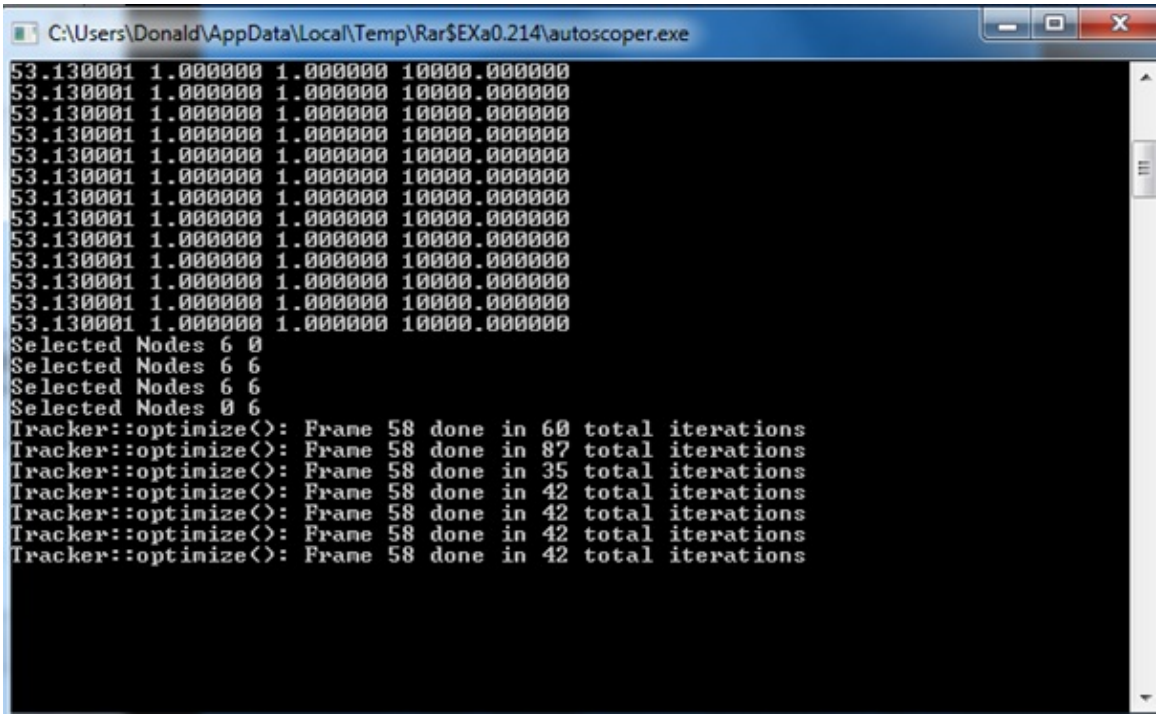

Figure B.11: DOS window showing when the optimization is completed

Highlight (click and drag box) black points for your current frame in timeline pane (below model panes) if the result is satisfactory click on 'Tracking' in utility menu and select 'Lock' (you can select the points by highlighting them with your mouse and then points in time line pane will be colored instead of black (see Figure B.12). If you lock them it means that the alignment of the 3D model with the 2D images will be locked for that current frame and even if you perform 'Tracking Options' that position will not be affected.

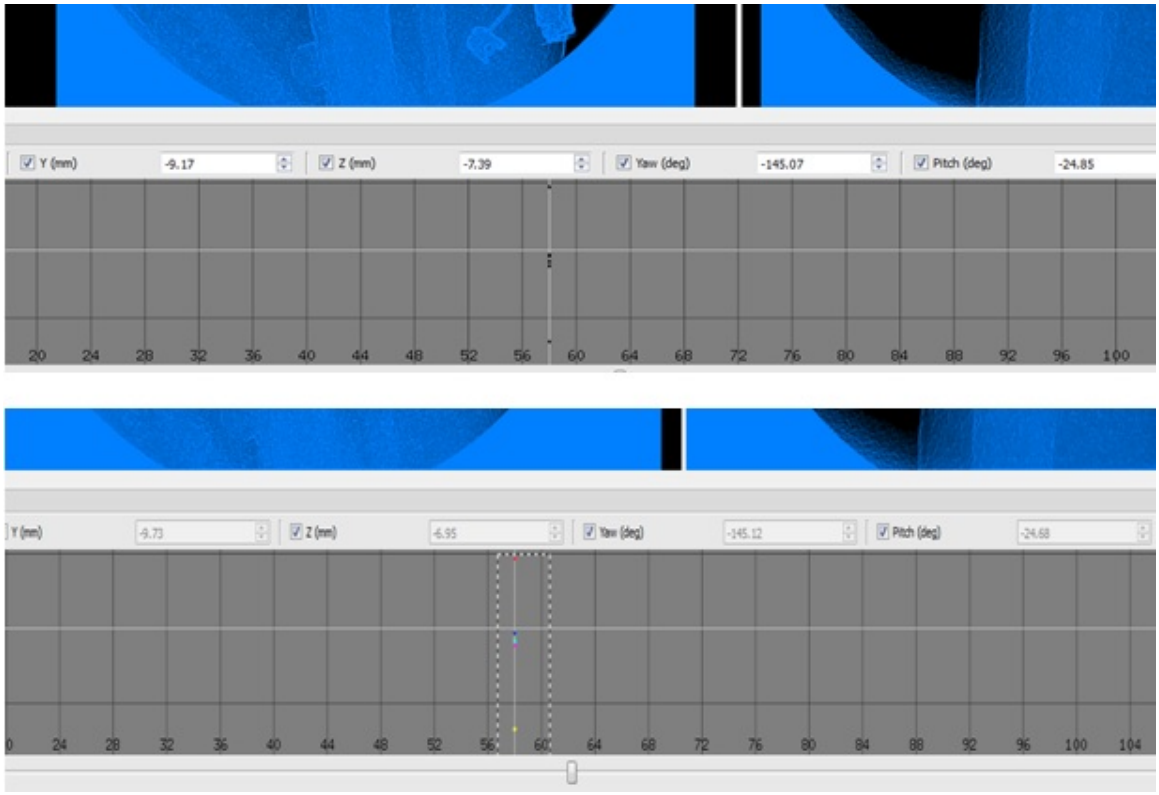

Figure B.12: How to lock a frame when the 2D-3D alignment for that current frame is satisfactory

Then you move on to another frame (according to the task, the number of frames skipped is going to be different, a good place to start is every 4 frames to do the alignment). If the result is not good enough then again you try to set the alignment manually and then you perform the 'Tracking Options' track command. After you finish your alignment for all of your trial and for example every 4 frames (and you have locked the alignment for each of the frames) then you save Tracking by selecting 'Save Tracking' button in order to write a file consisting of the 4x4 transformations for each model in each frame. After you give the name to your file that you want to save, the window as shown below will show up. Make sure that for the Format and Units Options you select the settings as illustrated in the Figure B.13 below.

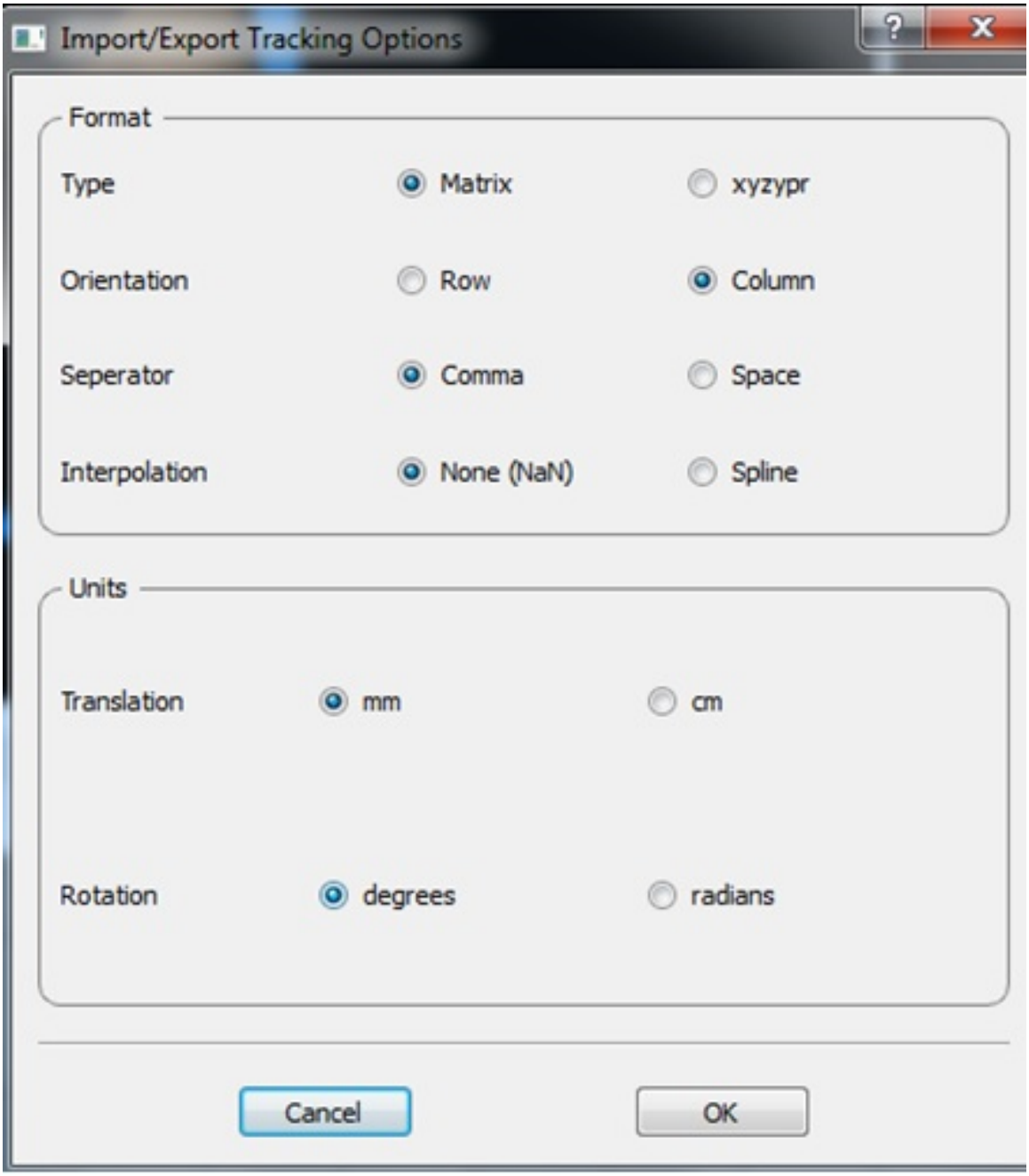

Figure B.13: Saving options in Autoscoper

You have two available options for the next step. Your choice of these two options is dependent on what your post processing pipeline looks like. a. The first option is to select the 'Track' button and now in the 'Tracking Options' for Initial Guess to select 'Spline Interpolation' instead and the range will be from your first tracking frame (e.g Frame 0) to

your last locked frame. Press OK and DOS window will show progress messages.

e.g. Frame 0 done in X iterations Frame 1 done in X iterations Frame n done in X iterations

Select 'Retrack' (wait for progress messages for all frames to appear in DOS window). Repeat the 'Retrack' until same number of iterations are consecutively reached 3 times.

b. Another option is to not perform any optimization ('Track' and 'Retrack') and instead when you have finished your tracking every 4 frames to press 'Save Tracking' and in the Import/Export Tracking options (see again Figure B.13) use Interpolation Spline (instead of none) and save your file. When you load your tracking file again all the missing frames that were not purposely tracked now they will be filled with tracking data.

Tracking method followed for the Healthy knees

1. First, do the alignment manually for your current frame until you are satisfied. 2. Apply optimization ('Track' and 'Retrack' option) for that frame. If you feel the alignment is correct then move on to step 3. Otherwise return to step 1 and reposition the model manually. There may be times when the tracking feature does not return good results (e.g. one view occluded, noisy radiographs). In this case it might be better to skip from step 1 to 3 directly. 3. Move on to the next frame you plan to track and repeat steps 1 and 2. As previously mentioned the amount of frames you skip in this step will be dependent on the task and your confidence in the spline or spline optimization features performed at the end. 4. Once you have tracked every n frames throughout your trial, you will want to take time to inspect several different display features Autoscoper offers. Below is a suggested workflow, but you may find some to be more helpful than others. a. Open the 3D world view and play through thetracking. Be sure to inspect the bone from several different angles. Keep an eye out for large unrealistic translations and perturbations in the orientation of the model registration, which typically look like rotations of the coordinate system shown by the pivot. Consider what these small rotations at the proximal (or distal) end of the bone would result in translations at the opposing end. b. Given the frames that look problematic in the 3D view, expand the graph pane to see if you can spot any large instantaneous rotations or translations. By expanding the graph view, and showing one DOF at a time, you can readily see these small perturbations. If you notice a large bump corresponding to an incorrectly tracked frame, you can try to lasso the point on the graph and, by holding shift, drag the design point into a more reasonable position. Be aware that the pivot position represents a coupled kinematic rotation to the actual model registration

and does not correspond directly to the graphed data (e.g. a 1o change of a frame on the roll/pitch/yaw graph may result in both a rotation and a translation of the model). You will often have to fix several DOFs at a single frame, realign manually, and return to the graphs until you are satisfied. 5. Once the kinematics in the 3D view look realistic for the entire trial, you can either save with spline or perform the optimization spline as discussed earlier in the document. If you perform the optimization spline, be sure to lock all of your tracked data points before running this command.